

Dissertation

**STUDY ON HOW TO REDUCE THERMAL AND MECHANICAL
STRESSES FOR CYLINDRICAL LARGE CERAMICS STRUCTURES**

H e n d r a / 07584104

Kyushu Institute of Technology

2010

Dissertation

STUDY ON HOW TO REDUCE THERMAL AND MECHANICAL STRESSES FOR CYLINDRICAL LARGE CERAMICS STRUCTURES

By

H e n d r a

(Student Number: 07584104)

Supervisor: Prof. Nao-Aki Noda

**Kyushu Institute of Technology
Graduate School of Engineering
Department of Mechanical Engineering
2010**

Contents

List of Figures

List of Tables

Abstract

1. Introduction

1.1 General of Ceramics	2
1.1.1 Traditional and Advanced of Ceramics	3
1.1.2 Classification and Properties of Advanced Ceramics	4
1.1.3 Application of Advanced Ceramics	8
1.1.4 Project Market of Advanced Ceramics	8
1.2 Thermal Stresses in Ceramics Structures	9
1.3 Static Fatigue and Cyclic Fatigue of Ceramics	12
1.4 Wear Surface Damage on the Ceramics Structure	21
1.5 Motivation and Objectives	23
1.6 Main Contributions	24
1.7 Outline of the Dissertation	24
References	25

2. Effect of Heat Transfer Coefficient on the Thermal Stress and Thermal Stress Analysis for Simple Ceramics Tube in the Low Pressure Die Casting Machine

2.1 Introduction	31
2.2 Effect of Heat Transfer Coefficient on the Thermal Stress when Ceramics Tube Dipping into Molten Metal	33
2.3 Analysis Method and Modeling	37
2.3.1 Analysis Model and Material Properties	37
2.3.2 Evaluation for Surface Heat Transfer	40
2.4 Thermal Stress for Vertical Tube	43

2.4.1	Results for Dipping Slowly	43
2.4.2	Results for Dipping Fast	46
2.4.3	Comparison between Dipping Slowly and Fast	47
2.5	Thermal Stress for Horizontal Tube	48
2.5.1	Results for Dipping Slowly	49
2.5.2	Results for Dipping Fast	49
2.5.3	Comparison between Dipping Slowly and Fast	51
2.6	Comparison between the Results of Vertical and Horizontal Tubes	53
2.7	Conclusions	54
	References	55

3. Thermal Stress and Heat Transfer Coefficient for Simple Ceramics Tube and Tube with Protuberance Dipping into Molten Aluminum

3.1	Introduction	57
3.2	Analysis Method	59
3.2.1	Analysis Model and Material Properties	59
3.2.2	Surface Heat Transfer Coefficient for Ceramics Tube	60
3.3	Thermal Stress for Simple Tube and Tube with Protuberance	60
3.3.1	Results for Dipping Slowly	61
3.3.2	Results for Dipping Fast	64
3.3.3	Comparison between Dipping Slowly and Fast	66
3.4	Conclusions	70
	References	71

4. Maximum Stress for Shrink Fitting System used for Ceramics Conveying Rollers

4.1	Introduction	73
4.2	Analytical Conditions	75
4.3	Results and Discussion	75
4.3.1	Maximum Tensile Stress	75

4.3.2 Effect of Shrink Fitting Ratio δ/d and Bending Moment upon the Maximum Tensile Stress $\sigma_{\theta_{max}}$	77
4.3.3 The Effect of Fitted Length L on σ_{θ_s} , $\sigma_{\theta_{max}}$ and σ_{θ_b}	80
4.3.4 The Effect of Materials Difference on σ_{θ_s} , $\sigma_{\theta_{max}}$ and σ_{θ_b}	80
4.3.5 The Effect of Radius Curvature ρ on σ_{θ_s} , $\sigma_{\theta_{max}}$ and σ_{θ_b}	82
4.3.6 The Effect of Diameter D on σ_{θ_s} , $\sigma_{\theta_{max}}$ and σ_{θ_b}	85
4.4 Conclusions	87
References	88

5. Strength Analysis for Shrink Fitting System Used for Ceramics Rolls in Continuous Pickling Line

5.1 Introduction	89
5.2 Analytical Conditions	91
5.3 Maximum Tensile Stress Analysis	92
5.3.1 Maximum Tensile Stress	92
5.3.2 Effect of Shrink Fitting Ratio and Bending Moment upon the Maximum Tensile Stress	93
5.3.3 The Effect of Thickness h on σ_{θ_s} and σ_{θ_b}	93
5.4 Fatigue Strengths Analysis of Ceramics Rolls	94
5.5 Conclusions	95
References	96

6. Summary

6.1 Conclusion of this Study	98
6.2 Future Issue	104

Acknowledgment

Appendix A

Appendix B

List of Figures

Figure 1.1	US view of national efforts and projected world markets for advanced ceramics	9
Figure 1.2	Comparison of stress-lifetime curves obtained in the static and cyclic fatigue test	13
Figure 1.3	Static and cyclic fatigue of alumina at room temperature	14
Figure 1.4	Static and cyclic fatigue strength sintered silicon nitride at room temperature	14
Figure 1.5	Static and cyclic fatigue strength sintered silicon carbide at room temperature	14
Figure 1.6	Cyclic fatigue life of hot-pressed AlN at room temperature	15
Figure 1.7	Static and cyclic fatigue of zirconia at room temperature Stress amplitude vs. time	15
Figure 1.8	Cyclic fatigue degradation of ceramics at room temperature Stress amplitude vs. time	15
Figure 1.9	Stress amplitude vs. time	17
Figure 2.1	Schema of the low pressure die casting (LPDC) machine	31
Figure 2.2	Zinc bath in the galvanizing line	32
Figure 2.3	Two-dimensional (2D) circle model	33
Figure 2.4 (a)	Maximum temperature vs. time relation of 2D model ($u = 25\text{mm/s}$)	34
Figure 2.4 (b)	Maximum stress vs. time relation of 2D model ($u = 25\text{mm/s}$)	34
Figure 2.5 (a)	Temperature and stress distribution for 2D model by Zukauskas formula ($u = 25\text{mm/s}$, $t = 75\text{s}$)	35

Figure 2.5 (b)	Temperature and stress distribution for 2D model by infinite value of α ($u = 25\text{mm/s}$, $t = 0.01\text{s}$)	36
Figure 2.5(c)	Temperature and stress distribution for 2D model using α analyzed by finite volume method ($u = 25\text{mm/s}$, $t = 0.98\text{s}$)	36
Figure 2.6(a)	Finite element mesh of vertical tube (No. of element=19500, No. of nodes=20816)	38
Figure 2.6(b)	Finite element mesh of horizontal tube (No. of element=45000, No. of nodes=55986)	38
Figure 2.7(a)	Surface heat transfer coefficient α for 2D and axi-symmetry model as a function of z in the molten metal with the velocity $u = 25\text{mm/s}$	40
Figure 2.7(b)	Surface heat transfer α as a function of x for two-dimensional cylinder in the molten metal with the velocity $u = 25\text{mm/s}$	41
Figure 2.8	Maximum stresses vs. time relation of vertical tube ($u = 2\text{mm/s}$)	44
Figure 2.9	Maximum stresses vs. time relation of vertical tube ($u = 25\text{mm/s}$)	45
Figure 2.10	Temperature and stress σ_z distributions of vertical tube ($u = 2\text{mm/s}$ at time $t = 20.5\text{s}$), displacement $\times 50$	47
Figure 2.11	Temperature and stress σ_θ distributions of vertical tube ($u = 25\text{mm/s}$ at time $t = 1.1\text{s}$), displacement $\times 50$	48
Figure 2.12	Maximum stresses vs. time relationship of horizontal tube ($u = 2\text{mm/s}$)	49
Figure 2.13	Maximum stresses vs. time relationship of horizontal tube ($u = 25\text{mm/s}$)	50
Figure 2.14 (a)	Temperature and stress σ_θ distributions of horizontal tube at	

	both ends $z = \pm 650\text{mm}$ ($u = 2\text{mm/s}$ at time $t = 75\text{s}$)	51
Figure 2.14 (b)	Temperature and stress σ_θ distributions of horizontal tube near the both ends at $z = 615\text{mm}$ ($u = 25\text{mm/s}$ at time $t = 1.73\text{s}$)	51
Figure 2.15(a)	Temperature and stress σ_θ distributions of horizontal tube ($u = 2\text{mm/s}$ at time $t = 75\text{s}$), displacement $\times 30$	52
Figure 2.15(b)	Temperature and stress σ_θ distributions of horizontal tube ($u = 25\text{mm/s}$ at time $t = 1.73\text{s}$), displacement $\times 30$	52
Figure 3.1	Schema of the low pressure die casting (LPDC) machine	57
Figure 3.2	Finite element mesh of ceramics stalk	58
Figure 3.3	Surface heat transfer coefficient α for simple tube and stalk with protuberance models as a function of x in the molten metal with the velocity $u = 25\text{mm/s}$	59
Figure 3.4	Maximum stresses vs. time relation for stalk with protuberance ($u = 2\text{mm/s}$)	62
Figure 3.5	Maximum stresses vs. time relation for simple tube and tube having protuberance ($u = 2\text{mm/s}$): similar to Fig. 2.8 (a)	63
Figure 3.6	Maximum stresses vs. time relation for stalk with protuberance ($u = 25\text{mm/s}$)	64
Figure 3.7	Maximum stresses vs. time relation for simple tube and tube with protuberance ($u = 25\text{mm/s}$)	65
Figure 3.8	Temperature and stress distribution for simple tube at the time of $\sigma_{\theta\text{max}}$ ($u = 2\text{mm/s}$, $t = 20.5\text{s}$)	66
Figure 3.9	Temperature and stress distribution for stalk with protuberance at	

	the time of $\sigma_{\theta_{\max}}$ ($u = 2\text{mm/s}$, $t = 41\text{s}$)	67
Figure 3.10	Temperature and stress σ_{θ} distributions of vertical tube at the time of $\sigma_{\theta_{\max}}$ ($u = 25\text{mm/s}$ at time $t = 1.1\text{s}$), displacement $\times 50$: similar to Fig. 2.11	68
Figure 3.11	Temperature and stress σ_{θ} distributions of vertical tube at the time of $\sigma_{\theta_{\max}}$ ($u = 25\text{mm/s}$ at time $t = 8.8\text{s}$), displacement $\times 50$	69
Figure 4.1	Layout of Conveying Rollers	73
Figure 4.2	Roller Structure	73
Figure 4.3	Models considered	74
Figure 4.4	FEM mesh	76
Figure 4.5	Stress distribution σ_{θ} when the sleeve and shaft are perfectly bonded as unit body	77
Figure 4.6	Stress distribution σ_{θ} when $\delta/d = 3.0 \times 10^{-4}$	77
Figure 4.7	Stress distribution σ_z when $\delta/d = 3.0 \times 10^{-4}$	77
Figure 4.8	σ_{θ} vs. δ/d when $L = 210\text{mm}$	78
Figure 4.9	σ_{θ} vs. δ/d when $L = 100\text{mm}, 150\text{mm}, 210\text{mm}$	79
Figure 4.10	σ_{θ} vs. δ/d when Steel, Ceramics, Cemented Carbide are used as the sleeve	81
Figure 4.11	Curvature radius on sleeve end corner of inner side	82
Figure 4.12	σ_{θ} vs. δ/d when $\rho = 5, 10, 20, 30\text{mm}$	83
Figure 4.13	σ_{θ} vs. δ/d when $D = 270, 405, 540\text{mm}$	84
Figure 4.14	σ_{θ} due to shrink fitting and load distribution when $\delta/d = 3.0 \times 10^{-4}$	86
Figure 5.1	Schematic diagram of new pickling line	90
Figure 5.2	New ceramics roll system (mm)	90

Figure 5.3	FEM mesh	91
Figure 5.4	Stress distribution σ_o when $\delta/d = 1.5 \times 10^{-4}$	92
Figure 5.5	σ_o vs. δ/d when $h=20\text{mm}$	93
Figure 5.6	σ_o vs. δ/d when $h=10, 20, \text{ and } 30\text{mm}$	94
Figure 5.7	Mean stress and stress amplitude for ceramics rolls $h=30\text{mm}$	95

List of Table

Table 1.1 Mechanical and physical properties of advanced structural ceramics	6
Table 2.1 The Physical properties of molten aluminum at 750°C (1023K)	39
Table 2.2 Mechanical properties of Sialon ceramics	39
Table 2.3 Assumption of surface heat transfer coefficient α W/m ² .K	42
Table 2.4 The maximum values of tensile stresses for simple tube	54
Table 3.1 Surface heat transfer coefficient α , W/m ² .K	61
Table 3.2 Maximum stresses for stalk with protuberance compared with the results of simple tube at the same time	70
Table 4.1 Material Properties	76
Table 5.1 Material Properties	91

Abstract

Structural engineering ceramics are widely used in all kinds of engineering fields for their advantages of wear resistance, corrosion resistance, abrasion resistance and high temperature resistance. The ceramics have been used for turbo-chargers, gas turbines, auto heat engines, rolls, stalks and conveying rollers. However, it is not easy to utilize large ceramics material in many kinds of engineering fields more efficiently because of their high cost of machining and low fracture toughness compared with metallic material. In this study, the maximum stresses of ceramics structure will be mainly considered by the application of the finite element method. Then, how to reduce the maximum stress will be investigated with varying dipping speeds for ceramics tube, and with varying the dimensions of the structure for conveying rollers.

Chapter 1

Introduction

Metal, polymers, and ceramics are classified as one of materials for structure. In metals⁽¹⁾, the bonding process is predominantly metallic, where delocalized electrons provide glue that kept cores of positive ion each other⁽²⁾. Metals consist of high density, medium to high melting point and elastic modulus, reactive and ductile. Polymers⁽³⁾ consist of very long, for the most part, C-based chains to which other organic atoms and molecules are attached. Polymers⁽³⁾ consist of very low density lower melting points and elastic modulus, higher thermal expansion of coefficients, lower stiffness than most metals or ceramics, ductile and brittle. Ceramics are compound between metallic element and nonmetallic element⁽³⁾. They are non-magnetic, chemically stable, good thermal and electric isolative, and hard but very brittle. The earliest ceramics were pottery objects made from clay and either by itself or mixed with other materials. Ceramics are now includes industrial products, building products and art objects. In the 20th century, new ceramics materials were developed for use in advanced ceramics engineering; for example, in semiconductors and parts of automotive engines.

Large ceramics structure has been recently used for tube (stalk) in the low pressure die casting machine⁽⁴⁾⁻⁽⁶⁾, conveying rollers in the hot rolling mills⁽⁷⁾, rolls in the galvanizing line⁽⁸⁾, rolling, rolls, and die cast sleeve⁽⁹⁾⁽¹⁰⁾. Previously, cast iron, steel and those coated of hard layer is used for stalk, conveying rollers and rolls. However, in case of conveying rollers, cast iron, steel and those coated conveying rollers must be changed frequently because hot conveyed strips induce wear on the roller surface in short period. Similarity with the galvanizing process, since the molten metal has high temperature, corrosion and abrasion arise on the roll surface only in a week, causing the

deterioration of quality of plating. Therefore, the production lines must be stopped to change the rolls, tube and roller. Then, the wear damage portions are usually repaired by using the flame spray or plasma jet coating. To prevent the surface damage, rollers are coated by alloyed steel, and rolls for the galvanizing line are coated by cemented carbide⁽¹¹⁾ and those coated rolls and roller are inadequate for needs. Recently, use of ceramics has been also started and promoted⁽¹²⁾.

In this study, ceramics are considered for material tube and rollers because they have high temperature resistance, high corrosion resistance and high abrasion resistance. However, the attention should be paid to the thermal stress when the ceramics tube is dipped into the molten metal. It is important to reduce the risk of fracture that may happen due to the thermal stresses. For conveying rollers, attention should be paid to the maximum tensile stresses (appearing at the edge of the sleeve) for brittle fracture and maximum repeated stress amplitude for fatigue fracture. In particular, as the fracture toughness of ceramics is extremely smaller compared with the values of steel, furthermore, exact stress analysis for the roller becomes more and more important.

Therefore, in this study the finite element method is applied to structure of conveying rollers, rolls in pickling continuous line and ceramics tube to calculate the thermal stress, maximum tensile stress and maximum repeated stress amplitude for ceramics that being strong in compression and weak in tension.

1.1 General of Ceramics

Ceramics are defined as solid materials that have as their essential component, and are composed by large part of inorganic non metallic materials⁽¹³⁾. Ceramics are inorganic, nonmetallic materials that have been subjected to high temperatures during

manufacturing⁽¹⁴⁾. Ceramics are solid compound with combinations of at least of two non metallic elemental solids and/or a combination of metal and non metallic element⁽²⁾. For example, magnesia, MgO, is ceramics when a solid compound composed of metal Mg, bonded to the non metal, O₂. Silica is ceramics when it combines with non metallic elemental solid Si and non metal O₂. Oxides, nitrides, borides, carbides and silica at all metals and non metallic elemental solids are ceramics. The characteristics of ceramics are high stiffness, high wear and temperature resistances, good thermal and electric isolative characteristic, non-magnetic and chemically stable, refractory and brittle.

1.1.1 Traditional and Advanced of Ceramics

Ceramics have been used in the world for thousand years in types of earthenware, pottery, porcelain, tiles etc. In old days, the process was considered only to the traditional or silicate-based. Nowadays, ceramics science or engineering encompasses much more than silicates and divided into traditional and advanced ceramics. Traditional ceramics are only used for sanitary ware, porcelains, Chinese fines and glass products. Strength of traditional ceramics is quite satisfactory for such structural products such as drain tile, bricks, and sewer pipe.

However, in more recent years, much money and time has been expended on developing stronger ceramics materials and improves the properties of ceramics material to compete with metal alloys for demanding structural applications. These materials are commonly termed “advanced ceramics” or, usually in Japan “fine ceramics”⁽¹⁴⁾. Dissimilarity to the traditional ceramics and advanced ceramics mainly occurs on raw materials and manufacturing process. Traditional ceramics are manufactured by mixing, shaping and firing natural minerals, and meanwhile, advanced

ceramics are manufactured by using highly purified natural raw materials, artificial raw materials synthesized through chemical processes and other non-naturally compounds. Through a series of precisely controlled, complex processes such as grinding, forming, sintering and machining, these compounded raw materials turn out to be advantage value-added products with excellent dimensional accuracy and characteristics functional. Advanced ceramics are used to make components that require high levels of performance and reliability.

1.1.2 Classification and Properties of Advanced Ceramics

Five important classes of advanced ceramics for structure are:

1. Alumina ceramics (Al_2O_3)

Alumina ceramics have been used in commercial application because of their availability and low cost. Alumina ceramics are often classified into high alumina (80% alumina oxide) and porcelains (having less than 80% aluminum oxide). High aluminas are used in many mechanical devices and electronics. Strength and other properties generally improve as the percentage of alumina is increased. However, cost increases because of the difficulty in processing.

2. Zirconia ceramics (ZrO_2)

Zirconia ceramics are an important class of ceramic materials that are characterized by high strength and toughness at room temperature. Zirconia exist in three different crystal structures such as monolithic (stable at room temperature and become up to about 1170°C), tetragonal (stable up to 2370°C) and cubic. Three types of zirconia ceramics used in the technical applications are cubic, partially stabilized and tetragonal zirconia. Cubic zirconia has low fracture toughness and strength. Partially

stabilized zirconia (PSZ) has larger fracture toughness. Tetragonal zirconia has highest toughness and strength compared to cubic and partially stabilized zirconias.

3. Silicon nitride ceramics (Si_3N_4)

Silicon nitride is one of the strongest and most toughness structural ceramics. They have an excellent oxidation resistance, very good thermal shock resistance since of its low thermal expansion coefficient and high strength. Silicon nitride classified by processing method, which is sintered, hot pressed, reaction bonded and hot iso-statically pressed. Silicon nitride is used for anti wear element for pump and water whale, conveying rollers in the hot rolling mills and for sink rolls in the galvanizing line. Silicon nitride is used in this study.

4. Sialon ceramics (SiAlON)

Sialon is usually made by addition of AlN , MgO , BeO , Y_2O_3 or other metal oxides to silicon nitride. Advantages of Sialon, its lower cost compared than silicon nitride and meanwhile mechanical properties are better than those of alumina. Sialon is used for heat protective tube, rolls for thin strip rolling, ceramics tube in the low pressure die casting machine and etc. Sialon is used in this study.

5. Silicon carbide ceramics (SiC)

Silicon carbide is widely used in applications requiring wear resistance, high hardness, high corrosion resistance and high oxidation resistance but low toughness. Silicon carbide classified by processing method is reactions bonded or reaction sintered, hot pressed, sintered and chemical vapor deposition (CVD). The advantage of silicon carbide for reaction bonded is low cost, and the other side, silicon carbide for hot pressed is high strength but high cost for finished components, which is due to the difficulty in machining process. Advantage of sintered type is that most of the

Table 1.1 Mechanical and physical properties of advanced structural ceramics⁽¹⁵⁾

Material	Density (g/cm ³)	Flexural strength (MPa)	Fracture Toughness (MPa.m ^{1/2})	Elastic Modulus (GPa)	Poisson's ratio	Hardness (GPa)	Thermal expansion coefficient (1/K)	Thermal conductivity (W/mK)
Silicon nitride								
sintered	3.2	600	4.5	276	0.24	14	3.4	28
hot pressed	3.2	800	5.0	317	0.28	20	3.2	30
reaction bonded	2.5	210	3.6	165	0.22	10	2.8	6
sintered reaction bonded	3.3	825	-	297	0.28	19	3.5	30
HIPed	3.2	1000	6.0	310	0.28	20	3.5	32
Sialon	3.2	650	5.0	297	0.28	18	3.2	22
Silicon carbide								
Hot pressed	3.2	550	3.9	449	0.19	25	4.5	70
Sintered	3.1	400	3.0	427	0.19	27	4.8	80
Reaction-bonded	3.0	350	3.5	385	0.19	17	4.4	90
CVD	3.2	500	2.6	450	-	30	5.5	150
Alumina (%)								
85	3.4	296	3.5	221	0.22	10	5.3	15
90	3.6	338	3.5	276	0.22	11	6.1	17
96	3.7	352	4.5	303	0.21	12	6.3	23
99.8	3.9	552	4.5	386	0.22	15	7.1	30
Zirconia								
Cubic	5.9	245	2.4	150	0.25	11	8.0	1.7
TZP	6.1	1020	11.0	210	0.24	13	10.6	0.4
PSZ	6.0	750	8.1	205	0.23	12	8.3	2.1

machining can be used easily.

Table 1.1 shows the mechanical and physical properties of advanced structural ceramics⁽¹⁵⁾. Five categories of properties of advanced ceramics for engineering application are shown as follows:

1. Abrasion and erosion resistances

The abrasion resistance is related to the hardness of the material. Ceramics are suitable for this requiring for abrasion and erosion resistance because of their high hardness. For example PSZ is used for knives in textile fiber processing, silicon carbide is used in rocket nozzles, spray drying nozzles and sandblasting nozzles. Silicon carbide and Sialon are used for bearings, seals, and bushing for slurry and

particulate handling equipment. In this study, Sialon is used for ceramics tube in the melting pot of the low pressure die casting machine. Si_3N_4 is used for conveying rollers in the hot rolling mills and rolls in the pickling continuous line.

2. Corrosive resistance

Ceramics are generally more resistant to chemical reactions and degradation than metals. Advanced ceramics such as silicon nitride and PSZ are used as pump sleeves, seals, and bushing and valve components in the chemical process industry to combat corrosive wear in harsh environments. In some applications the component must operate at temperatures as high as 850°C . Due to corrosive resistance, in this study, silicon nitride and Sialon are used for ceramics tube in the low pressure die casting machine and rolls in the continuous galvanizing line.

3. Wear resistance at elevated temperature

Advanced ceramics are used in metal forming and high speed metal cutting operations⁽¹⁶⁾. Sialon, silicon nitride and PSZ are used in metal forming process such as bending, extrusion, drawing and tube expanding. PSZ, TiB_2 , silicon nitride, $\text{Al}_2\text{O}_3/\text{B}_4\text{C}$ are used in the high cutting speed applications. Their processes require high hardness, fracture strength, and wear resistance at high temperature. In this study, silicon nitride used for conveying rollers in the hot rolling mills is analyzed.

4. Low density

Advanced ceramics are used in ceramic rolling element bearing because high abrasive and corrosive resistance, and high temperature environments⁽¹⁷⁾⁻⁽²⁰⁾.

An important advantage of ceramics, besides high strength and resistance to abrasion and corrosion, their lower density is another advantage. Ceramics bearing based on silicon nitride have high strength and low coefficient of thermal expansion,

which minimizes distortions and thermal stresses; allow a longer life than conventional bearing⁽²¹⁾.

5. Thermal properties.

Excellent thermal resistivity of ceramics is based on utilization of ceramics cylinder liners in low heat rejection engines⁽²²⁾ and tunnel furnace rolls operating in the range 1100~1200⁰C⁽²³⁾.

In this study, Sialon used to the structure for thermal stress and silicon nitride for shrink fitting stress and operating stress are analyzed.

1.1.3 Application of Advanced Ceramics

Advanced ceramics have been commonly used since the 1970s. Advanced ceramics have found in electrical insulator, automotive engines⁽²²⁾⁽²⁴⁾, tribological components⁽¹⁵⁾ and cylinder head plates, pistons and turbocharger rotors, machine tools, hot rolling mills and low pressure die casting machine. More than 60% of fine (advance) ceramics are used for electromagnetic parts; 25-26% are used for machine parts and 6-7% for biochemical purposes⁽²⁵⁾.

1.1.4 Project Market of Advanced Ceramics

Figure 1.1 shows the US view of national efforts and projected world market for advanced ceramics⁽²⁶⁾⁽²⁷⁾. As shown in Fig. 1 the lower area is prediction of the domination of markets in Japan and US. It also shows the position Americans have assigned to the rest of advanced ceramics. Upper area shows the national effort on funding over the last few decades and present situation is that there is a large American programme, a substantial German and Japanese. According to market studies, industrial

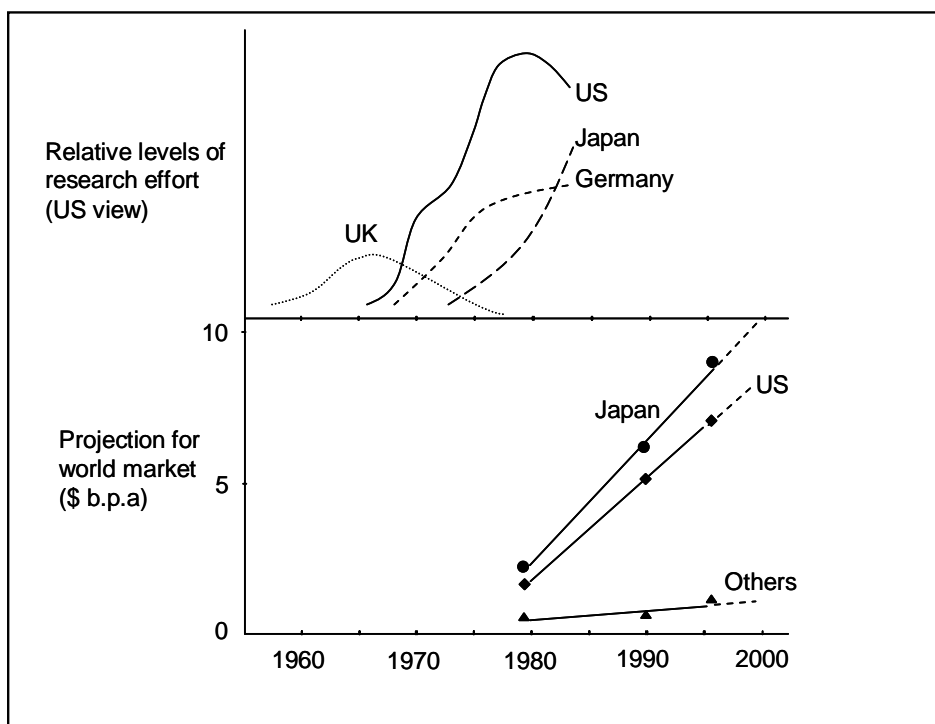


Fig. 1.1 US view of national efforts and projected world markets for advanced ceramics⁽²⁶⁾⁽²⁷⁾

ceramics had a 1986 world-market volume of roughly US\$5.4 billion (10^9) (Japan Fine Ceramics Association, 1988). Rapid growth is expected to expand this volume US\$24.5 billion within the next 10 years. The percentage of the share of structural ceramics (thermal or mechanical applications) is still small (13%) compared to that of the functional ceramics (electrical or magnetic applications)⁽²⁸⁾.

1.2 Thermal Stresses in Ceramics Structures

Thermal stresses are stresses induced in a body as results of distribution in temperature⁽³⁾. An understanding of the origins and nature of thermal stresses is important because these stresses can lead to fracture in brittle material such as ceramics. When a solid body is heated or cooled, the internal temperature distribution will depend on its size and shape, the thermal conductivity of the material, and the rate of

temperature change. Thermal stresses may be established as a result of temperature gradients across a body, which are frequently caused by rapid heating or cooling, in that the outside changes temperature more rapidly than the inside⁽³⁾. The two prime sources of thermal stresses are restrained thermal expansion (or contraction), and temperature gradients established during heating or cooling.

Thermal shock is resulting from thermal stresses induced by rapid temperature changes and caused by the fracture of a body. Because ceramic materials are brittle, they are especially susceptible to this type of failure. The thermal shock resistance of many materials is proportional to the fracture strength and thermal conductivity, and inversely proportional to both the modulus of elasticity and the coefficient of thermal expansion. As a consequence of their brittleness and their low thermal conductivities, ceramics are prone to the thermal shock; i.e., they will crack when subjected to large thermal gradients. The robustness of a material to thermal shock is characterized with the thermal shock parameter⁽²⁹⁾:

$$R_T = \frac{\lambda \cdot \sigma_T \cdot (1 - \nu)}{\alpha_{TE} \cdot E} \quad (1.1)$$

where

- λ is thermal conductivity
- σ_T is maximal tension the material can resist
- α_{TE} is the thermal expansion coefficient
- E is the Young's Modulus
- ν is the Poisson ratio

This is why it is usually not advisable to pour very hot liquid into a cold glass container, or cold water on a hot ceramic furnace tube. The rapidly cooled surface will want to contract, but will be restrained from contract by the bulk of the body, so tensile stresses will develop at the surface. If these stresses are large enough, the ceramic will crack⁽²⁾. The crack resistance is critical for structural components and ceramics products operating under extreme mechanical and thermal loads whose brittle fracture is intolerable even under arbitrary loads⁽³⁰⁾.

To calculate the thermal stress, it is necessary to know the surface heat transfer coefficient α when the tube dips into the molten metal⁽⁸⁾. Since three-dimensional thermo-fluid analysis to estimate α is very complicated, two-dimensional solutions will be considered. Zukauskas⁽³¹⁾ proposed the following equation to estimate Nusselt number for a two-dimensional cylinder in the fluid with the velocity u .

$$Nu_m \equiv \frac{\alpha_m \cdot D}{\lambda} = C_w \cdot Re^n \cdot Pr^{0.37} \cdot \left(\frac{Pr}{Pr_w} \right)^{0.25} \quad (1.2)$$

$$Re = \frac{u \cdot D}{\nu}, \quad Pr = \frac{C_p \cdot \eta}{\lambda} \quad (1.3)$$

Here, α_m is the average surface heat transfer coefficient, λ is thermal conductivity, D is the diameter of the cylinder, C_l and n are constants determined by Reynolds number Re ⁽³²⁾⁽³³⁾. Also, Pr is Prandtl number, and subscript w denotes the property for temperature of cylinder wall. The velocity u can be calculated by the diameter of the tube divided by the time when the tube dips into the molten aluminum. In this study, two-dimensional (2D) and axi-symmetric models are analyzed by using Zukauskas formula and the finite volume method to calculate α when the stalk dips into molten metal.

The finite volume method (FVM) based on the pressure corrections procedures

such as the SIMPLE (semi-implicit method for pressure linked equations) algorithm has been developed and employed widely in conventional computational fluid dynamics (CFD) applications⁽³⁴⁾. The FVM can more efficiently utilize both time and computer space and is also more computationally stable than the finite element method (FEM) when modeling polymer processing⁽³⁵⁾.

1.3 Static Fatigue and Cyclic Fatigue of Ceramics

Fatigue is a form of failure that occurs in structures subjected to dynamic and fluctuating stresses⁽³⁾. Fatigue is important in as much as it is the single largest cause of failure in metal, polymers and ceramics. Fatigue failure is brittle like in nature even in normally ductile metals, in that there is very little, if any, gross plastic deformation associated with failure. The process occurs by the initiation and propagation of crack, and ordinarily the fracture surface is perpendicular to the direction of an applied tensile stress.

In ceramics, static fatigue exists and the mechanism has been considered as main fatigue mechanism until about 20 years ago. Static fatigue proceeds by sub-critical crack growth under constant loads and has been recognized as an environmentally activated process. Gang JIN et al.⁽³⁶⁾ carried out the static and cyclic fatigue of alumina using smooth surface flexures specimen under several constant stress levels. The investigation showed that by comparing of the stress-lifetime curves for the static tests and modified cyclic curves, it is apparent that the difference between the static and cyclic curves in the Fig. 1.2 is relatively small at higher stress levels and more significant at lower stress levels. In one hand, this suggested that at higher stress levels cracks will propagate so quickly that the cyclic effects will not be sufficient to reduce

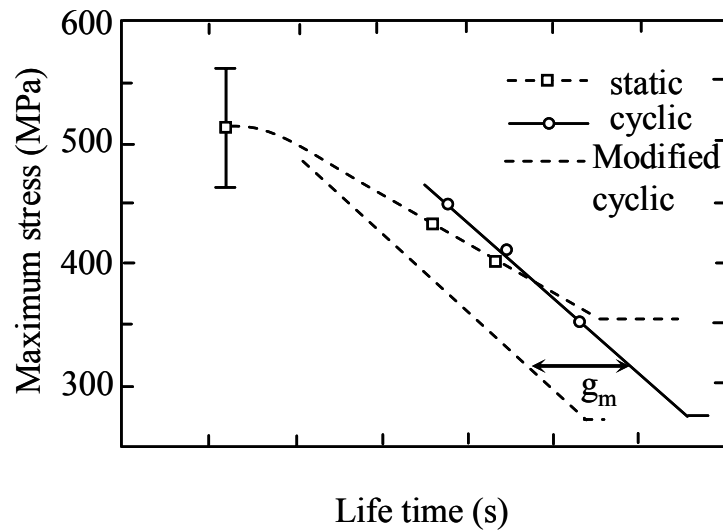


Fig. 1.2 Comparison of stress-lifetime curves obtained in the static and cyclic fatigue test of alumina⁽³⁶⁾

the stress shielding by bridging in the process zone wake⁽³⁶⁾. In addition, at higher stress levels, the time-dependent mechanism of cyclic fatigue is predominant due to an environmentally enhanced crack growth, meanwhile, the difference between the lifetimes in the static and cyclic fatigue tests becomes small. On the other hand, at lower stress level, the rate of the crack extension caused by cyclic fatigue loading is low and stress shielding at the process zone wake may be extensively weakened due to the cyclic stress, with accelerates the crack extension rate. Therefore, the difference between the lifetimes in the static and cyclic fatigue tests becomes larger.

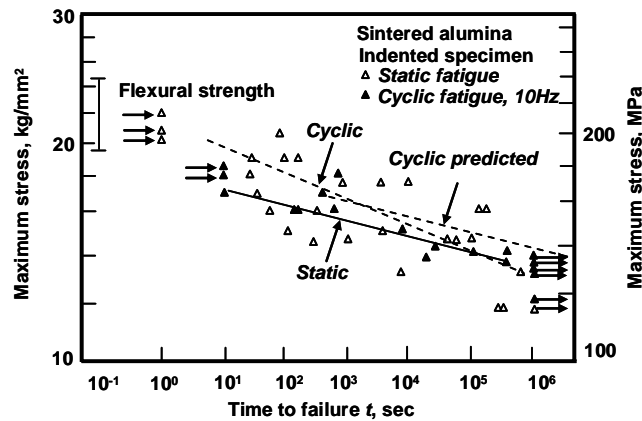


Fig. 1.3 Static and cyclic fatigue of alumina at room temperature⁽³⁷⁾.

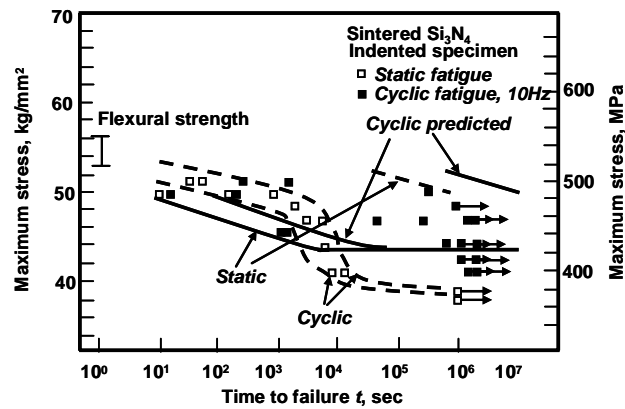


Fig. 1.4 Static and cyclic fatigue strength sintered silicon nitride at room temperature⁽³⁷⁾.

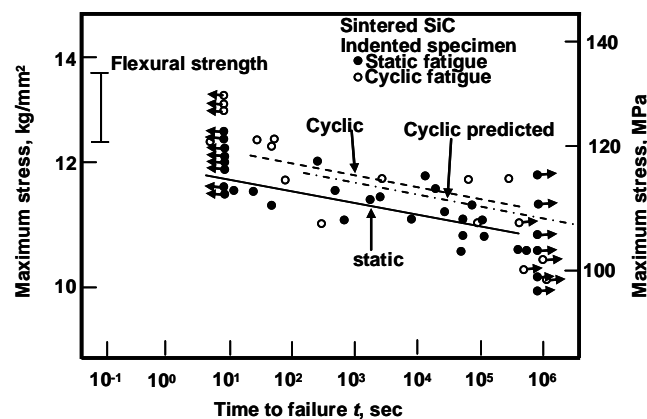


Fig. 1.5 Static and cyclic fatigue strength sintered silicon carbide at room temperature⁽³⁷⁾.

Kawakubo et al.⁽³⁷⁾ showed static and cyclic fatigue of alumina, silicon nitride,

silicon carbide, AlN and zirconia. Figure 1.3 shows static and cyclic fatigue exists in alumina at higher frequency and amplitudes. For the case of silicon nitride, effect of the cyclic fatigue is exist⁽³⁷⁾⁽³⁸⁾⁽³⁹⁾ in specimens. At the lowest limit of fatigue life markedly increased as the applied stress decreased and no specimen failed below 76% of the

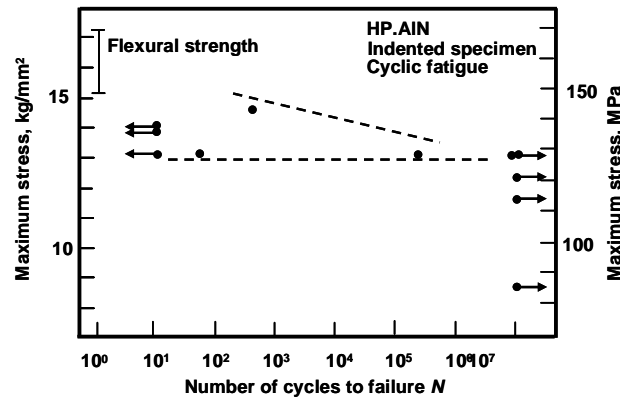


Fig. 1.6 Cyclic fatigue life of hot-pressed AlN at room temperature⁽³⁷⁾

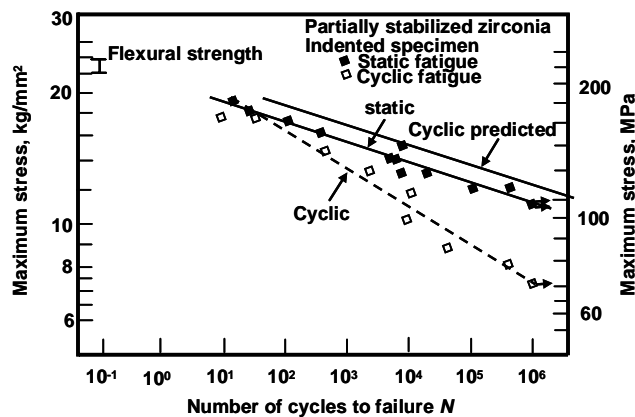


Fig. 1.7 Static and cyclic fatigue of zirconia at room temperature⁽³⁷⁾

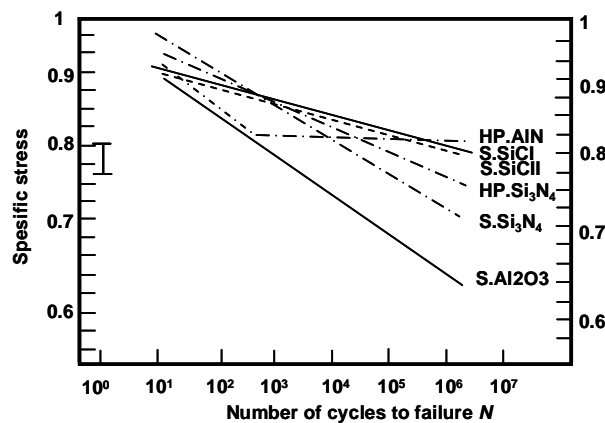


Fig. 1.8 Cyclic fatigue degradation of ceramics at room temperature⁽³⁷⁾

average flexural strength up to 10^6 s. Figure 1.4 shows the results of static and cyclic fatigue. The two specimens were tested at each stress level, and the difference in the fatigue life between two specimens was small as 10 times. The fatigue life increased as the applied peak stress was lowered but in a non-monotonic manner. At the peak stress of 372MPa, about 70% of the average flexural stress, no cyclic specimen failed. Comparing the static and cyclic fatigues, the minimum time to failure in both cases was similar, when the applied load was relatively high as shown in Fig. 1.4. Arbitrary fatigue limit in cyclic loading, however, was lower than that in static loading.

In the case of silicon carbide, Kawakubo et al.⁽³⁷⁾ showed static and cyclic fatigue of silicon carbide (see Fig. 1.5). The investigation showed that between the static and cyclic lifetimes, little difference was observed in silicon carbide. Figure 1.6 shows the cyclic fatigue of AlN. The apparent fatigue limit was about 80% of the average flexural strength for AlN. Hot-pressed AlN showed a mixed mode fracture of inter-granular and trans-granular cracking, and SiC exhibited trans-granular cracking only. For zirconia ceramics, Kawakubo et al.⁽³⁷⁾ showed static and cyclic fatigue of zirconia (see Fig.1.7). The cyclic fatigue strength of zirconia became as small as one-third of its flexural strength. Moreover, the fracture mode for static and cyclic fatigue in zirconia was the mixed type of trans-granular and inter-granular cracking, although the inter-granular cracking was dominant in the fast fractured portion. The fatigue degradation is increased compared to its flexural strength in this order: hot-pressed AlN, sintered SiC, hot-pressed Si₃N₄, sintered Si₃N₄ and sintered Al₂O₃ (see Fig. 1.8). The apparent fatigue limit was about 80% of the average flexural strength for AlN, and 60% for sintered Al₂O₃.

In general, three different fluctuating stress-time modes are possible in fatigue

such as reversed stress cycle, repeated stress cycle and random stress cycle. Figure 1.9 a

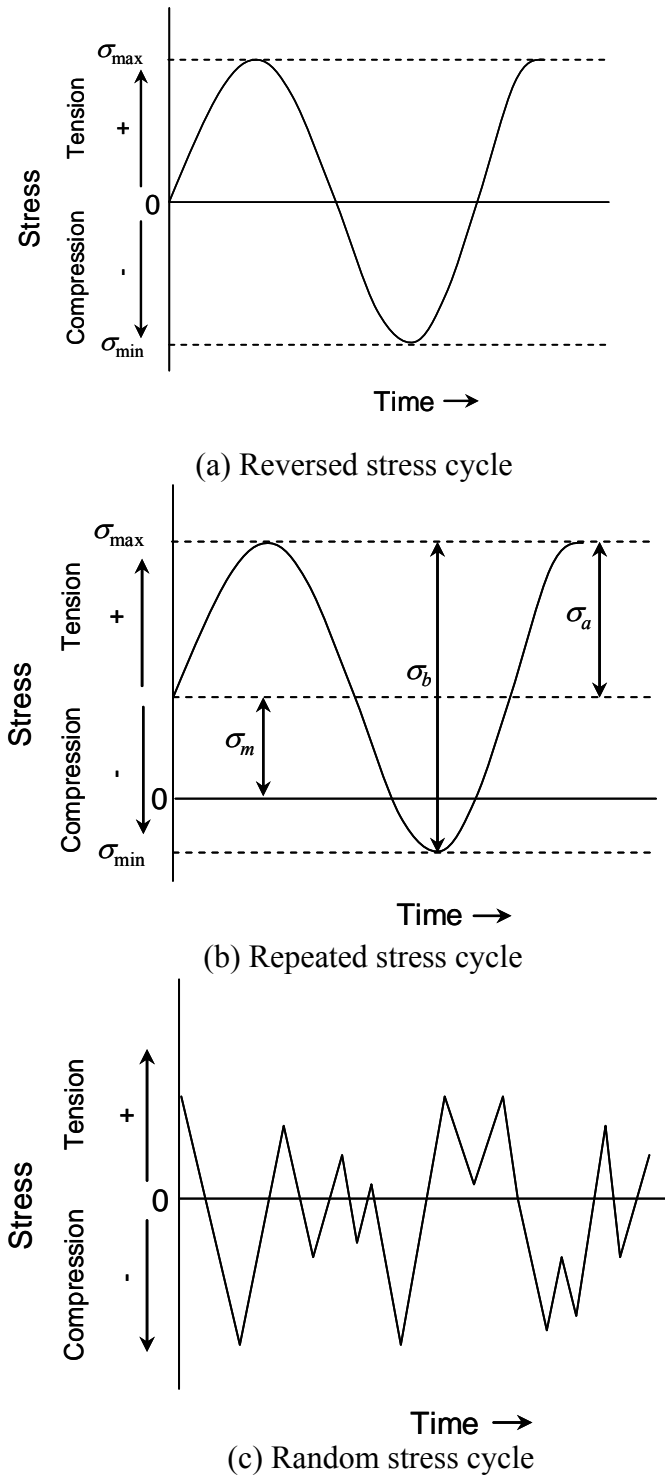


Fig. 1.9 Stress amplitude vs. time

shows reversed stress cycle, in which the stress alternates from a maximum tensile stress to a maximum compressive stress of equal magnitude. Repeated stress, in which maximum (σ_{max}) and minimum (σ_{min}) stresses are asymmetrical relative to the zero stress level as shown in Fig. 1.9 b. Random stress cycle, the stress level may vary randomly in amplitude and frequency as shown in Fig. 1.9 c.

The cyclic stress amplitude is defined as⁽²⁾⁽³⁾

$$\sigma_{amp} = \frac{(\sigma_{max} - \sigma_{min})}{2} \quad (1.4)$$

The mean stress σ_m is defined as the average of the maximum and minimum stresses in the cycle, namely,

$$\sigma_m = \frac{(\sigma_{max} + \sigma_{min})}{2} \quad (1.5)$$

The range of stress σ_b is defined as difference between σ_{max} and σ_{min} , namely,

$$\sigma_b = \sigma_{max} - \sigma_{min} \quad (1.6)$$

whereas the stress ratio R is defined as the ratio of maximum and minimum stress amplitudes.

$$R = \frac{\sigma_{min}}{\sigma_{max}} \quad (1.7)$$

Fatigue in ceramics materials is a very complicated phenomenon, which is involved in at least the following three factors:

1. Mechanical factor, refer to loading conditions (static and cyclic stress).
2. Microstructure factor, such as grain size, grain shape and toughening phase.
3. Environmental factor, especially for oxide ceramics with water and other corrosive medium.

Cyclic fatigue is mechanical phenomenon in which load oscillation leads to crack propagation. Meanwhile, ceramics are loaded cyclically, crack initiated from flaws in ceramics; the cracks then grow and final failure occurs at critical size. Different with metal fatigue, the crack initiation in ceramics fatigue under load is not known very well. For metal fatigue, the fatigue life is composed of crack initiation and crack propagation.

The characteristic of cyclic fatigue in ceramics appear to be quite different to metal fatigue:

1. Unlike in ductile materials fatigue crack in ceramics do not appear to initiate naturally; crack initiation is invariably with some pre-existing defect such as PSZ⁽⁴⁰⁾.
2. Unlike metal fatigue where there is a characteristic fracture mode for cyclic loading, i.e., striation growth, which is quite distinct from that for monotonic loading, the morphology of fatigue fracture surfaces in ceramics is almost identical to that under monotonic loads.
3. Effect a fatigue-crack growth rates becomes significant in microstructures of ceramics. The microstructure influences on fracture by fatigue.
4. The high sensitivity of growth rate for the stress intensity especially the exponent m in the simple Paris equation (see Eq.1.8) can take values as high as

15 to 50⁽⁴¹⁾.

$$da/dN = C(\Delta K)^m \quad (1.8)$$

Equation 1.9 shows the growth-rate relationship in terms of both K_{max} and ΔK , viz⁽⁴²⁾⁽⁴³⁾:

$$da/dN = C'(K_{max})^n (\Delta K)^p \quad (1.9)$$

The critical and sub-critical extension of a crack can be considered to the result of the mutual competition of two classes fatigue mechanisms. There are two classes of fatigue mechanisms⁽⁴⁴⁾:

1. Intrinsic mechanisms where, as in metals, crack-advance results from damage processes in the crack-tip region, which they are unique to cyclic loading.
2. Extrinsic mechanisms, where the crack-advance mechanisms ahead of the crack-tip is identical to that for monolithic loading, but unloading cycles promoted accelerated crack growth by degrading the degree of crack-tip shielding behind the tip.

Whereas the cyclic processes in metal fatigue are predominantly intrinsic in nature, the cyclic fatigue processes in ceramics are extrinsic.

Several researches have been reported since Williams showed cyclic fatigue degradation in sintered alumina. Under the assumption that there is no enhanced cyclic effect, the time to failure t_c under load is expressed by:

$$t_c = t_s \cdot g^{-1} \cdot \left(\frac{\sigma_s}{\sigma_m} \right)^n \quad (1.10)$$

where t_s time to failure under constant stress, g^{-1} is factor depending on cyclic stress and n . σ_s is maximum stress and σ_m is mean stress of the cyclic stress.

Mechanisms of the cyclic fatigue have been proposed by many researchers and they have been summarized in various reviews. In this review, proposed mechanisms of the cyclic fatigue which are summarized briefly:

1. Crack growth, which results from the generations of vacancies and other lattice defects by dislocation motion at the crack-tip.
2. Acceleration of the crack rate through heat generation at the tips of micro-cracks.
3. Role of localized tensile residual stress which results from thermal shrinkage.
4. Crack extension by sequential loss of interacting forces between crack faces.
5. Role of crack-tip shielding.

In this study, silicon nitride is used for ceramics structure. Finite element method analysis is applied to the new structure, and the maximum tensile stress and stress amplitude have been investigated by varying the dimensions of the structure. Fatigue strengths of ceramics are also considered under several geometrical conditions.

1.4 Wear Surface Damage on the Ceramic Structure

Modern industry requires stronger, harder, more wear resistance and heat resistant materials, which will operate cost effectively and produce high quality products in more hostile environments than ever before. Whenever the wear resistance, dimensional stability, surface quality or friction behavior of conventional materials is

inadequate for use in machine elements subject mainly to mechanical stress, high temperature, chemical attack, a ceramics material makes the better choice. As far as wear is concerned, metals do not fit the bill; they are quickly worn down by the synthetic thread, ultimately resulting in torn threads. In such load case, the relative wear resistance depends on the hardness of the material.

In a sliding contact, the surface is subjected to a set of normal and tangential stresses, which produce deformation and fracture of the material in a surface layer⁽⁴⁵⁾. The process of fracture consists of plastic flow, formation of micro-cracks, and propagation of this crack to eventual failure. When a tangential force is applied to two contacting bodies, resulting in shear traction, the displacement is initially elastic. With increasing force, some amount of the displacement will occur within the contact by plastic flow and slip. Sliding at the contact will require a tangential force sufficiently large to overcome the static friction force⁽¹²⁾. For silicon nitride balls on sapphire flats, brittle fracture and cracking of the flat occurred at large slip amplitudes. At smaller slip amplitudes, wear occurred by micro fracture within the contact area, which produced powdered wear debris⁽⁴⁶⁾. Peterson and Murray reported that the tribological behavior of ceramics is greatly influenced by contact load, temperature and environment⁽⁴⁷⁾. These authors concluded that at low stress levels, ceramics can slide effectively without surface damage.

The effect of temperature on the friction and wear of ceramics has been studied by several investigators. The results show the friction coefficient of alumina increasing at room temperature until 420⁰C, then to decrease at 640⁰C⁽⁴⁸⁾. Similarly behavior was recently reported by Yust and DeVore⁽⁴⁹⁾ for zirconia-toughened alumina. One of these researchers also reported that further increase in temperature to 800⁰C was accompanied

by a decrease in the friction coefficient.

In internal combustion engines, silicon nitride is particularly attractive for thermal oxidation and wear resistance because of its high strength, low density, and good oxidation resistance. Wear of silicon nitride engine component will be expected to occur at elevated temperature in the presence of reactive atmospheres containing combustion product, oxidant, and unburned fuels. Silicon nitride is not thermodynamically stable in such environments. Its resistance to oxidation and corrosion result from the formation of a protective oxidation product layer of SiO_2 , which separates the ceramic from the reactive atmospheres⁽⁵⁰⁾. Therefore, silicon nitride is used for conveying rollers in the hot rolling mills and for rolls in continuous galvanizing line.

1.5 Motivation and Objectives

The information and knowledge of the stresses in the thermal stress and shrink fitting stress of ceramics materials are important because the stress makes the structure to fail mechanically by heating and load. Therefore, attention should be paid to the thermal stress when the ceramics structure is dipped into molten metal and for maximum tensile stress in the ceramics structure because the fracture toughness of ceramics and plasticity is extremely lower than values of steel. Fatigue strength of ceramics is also considered in this study.

To design new structure by finite element method has a potentially to optimum design in new application of ceramics and it minimize the cost and time to renew and maintenance of ceramics component. Thus, the maximum stress and maximum stress amplitude should be decreased by design of structure, change of material and varying

dipping process. From this viewpoint, the objectives of the study in this thesis are to analyze the thermal stress and shrink fitting stress.

1.6 Main Contributions

As the objectives of study on how to reduce thermal and mechanical stresses for cylindrical large ceramics structures give a result of maximum stress and stress amplitude on the ceramics structure. This information is important for designing ceramics structure, whereas, these this abilities used in ceramics component, their reliability will be increasing and their life time will also be prolonged. These contributions will be useful for industries to increase the quality and productivity, and at the same time reduce the cost of production.

1.7 Outline of the Dissertation

The objectives of the study in this thesis constructs on how to reduce the thermal stress, shrink fitting stress and operating stress for cylindrical large ceramics structures by numerical analysis. Zukauskas formula and the finite volume method are applied in this study to calculate surface heat transfer coefficient. Thus, the finite element method is applied to calculate the thermal stresses when the tube is dipped into the crucible with varying dipping speeds. For shrink fitting stress and operating stress, we considered on finite element method. The thesis outline is composed of 6 (six) chapters as following:

Chapter 1 constructs of the background of ceramics application and the outline of thesis.

Chapter 2 briefly constructs the effect of surface heat transfer coefficient α on the thermal stress and thermal stress analysis for simple ceramics tube model dipping vertical and horizontal into molten metal. This chapter shows the results of the surface

heat transfer coefficient α for 2D cylinder and axi-symmetric models, and thermal stress for tubes dipping (vertical and horizontal). The discussion about the results is presented.

Chapter 3 briefly describe and explain the heat transfer coefficient α by finite volume method and thermal stress analysis for simple ceramics tube and tube having protuberance dipping vertical into molten metal. This chapter shows the results of thermal stress for simple tube and tube having protuberance. The discussion about the results is presented.

Chapter 4 give brief explanation on the stress analysis on shrink fitting system used for ceramics conveying rollers. This chapter shows the results of maximum stress for conveying rollers structure by different dimension and properties of material. The discussion about the results is presented.

Chapter 5 give brief focus analyzed on strengths analysis on shrink fitting system used for ceramics rolls in the pickling continuous line. This chapter shows the results of the maximum stress and stress amplitude of the ceramics rolls. The discussion about the results is presented.

Chapter 6 give brief summary of the study.

Reference

1. Richerson, D. W., Modern ceramics engineering: Properties, processing and use in design, Marcel Dekker, Inc, 1982.
2. Barsoum, M. W., Fundamental of ceramics, The McGraw Hill Companies, 1997.
3. Callister, Jr., W. D., Materials science and engineering, An introduction, John Wiley

- &son, Inc, New York, 1990.
4. Bonollo, F., Urban, J., Bonatto, B., and Botter, M., Gravity and low pressure die casting of aluminium alloys: a technical and economical benchmark, *Alluminio E Leghe*, 2005.
 5. Noda, N.A., Hendra, Takase, Y., Li, W., Thermal stress analysis for ceramics stalk in the low pressure die casting machine, *Journal of Solid Mechanics and Material Engineering*, Vol. 3, pp. 1090-1100, 2009.
 6. JFE Techno Research, ナノテクノロジー普及啓蒙調査報告書, p. 95, 2008, 2.
 7. Tsuyunaru, M., Noda, N. A., Hendra and Takase, Y., Maximum stress for shrink fitting system used for ceramics conveying rollers, *Transactions of the Japan Society of Mechanical Engineering*, Vol.74, No.743, pp.919-925, 2008, (in Japanese).
 8. Noda, N.A., Yamada, M., Sano, Y., Sugiyama, S., and Kobayashi, S., Thermal stress for all-ceramics rolls used in molten metal to produce stable high quality galvanized steel sheet, *Engineering Failure Analysis*, Vol. 15, pp. 261-274, 2008.
 9. Fine ceramics technical handbook, Nihon Gakojotsoshinkookai, Ochidarookakoho, p.139, 1998.
 10. Hitachi metals technical report, Vol. 20, p. 25, 2004.
 11. Miki, E., High corrosion resistance and cost reduction by spraying methods, *Plant Engineer*, Vol.21, No.1, 1989 (in Japanese).
 12. Iwata, T., and Mori, H., Material choice for hot run table roller, *Plant Engineer*, Vol.15, No.6, 1983 (in Japanese).
 13. Kingery, W.D., Bowen, H. K., and Uhlmann, D. R., Introduction of ceramics, 2nd ed., Wiley: New York, 1976.

14. Belitskus, D., Fiber and whisker reinforced ceramics for structural applications, Marcel Dekker, pp.1-20, 1993.
15. Jahanmir, S., Friction and wear of ceramics, Marcell Dekker, pp. 3-12, 1994.
16. Machining issue, *Ceram. Bull*, 67 (6), pp. 991-1052, 1988.
17. Zaretsky, E. V., Ceramic bearings for use in gas turbine engines, *ASME Paper*, No.88-GT-138, *American Society of Mechanical Engineers*: New York, 1988.
18. Katz, R. N., and Hannoosh, J. G., Ceramics for high performance rolling element bearings: A review and assessment, *Int. J. High Technol. Ceram.* 1, pp. 69-79, 1985.
19. Dill, J. F., Rolling element bearing technology: Sizing up the Japanese, *Mech. Eng*, pp. 37-40, Dec 1987.
20. Jahanmir, S., Ceramic bearing technology, NIST Special Publication No. 824, U.S. Department of commerce, National Institute of Standards and Technology, Washington, DC: Government Printing Office, 1991.
21. Jahanmir, S., Tribological applications for advanced ceramics, *Mat. Res. Soc. Symp. Proc.* 140, pp. 285-291, 1992.
22. Larsen, R. P., and Vyas, A.D., The outlook for ceramics in heat engines, 1900-2010, SAE Paper No. 880514, *Society of Automotive Engineers*: Dearborn, MI, 1998.
23. Miller. D., V., and Echlin, R., J., Advances in Tunnel Furnace Rolls: Steel Technology, pp. 71-76, June, 2003.
24. Wray, P., Advances structural ceramics, *Tech Monitoring*, SRI International, 1991.
25. Saito, S., Fine ceramics, Elsevier Applied Science Publisher Ltd, 1985.
26. Lenoë, E. M., and Meglen, J. L., *American Ceramics Society Bulletin*, 64, 271, 1985.

27. Jack, K. H., Sialons: A study in materials development, Non-oxide technical and engineering ceramics, Stuart Hampshire, Material research centre, National Institute of Higher Education, Limerick, Ireland, Elsevier applied science, London and New York, pp.1-30, 1986.
28. Dworak, U., Engineering applications of ceramics, High tech ceramics “Viewpoints and perspectives”, Edited by Gernot Kostordz, 1989.
29. W. F. Krupke; M.D. Shinn, J.E. Marion, J.A. Caird, and S.E. Stokowski, "Spectroscopic, optical, and thermomechanical properties of neodymium- and chromium-doped gadolinium scandium gallium garnet", *JOSAB* **3** (1) : 102–114, doi : 10.1364 / JOSAB.3.000102. <http://josab.osa.org/abstract.cfm?id=3938>, 1986.
30. Gogotsi, G. A., Fracture toughness of ceramics and ceramics composites, *Ceramics International*, 29, pp. 777-784, 2003.
31. Zukauskas, A., Heat transfer from tubes in cross flow, In: Hartnett JP, Irvine Jr TF, editors, Advances in heat transfer, Vol.8, New York: Academic Press, 1972, p. 131.
32. Adachi, T., Tamura, Y., and Yoshioka, T., Techniques of automatic operation in continuous galvanizing line, *Kawasaki Steel Technical Report*, Vol.34, 1996, pp.18-25.
33. Nishimura, K., Katayama, K., Kimura, T., Yamaguchi, T., and Ito, M., Newly develop techniques for improving the quality of continuous hot dip plating strips, *Hitachi Technical Report*, Vol. 65(2), 1983, pp. 121-126 (in Japanese).
34. Ferziger, J., H., Peric, M., Computational methods for fluid dynamics, Springer: Heidelberg, 1996.
35. Chang, R., Y., and Yang, W., H., Numerical simulation of mold filling in injection molding using a three-dimensional finite volume approach, *International Journal*

- for Numerical Methods in Fluids*, 37, pp. 125-148, 2000.
36. Jin, G., Honjoh, A., and Awaji, H., Static and cyclic fatigue limits of alumina ceramics, Vol. 108, *Journal of the Ceramics Society of Japan*, pp. 614-616, 2000.
 37. Kawakubo, T., and Komeya, K., Static and cyclic fatigue of precracked ceramics at room temperature, Vol. 37 No.419, *The Society of Materials Science, Japan*, pp. 63-68, 1987.
 38. Kishimoto, H., Ueno, A., and Kawamoto, H., Crack propagation characteristic of sintered Si_3N_4 under static and cyclic loads, Vol. 36, *The Society of Materials Science Japan*, pp. 1122-1127, 1987.
 39. Choi, G., Cyclic fatigue crack growth in silicon nitride: Influences of stress ratio and crack closure, Vol. 43 No.4, *Acta Metall. Material*, pp. 1489-1494, 1995.
 40. Steffen, A. A., Dauskardt, R. H. And Ritchie, R. O., Cyclic fatigue life and crack-growth behavior of microstructurally-small cracks in magnesium-partially-stabilized zirconia ceramics, *Journal of the American Ceramics Society*, 74, pp. 1259-1268, 1991.
 41. Dauskardt, R. H. and Ritchie, R. O., Cyclic fatigue of ceramics, in fatigue of advanced material, (Edited by R.O. Ritchie, R. H. Dauskardt, and B. N. Cox), MCEP Ltd., Edgbaston, pp. 133-151, 1991.
 42. Liu, S. Y. and Chen, I. W., Fatigue of yttria-stabilized zirconia- I. Fatigue damage, fracture origins and lifetime prediction, *Journal of the American Ceramics Society*, 74, pp. 1197-1205, 1991.
 43. Dauskardt, R. H. James, M. R., Porter, J. R. and Ritchie, R. O., Cyclic fatigue-crack growth in SiC-whisker-reinforced alumina ceramic composite: Long and small-crack behavior, *Journal of the American Ceramics Society*, 75, pp.

- 759-771, 1992.
44. Ritchie, R. O., Mechanisms of fatigue-crack propagation in ductile and brittle solids, Vol. 100, *International Journal of Fracture*, pp. 55-83, 1999.
 45. Jahanmir, S., On mechanics and mechanisms of laminar wear particle formation, in *Advances in the Mechanics and Physics of Surfaces*, Vol. 3, R. M. Latanision and T. E. Fischer (Eds), Harwood Academic: New York, pp. 261-331, 1986.
 46. Kennedy, P. J., and Conte, Jr., A. A., Surface damage and mechanics of fretting wear in ceramics, *Friction and wear of ceramics*, Marcell Decker, pp. 79-98, 1994.
 47. Peterson, M. B., and Murray, S. F., Friction behavior of ceramic materials, *Met. Eng. Q.* 7 (2), pp. 22-29, 1967.
 48. Rabinowics, E., Friction and wear at elevated temperatures, WADC Technical Report No. 59-603, 1960.
 49. Yust, C. S., and DeVore, C. E., Wear of zirconia toughened alumina and whisker reinforced zirconia toughened alumina, *Tribol. Trans.* 33, pp. 573-580, 1990.
 50. Mutoh, Y., Miyahara, N., Yamaishi, K., and Oikawa, T., High Temperature Fracture Toughness in Silicon Nitride and Sialon, *Journal of Engineering Materials and Technology*, Vol. 115, pp. 269-272, July, 1993. D. W. Richerson, *Modern Ceramic Engineering*, Dekker:New York, 1982.

Chapter 2

Effect of Heat Transfer Coefficient on the Thermal Stress and Thermal Stress Analysis for Simple Ceramics Tube in the Low Pressure Die Casting Machine

2.1 Introduction

Generally, structural engineering ceramics are widely used in all kinds of engineering fields for their advantages of high temperature resistance, corrosion resistance and abrasion resistance. The ceramics material has been used for auto heat engine, gas turbine, stalk in the low pressure die casting machine as shown in Fig. 2.1, and rolls in the galvanizing line (see Fig. 2.2). Low pressure die casting machine (LPDC) is especially suitable for producing axi-symmetric component such as cylinder head, piston, and brake drum⁽¹⁾⁽²⁾. LPDC is defined as a net shape casting technology in

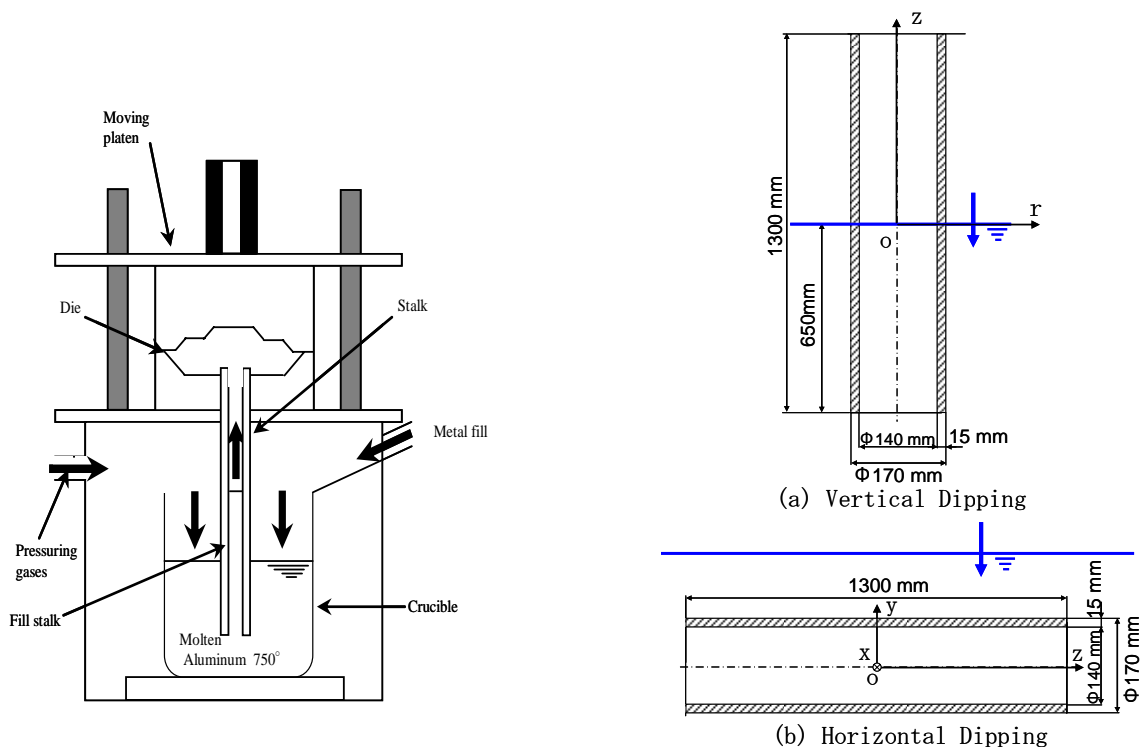


Fig. 2.1 Schema of the low pressure die casting (LPDC) machine
(Note that LPDC is sometimes called “low pressure casting” in Japan)

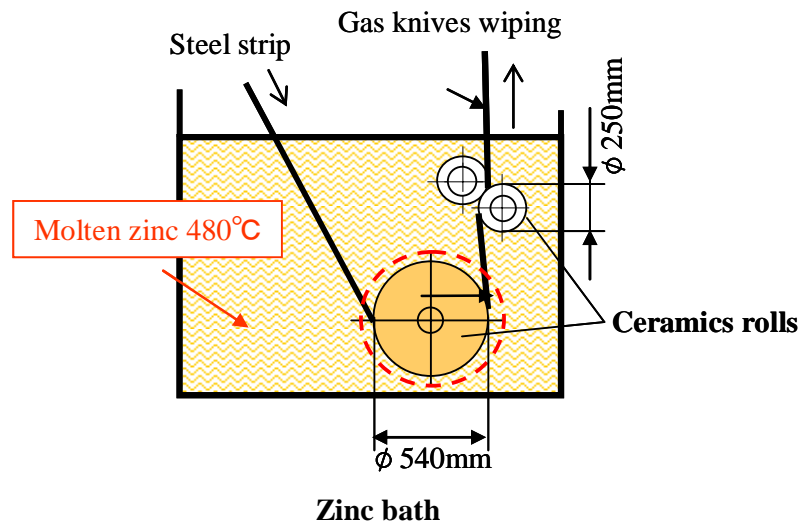


Fig. 2.2 Zinc bath in the galvanizing line

which the molten metal is injected at a high speed and pressured into a metallic die. The LPDC process is playing an increasingly important role in the foundry industry as a low-cost and high-efficiency precision forming technique. Typically operating sequence for the LPDC is shown in Fig. 2.1. The LPDC process is that the permanent die and filling systems are placed over the furnace containing the molten alloy. The filling of the cavity is obtained by forcing the molten metal by means of a pressurized gas in order to rise into a ceramic tube, which connects the die to the furnace. Ceramic tube called stalk has been used in the LPDC. Ceramics tube has high temperature resistance and high corrosion resistance. Previously, the tube was made of cast iron which resulted in spoiling the quality of the product due to the tube partial melted by molten metal. Therefore, ceramics tube was introduced to improve the life time of tube. However, there is still low reliability of ceramics mainly due to low toughness.

As shown in Fig. 2.1, the tube plays a critical function in the LPDC because it receives the molten metal from the crucible. However, attention should be paid to the thermal stress when the ceramics tube is dipped into the molten metal. It is important to

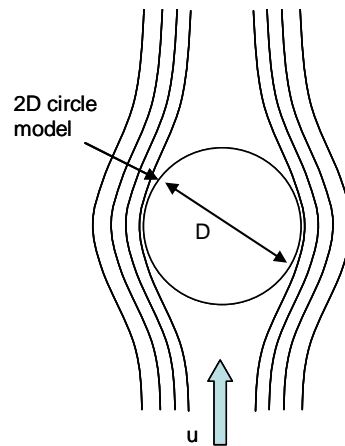


Fig. 2.3 Two-dimensional (2D) circle model

reduce the risk of fracture because of low fracture toughness of ceramics.

In this study the finite volume method is applied to calculate surface heat transfer coefficient. Then, the finite element method is applied to calculate the thermal stresses when the ceramics tube is dipped into the crucible with varying dipping speeds and tube directions.

2.2 Effect of Heat Transfer Coefficient on Thermal Stress when Ceramics Tube Dipping into Molten Metal

The heat transfer coefficient is the primary quantity characterizing the convection heat transfer process. In any given flow situation, it can vary with position on the surface and with time. It depends strongly on the velocity and thermal boundary conditions, as well as the geometry of the body. Since the value of heat transfer coefficient α is not well known, we will check the effect of α on the thermal stress of ceramics. Here, we consider a simple two-dimensional (2D) circular model in Fig. 2.3 to investigate the effect of heat transfer coefficient on the thermal stress because Zukauskas⁽³⁾ proposed a convenient formula to estimate heat transfer coefficient for 2D

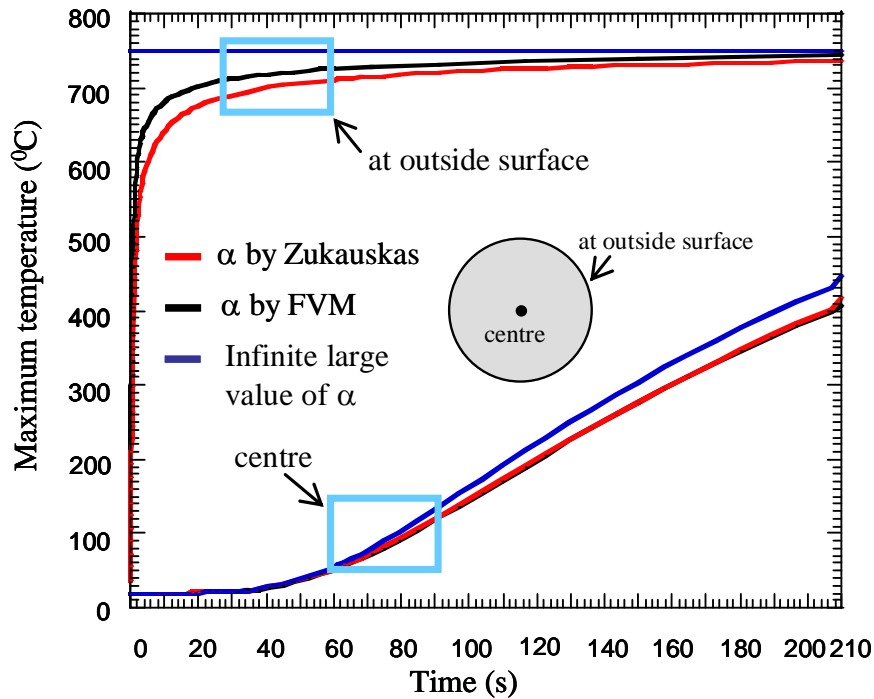


Fig. 2.4 (a) Maximum temperature vs. time relation of 2D model ($u = 25\text{mm/s}$)

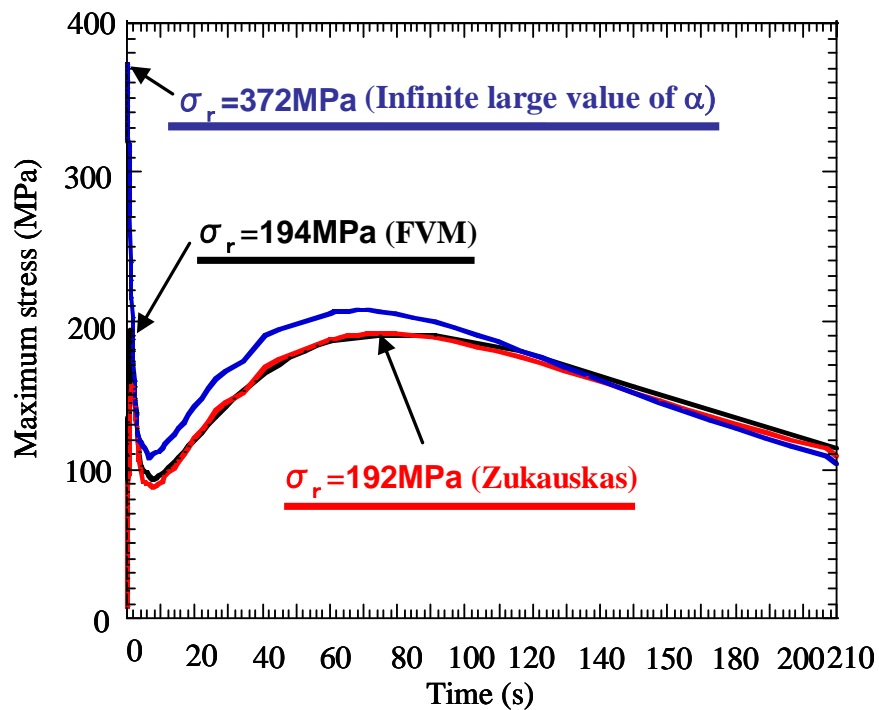


Fig. 2.4 (b) Maximum stress vs. time relation of 2D model ($u = 25\text{mm/s}$)

circle (see Eq. 2.1 in Sec. 2.2.2).

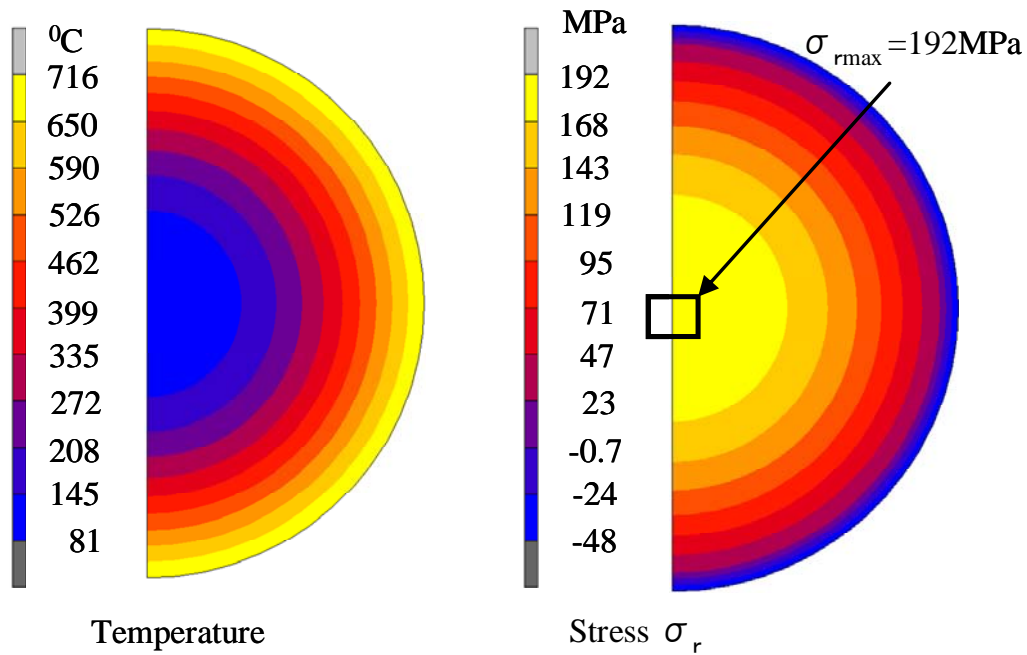


Fig. 2.5 (a) Temperature and stress distribution for 2D model by Zukauskas formula ($u = 25\text{mm/s}$, $t = 75\text{s}$)

In this study, three values of α are assumed for boundary conditions in the finite element method analysis, first $\alpha_{zu} = 6.348 \times 10^3 \text{ W/m}^2 \cdot \text{K}$ by Zukauskas formula⁽⁴⁾⁽⁵⁾; second $\alpha_1 = 10 \times 10^7 \text{ W/m}^2 \cdot \text{K}$ as an infinite large value of α , and third $\alpha_{FVM} = (2.886 - 10.214) \times 10^3 \text{ W/m}^2 \cdot \text{K}$ given by applying finite volume method (FVM) (see Fig. 2.7 (b) in Sec. 2.2.2). Temperature of the molten aluminum is assumed to be 750°C (1023K) (see Table 2.1 in Sec. 2.3), and the initial temperature of the 2D circular model is assumed to be 20°C . Sialon is used for 2D circular model (see Table 2.2 in Sec. 2.3) which has total of 510 elements and 548 nodes. The results are shown in Figs. 2.4 (a) and 2.4 (b). From Fig. 2.4 (b), it is found that the maximum stress $\sigma_{rmax} = 192\text{MPa}$ at $t = 75\text{s}$ when $\alpha_{zu} = 6.348 \times 10^3 \text{ W/m}^2 \cdot \text{K}$. For this case maximum stress is reached in a long time and the value is smaller than the case of the infinite large value of α . Figure 2.5 (a) shows the temperature distribution and maximum stress by Zukauskas formula. The maximum stress appears at the center of circle as shown in Fig. 2.5 (a).

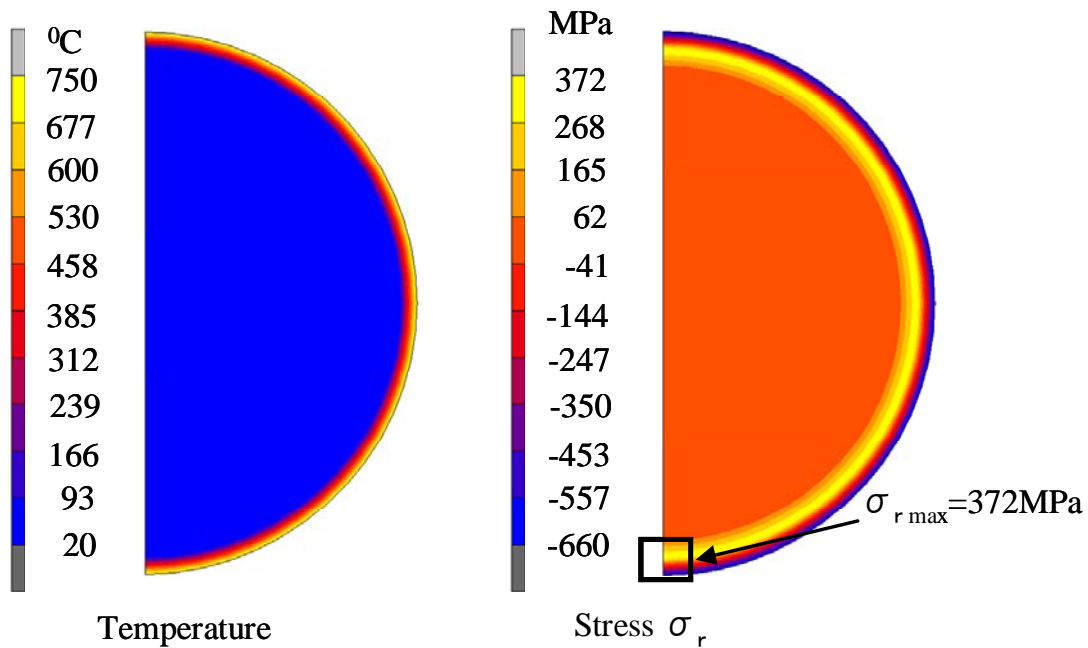


Fig. 2.5 (b) Temperature and stress distribution for 2D model by infinite large value of α ($u = 25 \text{ mm/s}$, $t = 0.01 \text{ s}$)

Utilizing the infinite large value of α , it is found that maximum stress $\sigma_{r \max} = 372 \text{ MPa}$ appears at $t = 0.01 \text{ s}$ when $\alpha_1 = 10 \times 10^7 \text{ W/m}^2 \cdot \text{K}$. For this case the

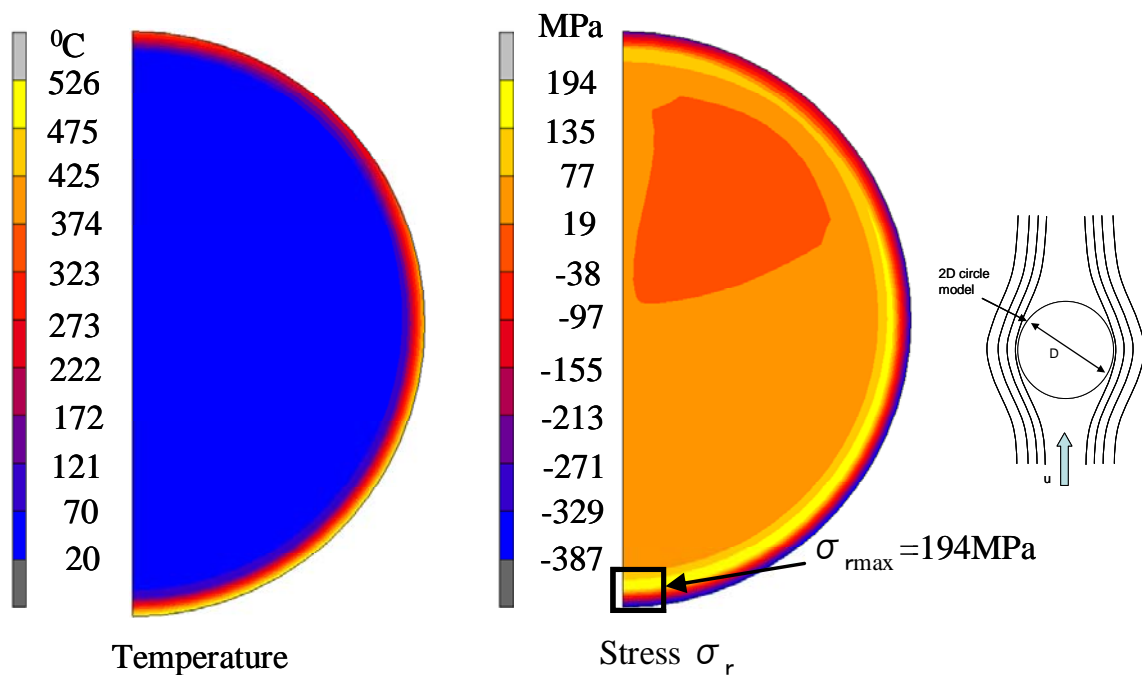


Fig. 2.5 (c) Temperature and stress distribution for 2D model using α analyzed by finite volume method ($u = 25 \text{ mm/s}$, $t = 0.98 \text{ s}$)

maximum stress is reached to be the large value in a short time. Figure 2.5 (b) shows the temperature distribution and maximum stress for the infinite large value of α . As shown in Fig. 2.5 (b), the maximum stress appears near surface. This is due to the large temperature difference appearing near outside surface very shortly.

Figure 2.4 (b) shows maximum stress by finite volume method calculation, $\sigma_{\max} = 194\text{MPa}$ at $t = 0.98\text{s}$ when $\alpha_{\text{FVM}} = (2.886-10.214) \times 10^3 \text{W/m}^2 \cdot \text{K}$ (see Fig. 2.5 (c)). The time to reach the maximum stress is shorter than the Zukauskas formula although the value is almost the same. Figure 2.5 (c) shows the temperature distribution and maximum stress by finite volume method. As shown in Fig. 2.5 (c), the maximum stress appears near the surface at the bottom of circle. This is due to the large temperature difference appearing near the surface at the bottom of circle.

As shown in Fig. 2.4 (b), the maximum stress due to the infinite large value of α is larger than that due to Zukauskas formula and finite volume method. From the above discussion, it is found that just assuming a infinite large value of α does not provide correct thermal stresses. Maximum stress of α using Zukauskas formula and FVM is nearly the same but the time for reaching maximum stress is different. It may be therefore concluded that the finite volume method is desirable for calculating thermal stress of ceramics correctly.

2.3 Analysis Method and Modeling

2.3.1 Analysis Model and Material Properties

In low pressure die casting machine in Fig. 2.1, the ceramics tube is 170mm in diameter and 1300mm in length. Recently it is usually made of ceramic because of its

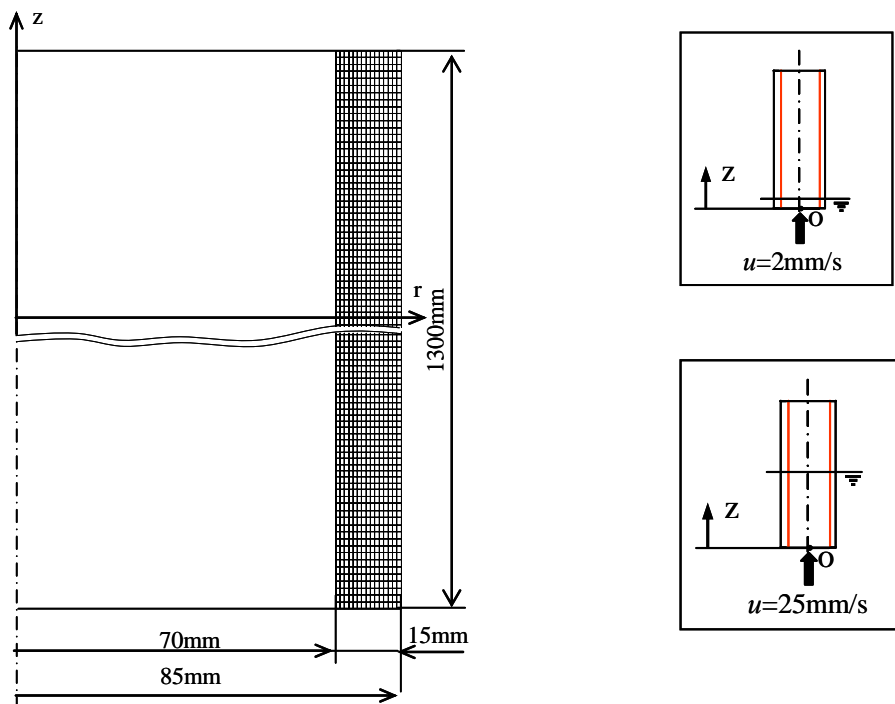


Fig. 2.6 (a) Finite element mesh of vertical tube (No. of elements=19500, No. of nodes=20816)

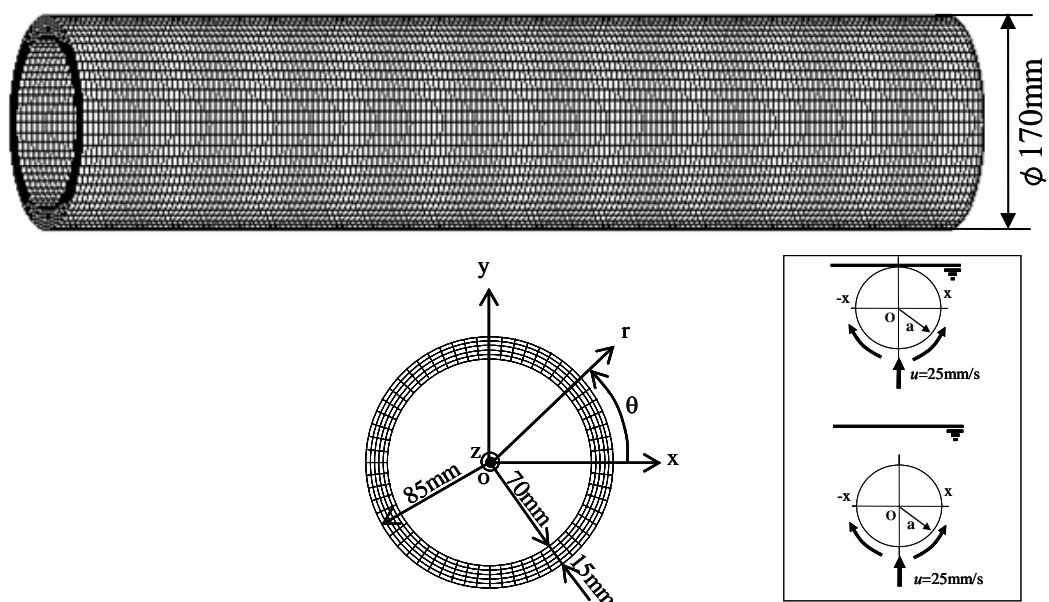


Fig. 2.6 (b) Finite element mesh of horizontal tube (No. of elements=45000, No. of nodes=55986)

high temperature resistance and high corrosion resistance. Temperature of the molten

aluminum is assumed as 750°C, and the initial temperature of the tube is assumed as 20°C. Table 2.1 shows the physical properties of molten aluminum at 750 °C (1023 K)⁽⁴⁾. Table 2.2 shows the properties of ceramics called Sialon⁽⁵⁾⁽⁶⁾ used for the ceramics tube. Axi-symmetric model will be used for vertical tube with total of 19500 elements and 20816 nodes as shown in Fig. 2.6 (a). Three-dimensional model will be used for

Table 2.1 The Physical properties of molten aluminum at 750°C (1023K)

Physical property (dimension)	
Thermal conductivity λ , W/m K	112.2
Roll diameter D , m	0.17
Kinematics viscosity ν , mm ² /s	0.967
Isobaric specific heat C_p , kJ/kg K	1.1
Viscosity η , mPa s	2.2
Constants in Eq. (1) when $Re = 1 \times 10^3 - 2 \times 10^5$ (C_1)	0.26
Constants in Eq. (1) when $Re = 1 \times 10^3 - 2 \times 10^5$ (n)	0.6

Table 2.2 Mechanical properties of Sialon ceramics

Mechanical properties of ceramics (dimension)	Sialon
Thermal conductivity, W/m K	17
Specific heat, J/kg K	650
Coefficient of linear expansion, 1/K	3.0×10^{-6}
Young`s modulus, GPa(kgf/mm ²)	294 (29979)
Specific weight	3.26
Poisson`s ratio	0.27
4 Point bending strength, MPa (kgf/mm ²)	1050 (107)
Fracture toughness, MN/m ^{3/2}	7.5

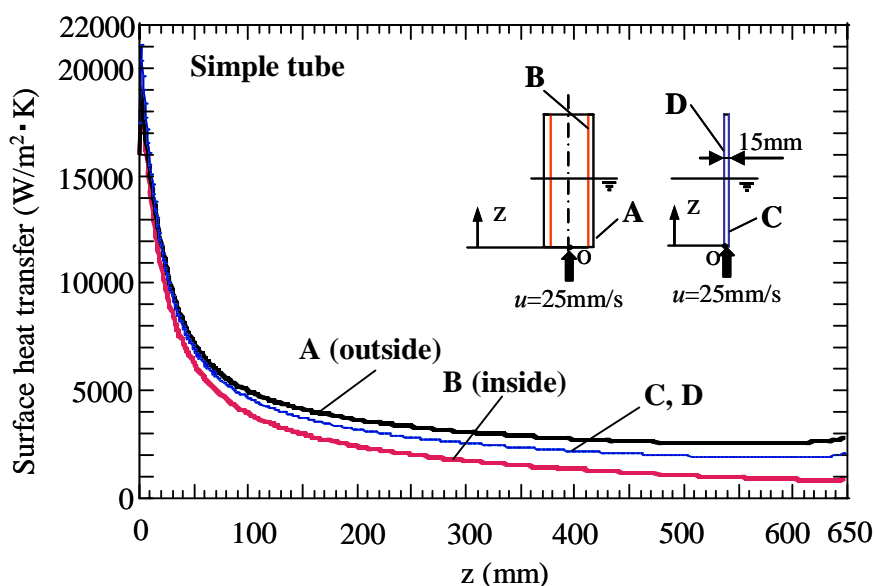


Fig. 2.7 (a) Surface heat transfer coefficient for 2D and axi-symmetry model as a function of z in the molten metal with the velocity $u = 25\text{mm/s}$

horizontal tube with total of 45000 elements and 55986 nodes as shown in Fig. 2.6 (b). Here, 4-node quadrilateral elements will be employed for FEM analysis.

2.3.2 Evaluation for Surface Heat Transfer

To calculate the thermal stress, it is necessary to know the surface heat transfer coefficient α when the tube dips into the molten aluminum. In this study, two-dimensional (2D) and axi-symmetric models are analyzed by using the finite volume method to calculate α when the vertical tube is dipped into the molten metal.

Figure 2.7 (a) shows the results of α for the 2D and axi-symmetric models at $u = 25\text{mm/s}$. For axi-symmetry model, the values of the surface heat transfer coefficient α inner (B) and outer (A) of tube are different as shown in Fig. 2.7 (a). It is confirmed that when the diameter of the axi-symmetric model is infinity the value of α coincides with 2D results.

In case of horizontal tube, the calculation α for a two-dimensional cylinder

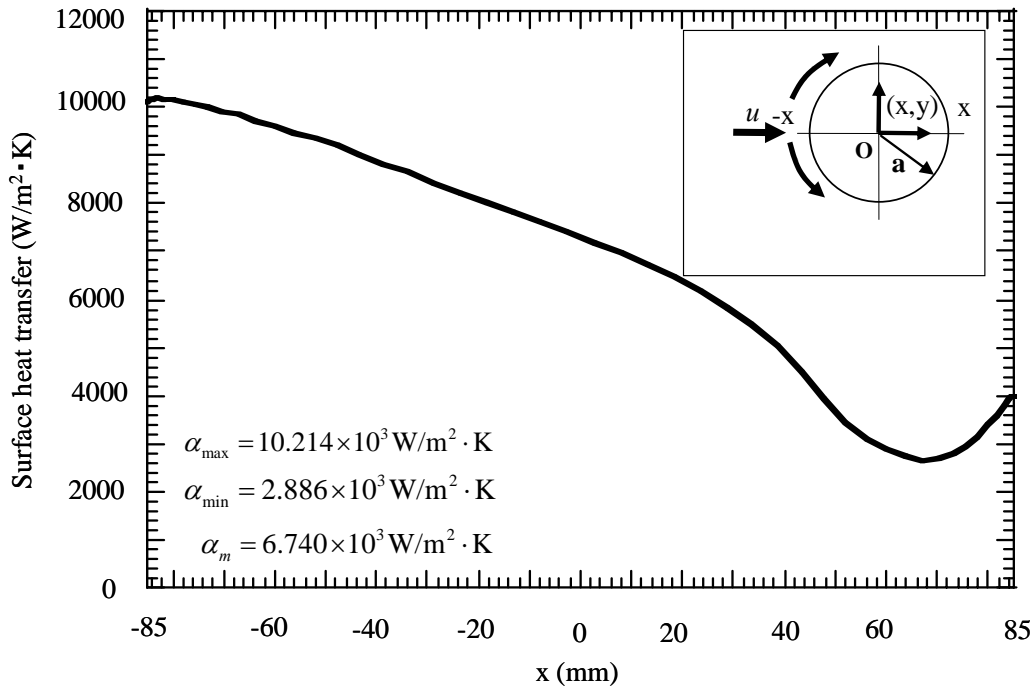


Fig. 2.7 (b) Surface heat transfer as a function of x for two-dimensional cylinder in the molten metal with the velocity $u = 25\text{mm/s}$

using Zukauskas⁽⁵⁾ is compared with the finite volume method calculation. Zukauskas⁽³⁾ proposed the following equation to estimate Nusselt number for a two-dimensional cylinder in the fluid with the velocity u .

$$Nu_m \equiv \frac{\alpha_m \cdot D}{\lambda} = C_1 \cdot Re^n \cdot Pr^{0.37} \cdot \left(\frac{Pr}{Pr_w} \right)^{0.25} \quad (2.1)$$

$$Re = \frac{u \cdot D}{\nu}, \quad Pr = \frac{C_p \cdot \eta}{\lambda} \quad (2.2)$$

where, α_m is the average surface heat transfer coefficient, λ is thermal conductivity, D is the diameter of the cylinder, C_1 and n are constants determined by Reynolds number Re . Also, Pr is Prandtl number, and subscript w denotes the property for temperature of cylinder wall. The velocity u can be calculated by the diameter of the tube divided by the time when the tube dips into the molten aluminum, which is usually $u = 2-25\text{mm/s}$. The values of isobaric specific heat C_p , viscosity η , kinematics viscosity ν are taken from reference⁽⁴⁾, as shown in Table 2.1. Substituting these into

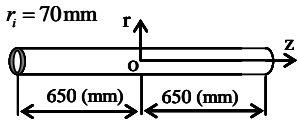
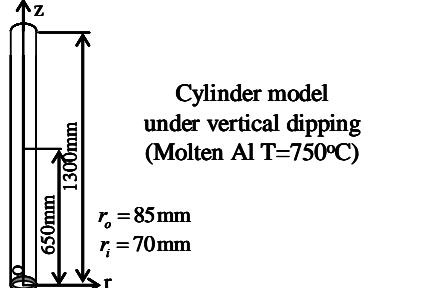
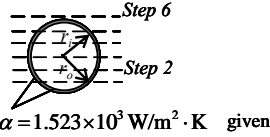
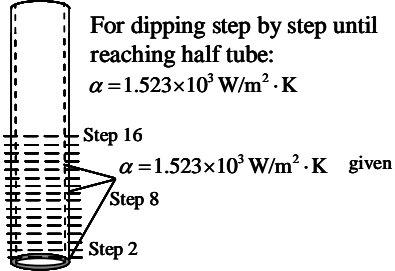
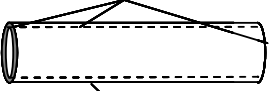
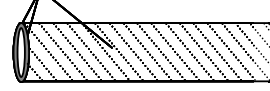
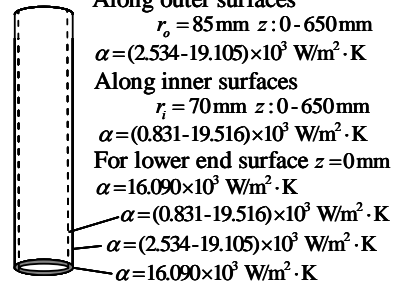
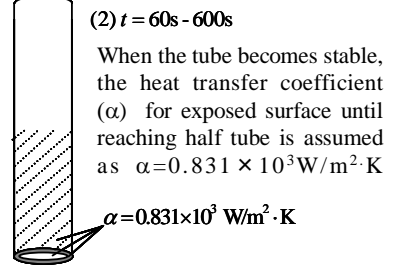
Eqs. (2.1) and (2.2), Nu_m is calculated for the determination of α_m , which is,

$$\alpha_m = 1.523 \times 10^3 \text{ W/m}^2 \cdot \text{K} \quad (\text{when } u = 2 \text{ mm/s}). \quad (2.3)$$

$$\alpha_m = 6.348 \times 10^3 \text{ W/m}^2 \cdot \text{K} \quad (\text{when } u = 25 \text{ mm/s}). \quad (2.4)$$

Figure 2.7 (b) shows the distribution of surface heat transfer coefficient as a function

Table 2.3 Assumption of surface heat transfer coefficient α $\text{W/m}^2 \cdot \text{K}$

Model	<p>Cylinder model under horizontal dipping (Molten Al T=750°C)</p> <p>$r_o = 85 \text{ mm}$ $r_i = 70 \text{ mm}$</p> 	<p>Cylinder model under vertical dipping (Molten Al T=750°C)</p> <p>$r_o = 85 \text{ mm}$ $r_i = 70 \text{ mm}$</p> 
<p>$u = 2 \text{ mm/s}$</p>	<p>For dipping step by step: $\alpha = 1.523 \times 10^3 \text{ W/m}^2 \cdot \text{K}$</p>  <p>$\alpha = 1.523 \times 10^3 \text{ W/m}^2 \cdot \text{K}$ given</p>	<p>For dipping step by step until reaching half tube: $\alpha = 1.523 \times 10^3 \text{ W/m}^2 \cdot \text{K}$</p>  <p>$\alpha = 1.523 \times 10^3 \text{ W/m}^2 \cdot \text{K}$ given</p>
<p>$u = 25 \text{ mm/s}$</p>	<p>(1) $t = 0 - 60 \text{ s}$ Along outer surfaces $r_o = 85 \text{ mm}$ $\alpha = (2.886 - 10.214) \times 10^3 \text{ W/m}^2 \cdot \text{K}$ At both ends $z = \pm 650 \text{ mm}$ $\alpha = 2.886 \times 10^3 \text{ W/m}^2 \cdot \text{K}$ Along inner surfaces $r_i = 70 \text{ mm}$ $\alpha = 2.886 \times 10^3 \text{ W/m}^2 \cdot \text{K}$ $\alpha = 2.886 \times 10^3 \text{ W/m}^2 \cdot \text{K}$</p>  <p>$\alpha = (2.886 - 10.214) \times 10^3 \text{ W/m}^2 \cdot \text{K}$</p> <p>(2) $t > 60 \text{ s}$ When the tube becomes stable, the heat transfer coefficient (α) for all exposed surface is assumed as $\alpha = 2.886 \times 10^3 \text{ W/m}^2 \cdot \text{K}$</p>  <p>$\alpha = 2.886 \times 10^3 \text{ W/m}^2 \cdot \text{K}$</p>	<p>(1) $t = 0 - 60 \text{ s}$ Along outer surfaces $r_o = 85 \text{ mm } z : 0 - 650 \text{ mm}$ $\alpha = (2.534 - 19.105) \times 10^3 \text{ W/m}^2 \cdot \text{K}$ Along inner surfaces $r_i = 70 \text{ mm } z : 0 - 650 \text{ mm}$ $\alpha = (0.831 - 19.516) \times 10^3 \text{ W/m}^2 \cdot \text{K}$ For lower end surface $z = 0 \text{ mm}$ $\alpha = 16.090 \times 10^3 \text{ W/m}^2 \cdot \text{K}$ $\alpha = (0.831 - 19.516) \times 10^3 \text{ W/m}^2 \cdot \text{K}$ $\alpha = (2.534 - 19.105) \times 10^3 \text{ W/m}^2 \cdot \text{K}$ $\alpha = 16.090 \times 10^3 \text{ W/m}^2 \cdot \text{K}$</p>  <p>(2) $t = 60 \text{ s} - 600 \text{ s}$ When the tube becomes stable, the heat transfer coefficient (α) for exposed surface until reaching half tube is assumed as $\alpha = 0.831 \times 10^3 \text{ W/m}^2 \cdot \text{K}$</p>  <p>$\alpha = 0.831 \times 10^3 \text{ W/m}^2 \cdot \text{K}$</p>

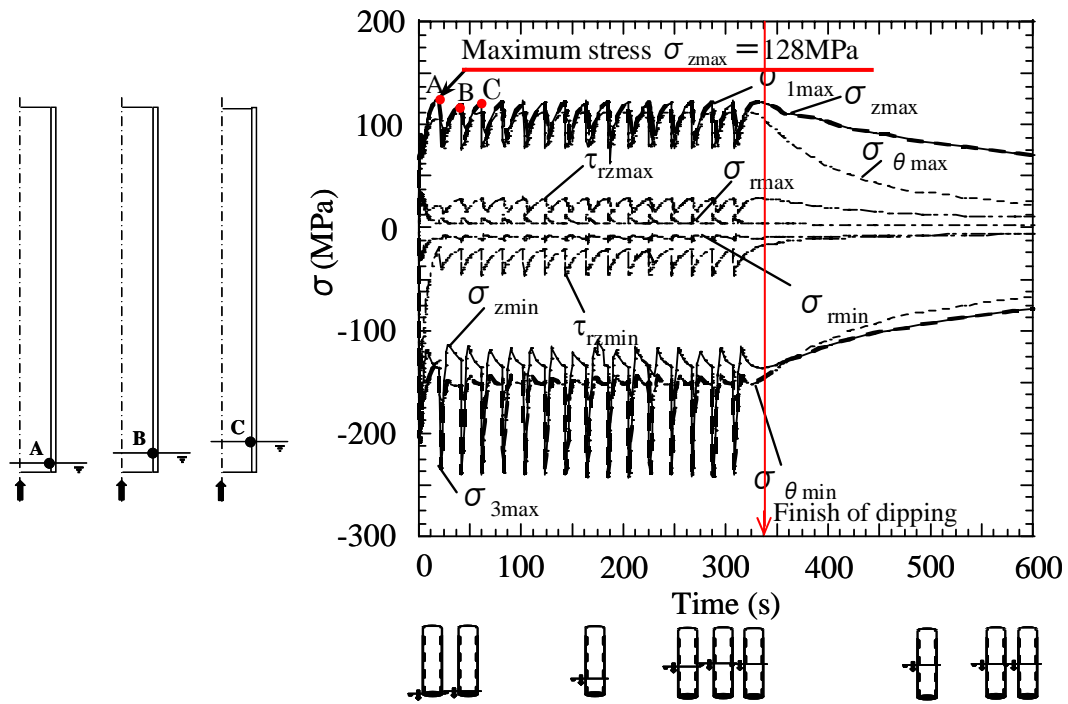
of x for two-dimensional cylinder in the molten metal with the velocity $u = 25\text{mm/s}$. The results for $a = 85\text{mm}$ in molten aluminum are obtained by the application of the finite volume method for two-dimensional cylinder model in the molten metal with the velocity $u = 25\text{mm/s}$. The results in Fig. 2.7 (b) are used in horizontal tubes for calculation of thermal stress. In Fig. 2.7 (b), the average value of $\alpha_m = 6.740 \times 10^3 \text{W/m}^2 \cdot \text{K}$ for $a = 85\text{mm}$ which is in agreement with Eq. (2.4). Table 2.3 shows the values of surface heat transfer coefficient α for simple tube when the vertical and horizontal tubes are dipped into molten metal at $u = 2\text{mm/s}$ and $u = 25\text{mm/s}$.

2.4 Thermal Stress for Vertical Tube

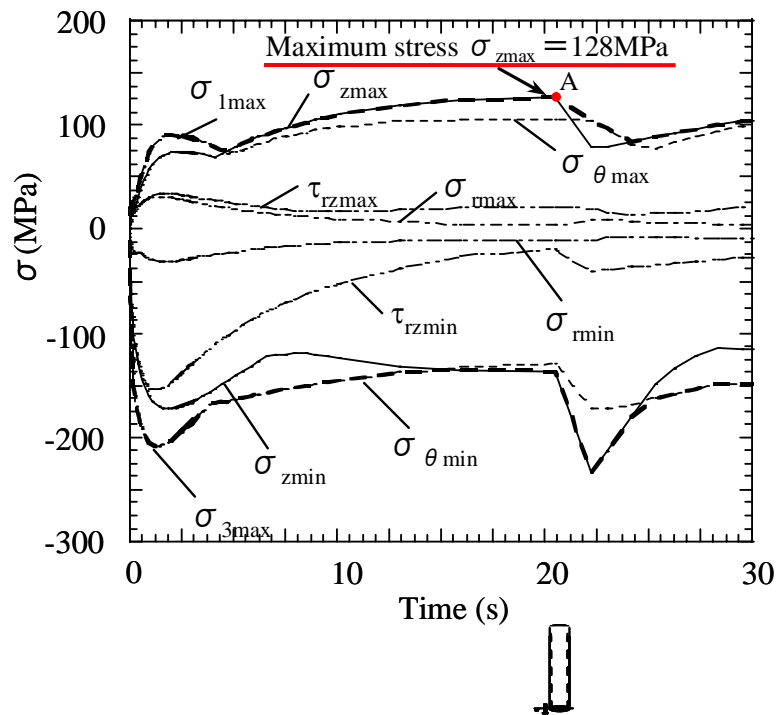
The vertical tube model with the length of 1300mm as shown in Fig. 2.1 (a) is considered when half of the tube is dipping into molten aluminum at the speeds of $u = 2\text{mm/s}$ and $u = 25\text{mm/s}$. It should be noted that $u < 2\text{mm/s}$ is too slow and not convenient and $u > 25\text{mm/s}$ is too fast and not safe. Here, maximum tensile stress is important because ceramics is strong for compressive stress. Therefore, maximum tensile stress will be discussed in this study.

2.4.1 Results for Dipping Slowly

When $u = 2\text{mm/s}$, a constant value $\alpha_m = 1.523 \times 10^3 \text{W/m}^2 \cdot \text{K}$ in Eq. (2.3) is applied for dipping step by step along the inner and outer surfaces ($r_i = 70\text{mm}$, $r_o = 85\text{mm}$) until reaching half tube. Since it takes 328s for dipping completely, sixteen types of partially dipping models are considered as shown in the Table 2.3, and the value $\alpha_m = 1.523 \times 10^3 \text{W/m}^2 \cdot \text{K}$ is applied to the whole surface touching molten aluminum.



(a)



(b). Enlarge time scale in Fig. (a)

Fig. 2.8 Maximum stresses vs. time relation of vertical tube ($u = 2\text{mm/s}$)

tensile principle stress σ_1 , maximum compressive principle stress σ_3 and maximum stresses components σ_r , σ_θ , σ_z . Since the maximum shear stresses τ_{rz} , $\tau_{\theta z}$, $\tau_{r\theta}$ are within 25% of σ_{zmax} , only the largest shear stress τ_{rz} is indicated. From Fig. 2.8 it is

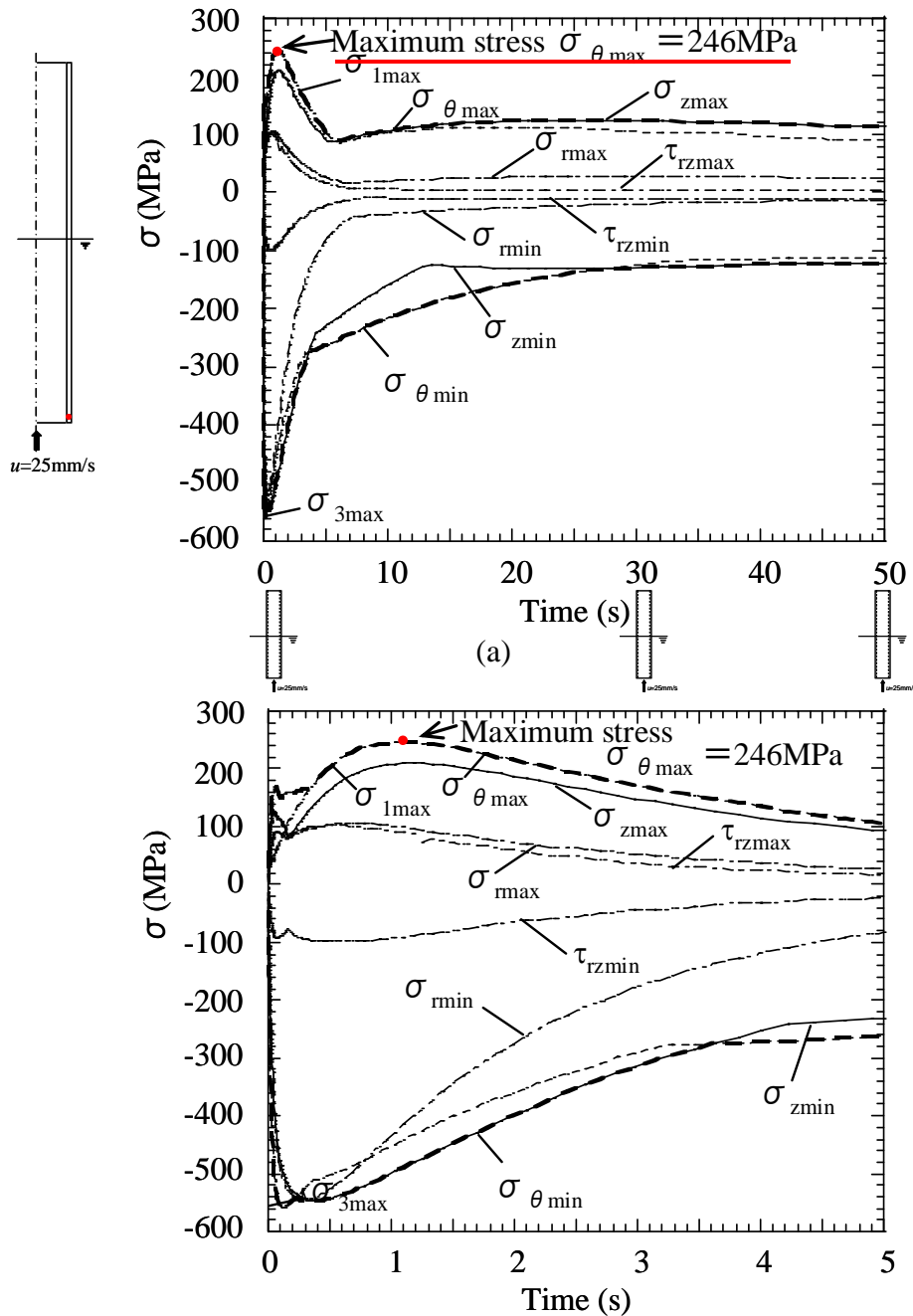


Fig. 2.9 Maximum stresses vs. time relation of vertical tube ($u = 25\text{mm/s}$)

seen that $\sigma_{z_{\max}}$ coincides with σ_1 at $t = 20.5\text{s}$, and $\sigma_{z_{\min}}$ coincides with σ_3 at $t = 165\text{s}$. Therefore, only $\sigma_{z_{\max}}$ and $\sigma_{z_{\min}}$ will be discussed later because they are almost equivalent to the maximum stresses σ_1 and σ_3 , respectively. The stress $\sigma_{z_{\max}}$ has the peak value of 128MPa at $t = 20.5\text{s}$. The maximum thermal stress $\sigma_{z_{\max}} = 128\text{MPa}$ does not decrease while half of the tube is dipping into the molten metal. Then, the stress decreases gradually after half dipping is finished. Since sixteen types of partially dipping model are utilized, fluctuation of stresses appears as shown in Fig. 2.8.

2.4.2 Results for Dipping Fast

In this study, the finite volume method is used to calculate heat transfer coefficient for dipping fast for thermal stress analysis. In this case, the lower half part of the vertical tube is assumed already in the molten aluminum and molten metal has a velocity of $u = 25\text{mm/s}$.

Thermal stress is considered when the tube in Fig. 2.1 dips into molten aluminum fast at $u = 25\text{mm/s}$. The surface heat transfer is applied as follows (see Table 2.3):

1. When $t = 0\text{-}60\text{s}$, the values in Table 2.3 $\alpha = (0.831\text{-}19.516) \times 10^3 \text{W/m}^2 \cdot \text{K}$ is applied at the inner and outer surfaces for simple tube. Also the maximum value, in Fig. 2.7 (a), $\alpha = 16.090 \times 10^3 \text{W/m}^2 \cdot \text{K}$ is applied at the lower end surface ($z = 0\text{mm}$) for simple tube.
2. When $t > 60\text{s}$, the minimum value, in Fig. 2.7 (a) $\alpha = 0.831 \times 10^3 \text{W/m}^2 \cdot \text{K}$ is applied for the exposed surface until reaching half tube for simple tube.

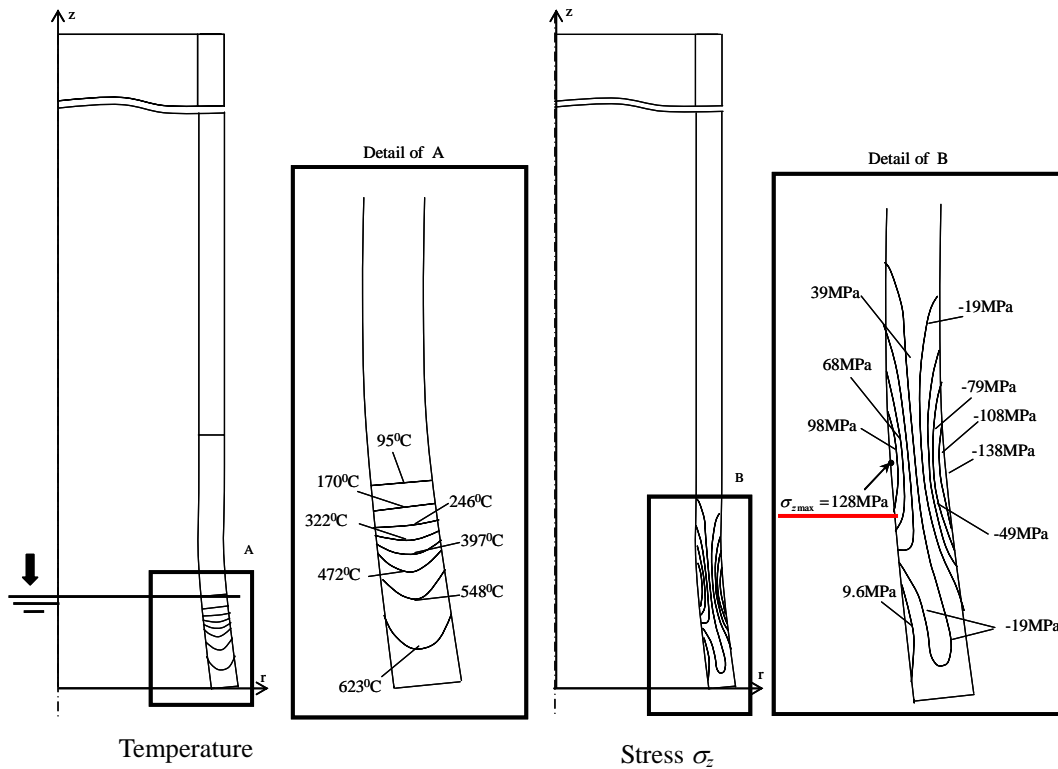


Fig. 2.10 Temperature and stress σ_z distributions of vertical tube ($u = 2\text{mm/s}$ at time $t = 20.5\text{s}$), displacement $\times 50$

Figure 2.9 shows the maximum value of stresses σ_1 , σ_r , σ_θ , σ_z and τ_{rz} . As shown in Fig. 2.9, the maximum tensile stress $\sigma_1 = \sigma_\theta$ increases in a short time. After taking a peak value $\sigma_{\theta\text{max}} = 246\text{MPa}$ at $t = 1.1\text{s}$ for simple tube, it is decreasing. The maximum value 246MPa is larger by twice than that of 128MPa for dipping slowly.

2.4.3 Comparison between Dipping Slowly and Fast

The temperature and stress distributions of vertical tubes are indicated in Figs. 2.10 and 2.11. Figure 2.10 shows temperature and stress distributions of σ_z at $t = 20.5\text{s}$, where the maximum stress $\sigma_{z\text{max}} = 128\text{MPa}$ appears for the tube dipping slowly. Figure 2.11 shows temperature and stress distributions σ_θ at $t = 1.1\text{s}$ where the maximum stress $\sigma_{\theta\text{max}} = 246\text{MPa}$ appears for the tube dipping fast. For dipping slowly at $u = 2\text{mm/s}$, the maximum stress σ_z appears at the inner surface of the tube $r_i = 70\text{mm}$ just above the dipping level of molten aluminum (see Fig. 2.10). This is due

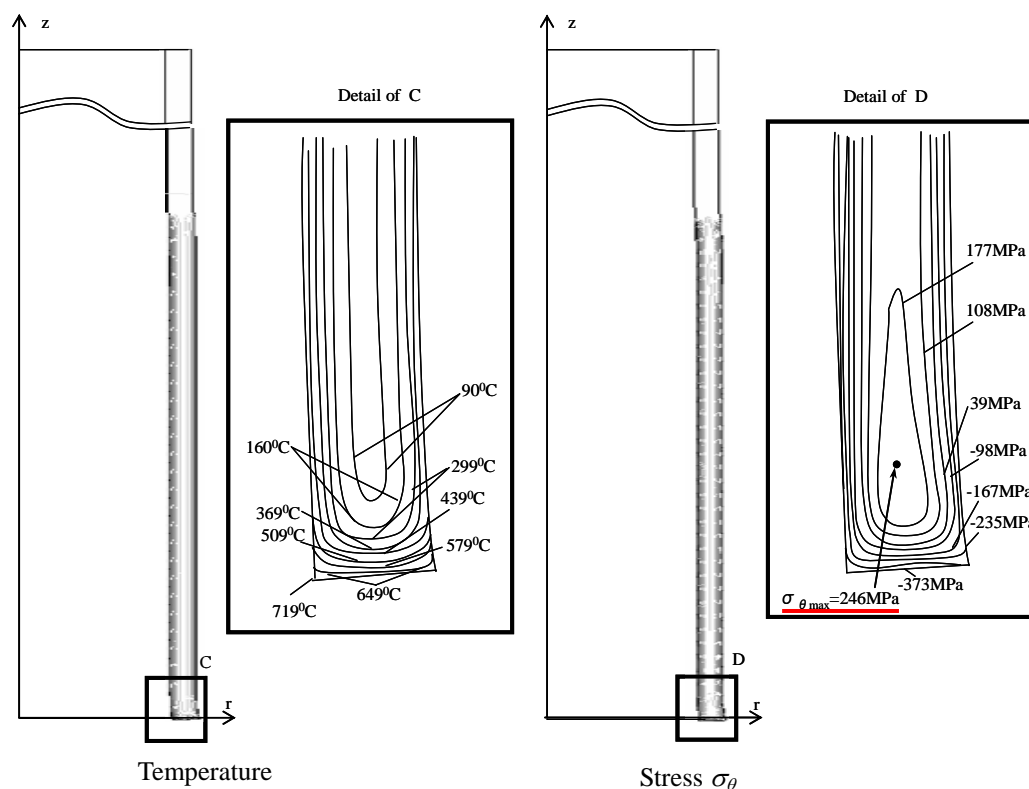


Fig. 2.11 Temperature and stress σ_{θ} distributions of vertical tube ($u = 25\text{mm/s}$ at time $t = 1.1\text{s}$), displacement $\times 50$

to the bending moment caused by the thermal expansion of the dipped portion of the tube. On the other hand, for the fast dipping at $u = 25\text{mm/s}$, the maximum stress $\sigma_{\theta\text{max}}$ appears at the inside of the thickness as shown in Fig. 2.11. This is due to the large temperature difference appearing in the thickness direction. In the previous study⁽⁷⁾, it is found that micro-crack formation appears under 60%-80% of the final fracture stress independent of the position of the maximum stress. Therefore, in this paper we consider the maximum value of tensile stress in order to compare the results for dipping fast and dipping slowly.

2.5 Thermal Stress for Horizontal Tube

Thermal stress is considered when the horizontal tube in Fig. 2.1 (b) dips into

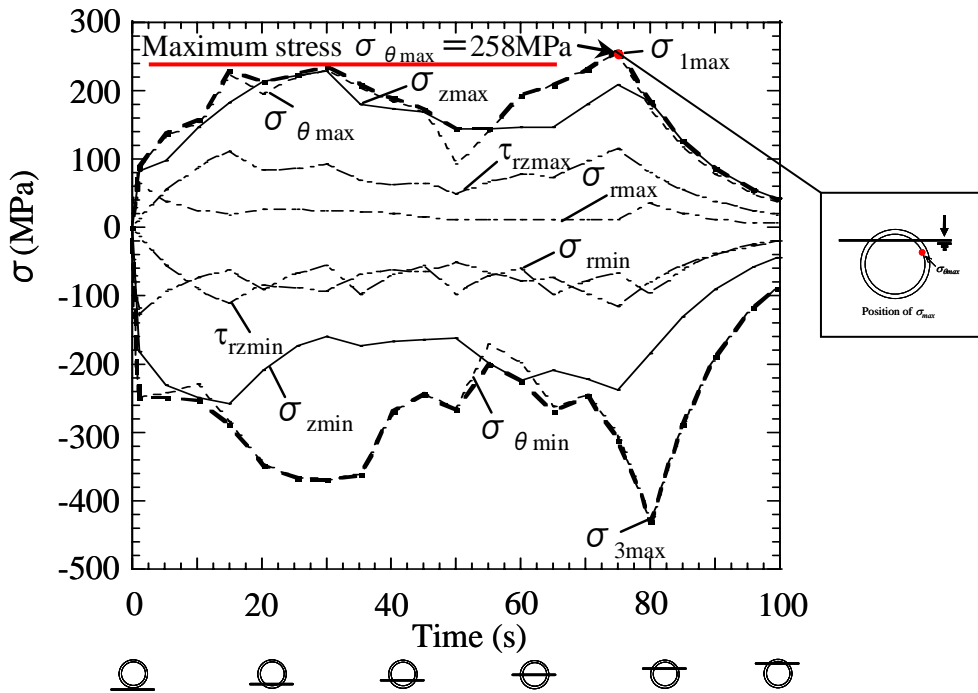


Fig. 2.12 Maximum stresses vs. time relationship of horizontal tube ($u = 2\text{mm/s}$)

molten aluminum at the speeds of $u = 2\text{mm/s}$ and $u = 25\text{mm/s}$. Three-dimensional model will be used for horizontal tube with a total of 45000 elements and 55986 nodes as shown in Fig. 2.6 (b).

2.5.1 Results for Dipping Slowly

When $u = 2\text{mm/s}$, a constant value $\alpha_m = 1.523 \times 10^3 \text{W/m}^2 \cdot \text{K}$ (same to the case of vertical tube) is applied for dipping step by step along the inner and outer surfaces ($r_i = 70\text{mm}$, $r_o = 85\text{mm}$). Since it takes 210s for dipping completely, six types of partially dipping models are considered as shown in the Table 2.3, and the value $\alpha_m = 1.523 \times 10^3 \text{W/m}^2 \cdot \text{K}$ is applied to the surface touching molten aluminum. Figure 2.12 shows maximum values of stresses σ_r , σ_θ , σ_z and τ_{rz} . In Fig. 2.12, the maximum tensile stress $\sigma_{\theta\max} = 258\text{MPa}$ appears at $t = 75\text{s}$ and compressive stress $\sigma_{\theta\min} = -430\text{MPa}$ at $t = 80.1\text{s}$.

2.5.2 Results for Dipping Fast

Similarly, with the dipping fast for vertical tube in the simple model, the finite volume method is used to calculate heat transfer coefficient for thermal stress for

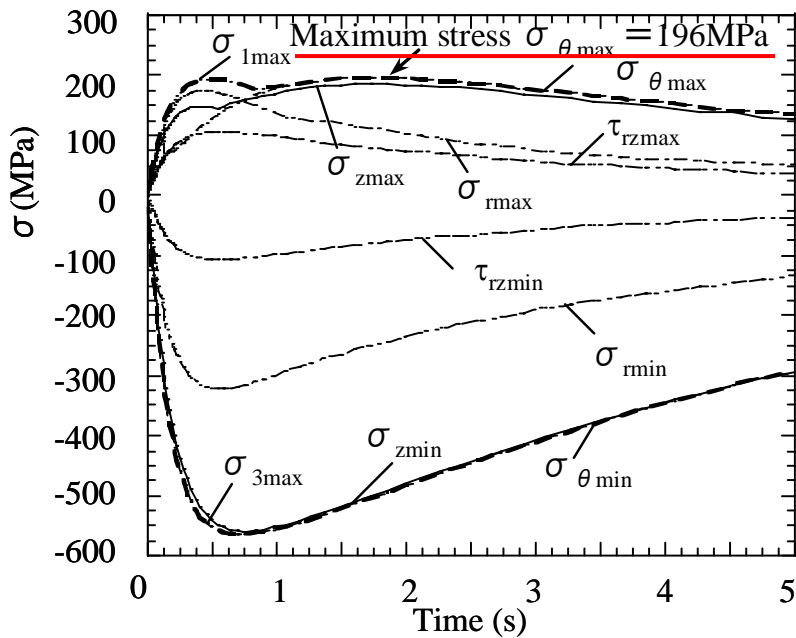
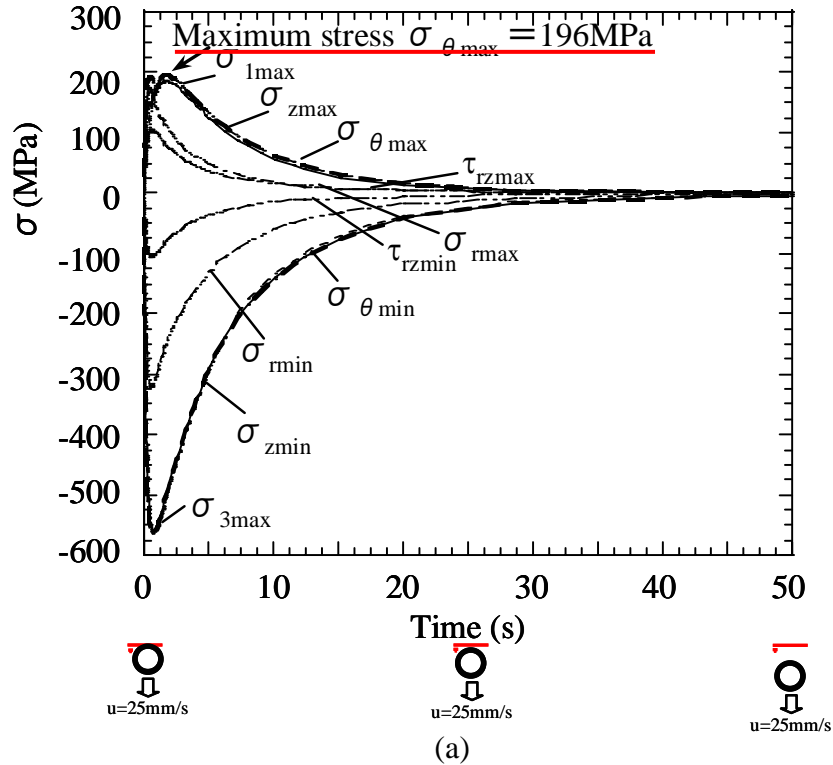


Fig. 2.13 Maximum stresses vs. time relationship of horizontal tube ($u = 25\text{mm/s}$)

horizontal tube dipping fast. In this case, the whole part of horizontal tube is assumed in the molten aluminum because it takes 6.8s to dip into the bath and 47s to the horizontal tube position.

Thermal stress is considered when the horizontal tube in Fig. 2.1 (b) dips into the molten aluminum fast at $u = 25\text{mm/s}$. Here, the surface heat transfer is applied in the following way:

1. When $t = 0\text{-}60\text{s}$, the values in Table 2.3 $\alpha = (2.886\text{-}10.214) \times 10^3 \text{ W/m}^2 \cdot \text{K}$ are applied along the outer surface ($r_o = 85\text{mm}$). Also the minimum value in Table 2.3 $\alpha = 2.886 \times 10^3 \text{ W/m}^2 \cdot \text{K}$ is applied at the inner surface ($r_i = 70\text{mm}$) and tube ends $z = \pm 650\text{mm}$.
2. When $t > 60\text{s}$, the minimum value in Table 2.3 $\alpha = 2.886 \times 10^3 \text{ W/m}^2 \cdot \text{K}$ is applied for all exposed surfaces.

Figure 2.13 shows maximum values of stresses σ_r , σ_t , σ_θ , σ_z and τ_{rz} . As shown in Fig. 2.13 the maximum tensile stress increases in a short time, and has a peak value $\sigma_{\theta\text{max}} = 196\text{MPa}$ at $t = 1.73\text{s}$ and compressive stress $\sigma_{\theta\text{min}} = -564\text{MPa}$ at $t = 0.7\text{s}$.

2.5.3 Comparison between Dipping Slowly and Fast

Figure 2.14 (a) shows the temperature and stress distributions σ_θ for horizontal

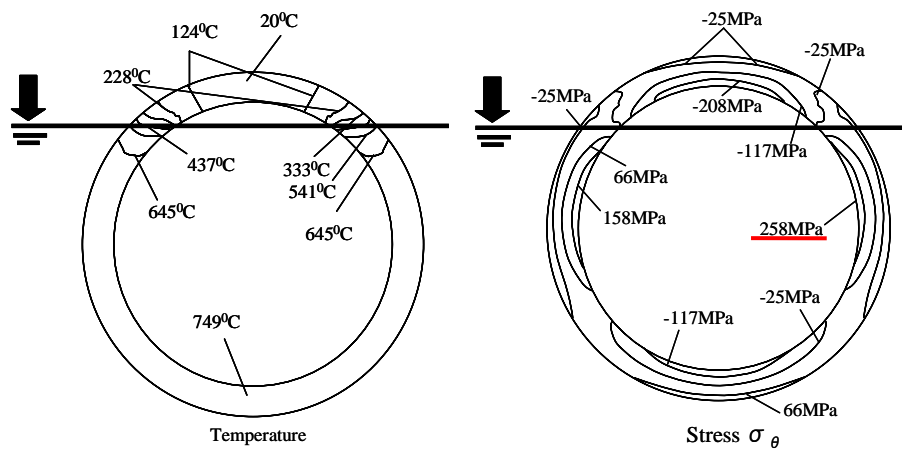


Fig. 2.14 (a) Temperature and stress σ_θ distributions of horizontal tube at both ends $z = \pm 650\text{mm}$ ($u = 2\text{mm/s}$ at time $t = 75\text{s}$)

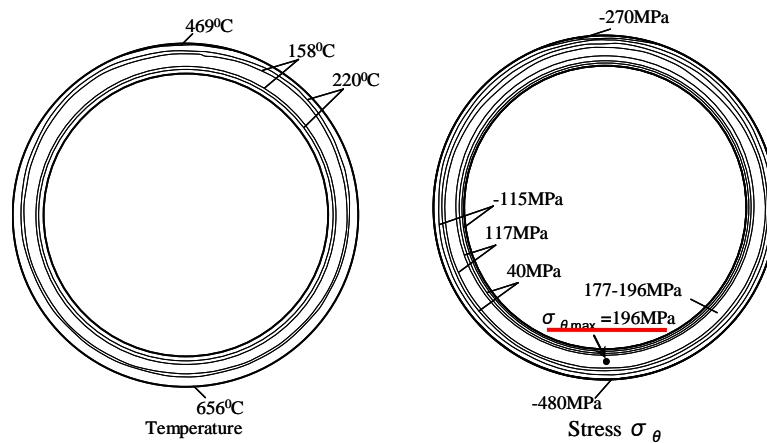


Fig. 2.14 (b) Temperature and stress σ_θ distributions of horizontal tube near the both ends at $z = 615\text{mm}$ ($u = 25\text{mm/s}$ at time $t = 1.73\text{s}$)

tube at both ends where $\sigma_{\theta\text{max}} = 258\text{MPa}$ appears at $t = 75\text{s}$ for the tube dipping slowly. Figure 2.14 (b) shows temperature and stress distributions σ_θ near both ends, where $\sigma_{\theta\text{max}} = 196\text{MPa}$ appears at $t = 1.73\text{s}$ for the tube dipping fast.

For dipping slowly, as shown in Fig. 2.15 (a) the maximum stress $\sigma_{\theta\text{max}}$ appears at the inner surface of the tube ends $z = \pm 650\text{mm}$. In this case, the circular cross section becomes elliptical because of temperature difference between the dipped and

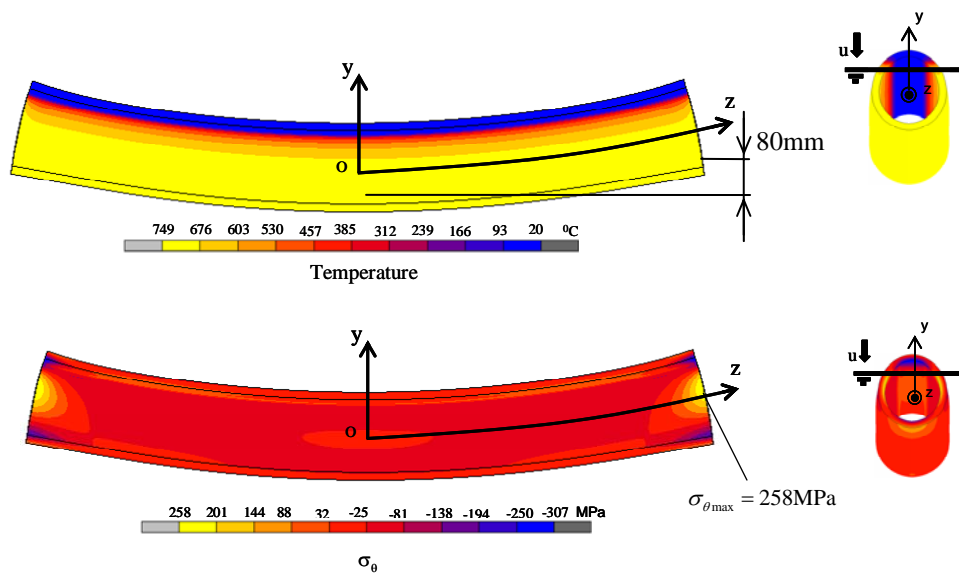


Fig. 2.15 (a) Temperature and stress σ_θ distributions of horizontal tube ($u = 2\text{mm/s}$ at time $t = 75\text{s}$), displacement $\times 30$

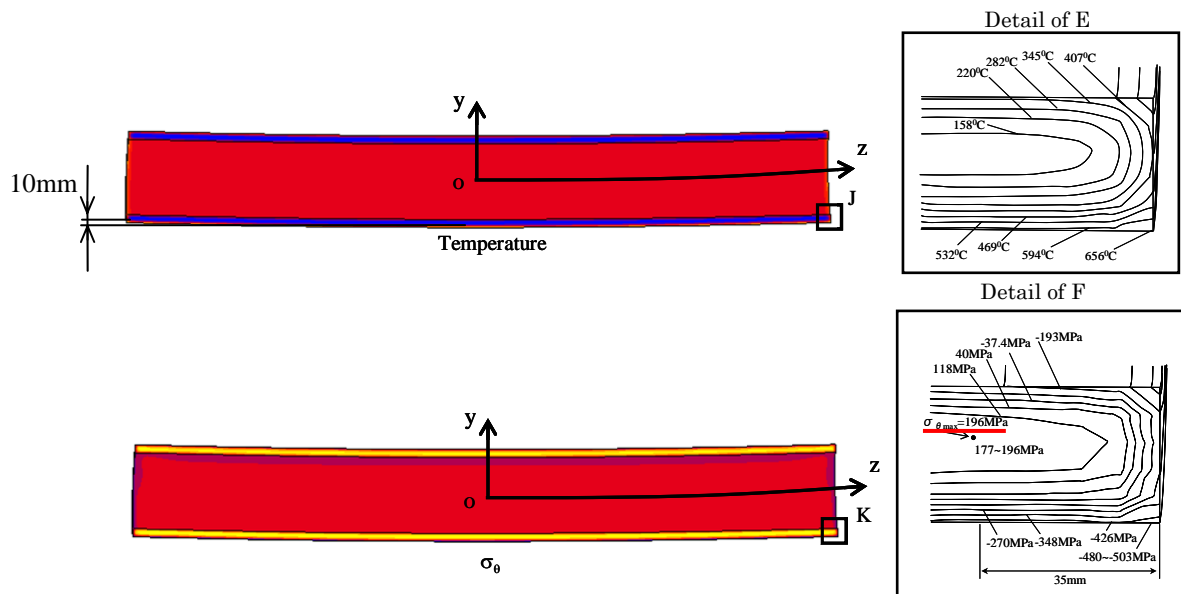


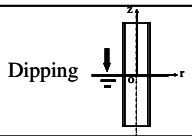
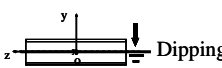
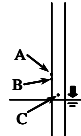
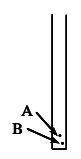
Fig. 2.15 (b) Temperature and stress σ_θ distributions of horizontal tube ($u = 25\text{mm/s}$ at time $t = 1.73\text{s}$), displacement $\times 30$

upper parts. In other words, the maximum stress $\sigma_{\theta_{max}}$ appears due to asymmetric deformation. For dipping fast as shown in Fig. 2.15 (b), the temperature and stress distributions are similar to the ones of vertical tube dipping fast in Fig. 2.11. In other words, for dipping fast, the deformation is almost axi-symmetric. The larger stress appears much more shortly than the case of $u = 2\text{mm/s}$. Therefore horizontal tubes should dip fast at $u = 25\text{mm/s}$ rather than slowly at $u = 2\text{mm/s}$ to reduce the thermal stress.

2.6 Comparison between the Results of Vertical and Horizontal Tubes

Table 2.4 shows the maximum values of tensile stresses for each tube. For vertical tube, dipping slowly for ceramics tube may be suitable for reducing the thermal stresses because dipping fast causes larger temperature difference in the thickness direction, which results in larger thermal stresses. On the other hand, for horizontal tube, dipping fast may reduce the thermal stress although in this case similar large

Table 2.4 the maximum values of tensile stresses for simple tube

	Vertical tube		Horizontal tube	
Model				
$u=2\text{mm/s}$	At $t=20.5\text{s}$ (maximum stress appears) $\sigma_1 = 128\text{MPa}$ (A) $\sigma_z = 128\text{MPa}$ (A) $\sigma_\theta = 105\text{MPa}$ (B) $\sigma_r = 4\text{MPa}$ (A) $\tau_{rz} = 21\text{MPa}$ (C)		At $t=75\text{s}$ (maximum stress appears) $\sigma_1 = 258\text{MPa}$ $\sigma_\theta = 258\text{MPa}$ $\sigma_z = 210\text{MPa}$ $\sigma_r = 11\text{MPa}$ $\tau_{rz} = 116\text{MPa}$	
$u=25\text{mm/s}$	At $t=1.1\text{s}$ (maximum stress appears) $\sigma_1 = 246\text{MPa}$ (A) $\sigma_\theta = 246\text{MPa}$ (A) $\sigma_z = 209\text{MPa}$ (A) $\sigma_r = 89\text{MPa}$ (A) $\tau_{rz} = 98\text{MPa}$ (B)		At $t=1.73\text{s}$ (maximum stress appears) $\sigma_1 = 196\text{MPa}$ $\sigma_\theta = 196\text{MPa}$ $\sigma_z = 186\text{MPa}$ $\sigma_r = 112\text{MPa}$ $\tau_{rz} = 80\text{MPa}$	

temperature difference appears in the thickness direction. Those different conclusions may be explained in terms of deformations of the tube. For vertical tube, the deformation is always axi-symmetric. However, for horizontal tube, dipping slowly causes large asymmetric deformation, which results in the largest $\sigma_{\theta\max}$ at the inner surface of the end of the tube. On the other hand, for dipping fast of horizontal tube, the deformation is almost axi-symmetric.

2.7 Conclusions

In the recent low pressure die casting machine, the vertical tube called stalk is usually made of ceramics because of its high temperature and corrosion resistances. However, attention should be paid to the thermal stresses when the tube is dipped into the molten aluminum. In this study, the finite element method in connection with thermo-fluid analysis (finite volume method) for surface heat transfer coefficient α was applied to reduce the thermal stress when the tube is installed in the crucible. The conclusions are given as following.

1. Thermal stress for 2D ceramic cylinder was considered. It was found that accurate α distribution is desirable for obtaining accurate thermal stress by applying the finite volume method (see Figs. 2.7 (a) and 2.7 (b)).
2. For vertical tube, dipping slowly ($u = 2\text{mm/s}$) may be suitable for reducing the thermal stresses because dipping fast ($u = 25\text{mm/s}$) causes larger temperature difference in the thickness direction, which results in larger thermal stresses.
3. For horizontal tube, however, dipping fast may be suitable for reducing the thermal stress even though it causes larger temperature difference in the thickness direction of the tube.
4. The different conclusions about the vertical and horizontal tubes may be explained in terms of deformations of tube. For horizontal tube, dipping slowly causes larger asymmetric deformation, which results in larger $\sigma_{\theta_{\max}}$ at the tube ends.

References

1. "The A to Z of Materials" Aluminum Casting Techniques-Sand Casting and Die Casting Processes. (Online), available from <<http://www.azom.com/details.asp?Articled=1392>>, (accessed 2008-4-23).
2. Bonollo, F., Urban, J., Bonatto, B., and Botter, M., Gravity and Low Pressure Die Casting of Aluminium Alloys: a Technical and Economical Benchmark, *Alluminio E Leghe*, 2005.
3. Noda, N.A., Yamada, M., Sano, Y., Sugiyama, S., and Kobayashi, S., Thermal Stress for All-ceramics Rolls used in Molten Metal to Produce Stable High Quality Galvanized Steel Sheet, *Engineering Failure Analysis*, Vol. 15, pp. 261-274, 2008.
4. Editorial committee of JSME, *Data of heat transfer*, Tokyo: JSME, p.323, 1986 (in

- Japanese).
5. Nogami, S., Large Sialon Ceramics Product for Structural Use, *Hitachi Metal Report*, Vol.15, pp.115-120, 1999, (in Japanese).
 6. Korenaga, I., Sialon Ceramics Products used in Molten Aluminum, *Sokeizai*; 5:12-7, 1991 (in Japanese).
 7. Huh, J. W., and Kobayashi, H., Effect of Specimen Geometry on Bending Strength of Ceramics/Metal Joints, *Journal of Japan Society of Mechanical Engineering* (Seri A) Vol. 63, No. 609, pp. 983-988, 1975.
 8. Zukauskas, A., Heat Transfer from Tubes in Cross Flow, In: Hartnett JP, Irvine Jr TF, editors, *Advances in Heat Transfer*, Vol.8, New York: Academic Press, p. 131, 1972.
 9. Editorial committee of JSME, *Data of heat transfer*, Tokyo: JSME; p.61, 1986 (in Japanese).
 10. Adachi, T., Tamura, Y., and Yoshioka, T., Techniques of Automatic Operation in Continuous Galvanizing Line, *Kawasaki Steel Technical Report*, Vol.34, pp. 18-25, 1996.
 11. Nishimura, K., Katayama, K., Kimura, T., Yamaguchi, T., and Ito, M., Newly Develop Techniques for Improving the Quality of Continuous Hot dip Plating Strips, *Hitachi Technical Report*, Vol. 65(2), pp. 121-126, 1983 (in Japanese).

Chapter 3

Thermal Stress and Heat Transfer Coefficient for Simple Ceramics Tube and Tube with protuberance Dipping into Molten Aluminum

3.1 Introduction

Ceramics tube called stalk has been used in the low pressure die casting machine⁽¹⁾ (LPDC). In this study the shape of tube as shown in Fig. 3.1 is used. Ceramics tube has high temperature resistance and high corrosion resistance. Previously, the tube was made of cast iron which resulted in spoiling the quality of the product due to the tube partial melted by molten metal. Therefore, ceramics tube was introduced to improve the life time of tube. However, there is still low reliability of ceramics mainly

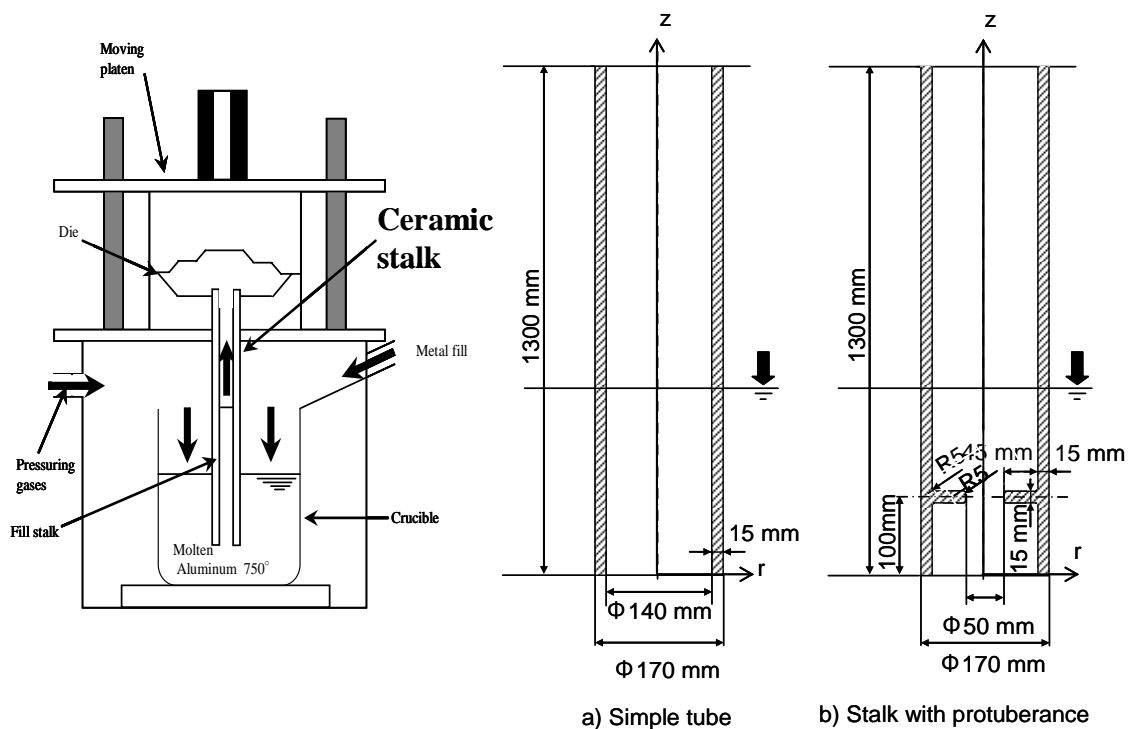


Fig. 3.1 Schema of the low pressure die casting (LPDC) machine
(Note that LPDC is sometimes called “low pressure casting” in Japan)

due to low toughness.

The ceramics tube plays a critical function in the LPDC⁽²⁾ because it receives the molten metal with high temperature from the crucible. However, attention should be paid to the thermal stress when the ceramics tube is dipped into the molten metal. It is important to reduce the risk of fracture because of low fracture toughness of ceramics. In this study the finite volume method is applied to calculate surface heat transfer coefficient. Then, the finite element method is applied to calculate the thermal stresses

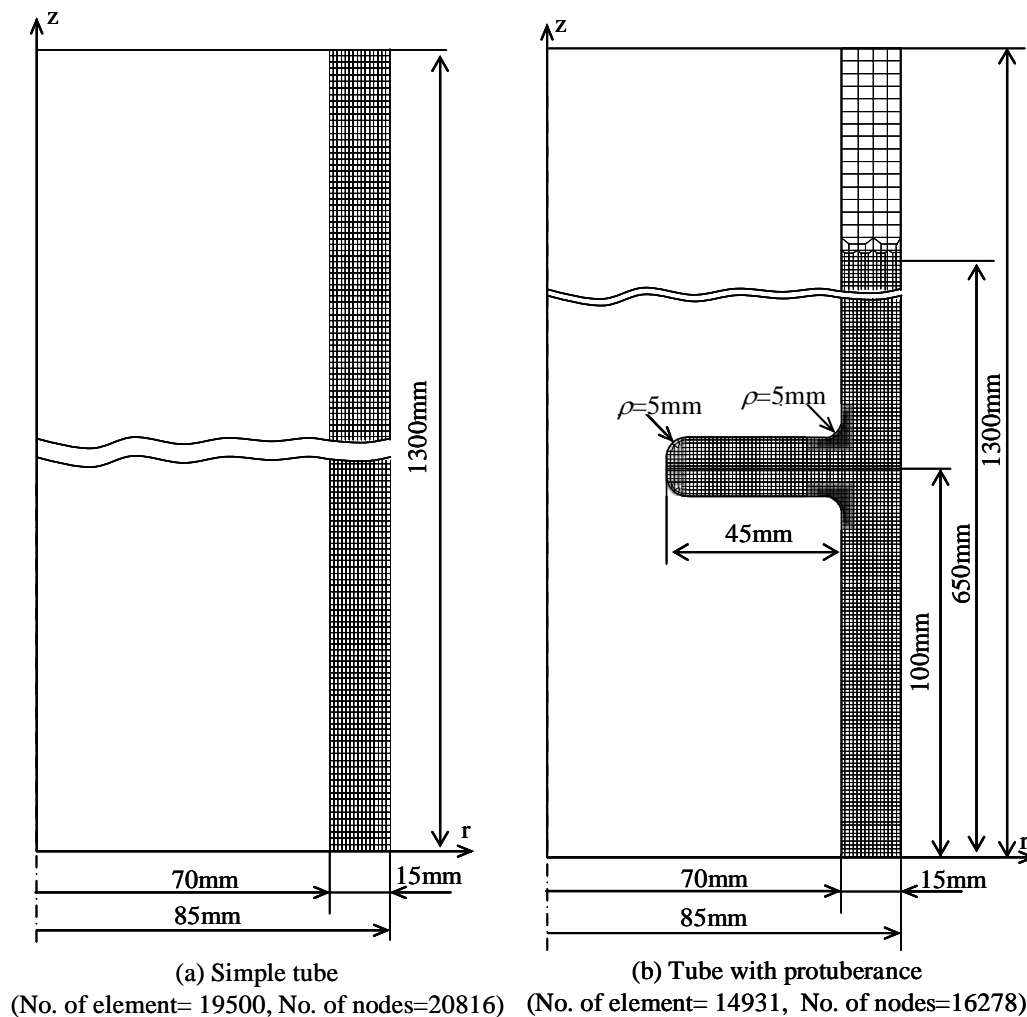


Fig. 3.2 Finite element mesh of ceramics stalk
(Note that the protuberance has the radius $\rho=5\text{mm}$)

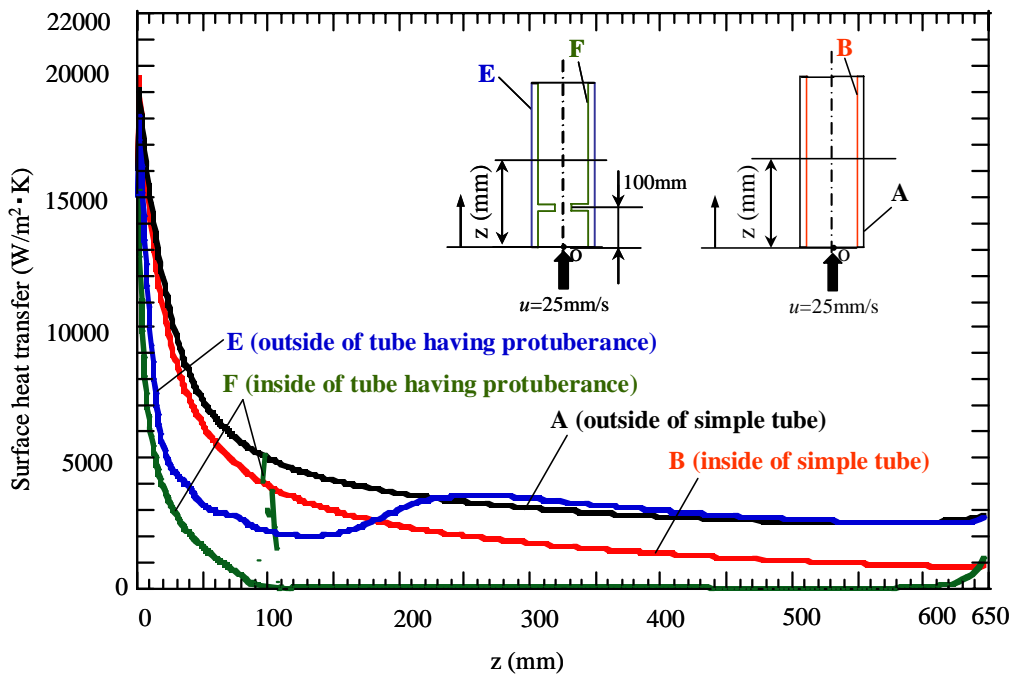


Fig. 3.3 Surface heat transfer coefficient for simple tube and stalk with protuberance models as a function of z in the molten metal with the velocity $u=25\text{mm/s}$

when the tube with protuberance is dipped into the crucible with varying dipping speeds. Figure 3.1 shows the model of ceramics tube for simple model and tube with protuberance.

3.2 Analysis Method

3.2.1 Analysis Model and Material Properties

In low pressure die casting machine, the tube is 170mm in diameter and 1300 mm in length. As shown in Fig. 3.1 (b) the tube has the protuberance with the root radius $\rho = 5\text{mm}$. The tube is made of ceramics because of its high heat temperature resistance and high corrosion resistance. Temperature of the molten aluminum is assumed to be 750°C , and the initial temperature of the ceramics tube is assumed to be 20°C . Table 2.1 (see in Chapter 2) shows the physical properties of molten aluminum at

750°C (1023K)⁽³⁾⁽⁴⁾. Table 2.2 (see in Chapter 2) shows the mechanical properties of ceramics called Sialon⁽³⁾⁽⁴⁾ used for the tube. Axi-symmetric model will be used for simple tube with a total of 19500 elements and 20816 nodes, and for tube with protuberance with a total of 14931 elements and 16278 nodes as shown in Fig. 3.2. In this study, laminar⁽⁵⁾⁽⁶⁾ model is applied for finite volume method and 4-node quadrilateral elements are employed for FEM analysis.

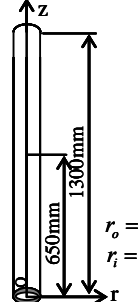
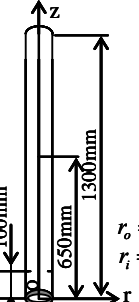
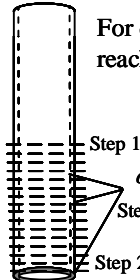
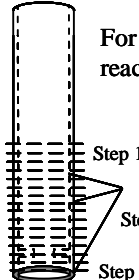
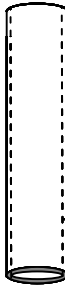
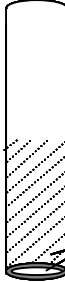


3.2.2 Surface Heat Transfer Coefficient for Ceramics Tube

In this study, axi-symmetric models are analyzed by using the finite volume method to calculate α when the tube is dipped into the molten metal. For axi-symmetry model, the values of the surface heat transfer coefficient α inner (B) and outer (A) of tube are different as shown in Fig. 3.3. Figure 3.3 shows the surface heat transfer coefficient α of tube with protuberance compared with the simple tube. As shown in Fig. 3.3 the values of α for inner (F) of tube with protuberance are much smaller than those of the simple tube (B) and the value of α becomes 350 W/m²K when $z \geq 100\text{mm}$. The molten metal cannot go into the ceramics tube with protuberance smoothly and most of the molten metal has to detour the tube. Therefore, the outer α of ceramics tube with protuberance is also lower than the outer α of the simple tube when $z < 200\text{mm}$. And when $z > 230\text{mm}$, the outer α of ceramics tube with protuberance becomes coincides with the outer α of simple tube. Table 3.1 shows the values of surface heat transfer coefficient α for simple tube and for ceramics tube with protuberance at $u = 2\text{mm/s}$ and $u = 25\text{mm/s}$.

3.3 Thermal Stress for Simple Tube and Tube with Protuberance

The simple tube and tube having protuberance with the length of 1300mm and

Table 3.1 surface heat transfer coefficient α , $W/m^2 \cdot K$

Model	 <p style="text-align: center;">Cylinder model under vertical dipping (Molten Al T=750°C)</p> <p style="text-align: center;">$r_o = 85\text{mm}$ $r_i = 70\text{mm}$</p>	 <p style="text-align: center;">Cylinder having protuberance model under vertical dipping (Molten Al T=750°C)</p> <p style="text-align: center;">$r_o = 85\text{mm}$ $r_i = 70\text{mm}$</p>
<p>$u = 2\text{mm/s}$</p>	<p>For dipping step by step until reaching half tube</p>  <p>Step 16 $\alpha = 1.5 \times 10^3 \text{ W/m}^2 \cdot \text{K}$ given Step 8 Step 2</p>	<p>For dipping step by step until reaching half tube</p>  <p>Step 16 $\alpha = 1.5 \times 10^3 \text{ W/m}^2 \cdot \text{K}$ given Step 8 Step 2</p>
<p>$u = 25\text{mm/s}$</p>	<p>(1) $t = 0 - 60\text{s}$ Along inner and outer surfaces $r_i = 70\text{mm}$ $r_o = 85\text{mm}$ $z : 0 - 650\text{mm}$ $\alpha = (0.831 - 19.51) \times 10^3 \text{ W/m}^2 \cdot \text{K}$ For lower end surface $z = 0\text{mm}$ $\alpha = 16.1 \times 10^3 \text{ W/m}^2 \cdot \text{K}$</p>  <p>$\alpha = (0.831 - 19.51) \times 10^3 \text{ W/m}^2 \cdot \text{K}$ $\alpha = (2.53 - 19.1) \times 10^3 \text{ W/m}^2 \cdot \text{K}$ $\alpha = 16.1 \times 10^3 \text{ W/m}^2 \cdot \text{K}$</p> <p>(2) $t = 60\text{s} - 600\text{s}$ When the tube becomes stable, the heat transfer coefficient (α) for exposed surface until reaching half tube is assumed as $\alpha = 0.831 \times 10^3 \text{ W/m}^2 \cdot \text{K}$</p>  <p>$\alpha = 0.831 \times 10^3 \text{ W/m}^2 \cdot \text{K}$</p>	<p>(1) $t = 0 - 60\text{s}$ Along inner and outer surfaces $r_i = 70\text{mm}$ $r_o = 85\text{mm}$ $z : 0 - 650\text{mm}$ $\alpha = (0.035 - 18.1) \times 10^3 \text{ W/m}^2 \cdot \text{K}$ For lower end surface $z = 0\text{mm}$ $\alpha = 15.1 \times 10^3 \text{ W/m}^2 \cdot \text{K}$</p>  <p>$\alpha = (0.035 - 15.3) \times 10^3 \text{ W/m}^2 \cdot \text{K}$ $\alpha = (2.52 - 18.1) \times 10^3 \text{ W/m}^2 \cdot \text{K}$ $\alpha = 0.25 \times 10^3 \text{ W/m}^2 \cdot \text{K}$ $\alpha = 0.034 \times 10^3 \text{ W/m}^2 \cdot \text{K}$ $\alpha = 0.25 \times 10^3 \text{ W/m}^2 \cdot \text{K}$ $\alpha = 15.1 \times 10^3 \text{ W/m}^2 \cdot \text{K}$ $\alpha = (2.24 - 3.64) \times 10^3 \text{ W/m}^2 \cdot \text{K}$ $\alpha = 1.13 \times 10^3 \text{ W/m}^2 \cdot \text{K}$</p> <p>(2) $t = 60\text{s} - 600\text{s}$ When the tube becomes stable, the heat transfer coefficient (α) for exposed surface until reaching half tube is assumed as $\alpha = 0.034 \times 10^3 \text{ W/m}^2 \cdot \text{K}$</p>  <p>$\alpha = 0.034 \times 10^3 \text{ W/m}^2 \cdot \text{K}$</p>

$\rho = 5\text{mm}$ as shown in Fig. 3.1 is considered when half of the tube is dipping into molten aluminum at the speeds of $u = 2\text{mm/s}$ and $u = 25\text{mm/s}$.

3.3.1 Results for Dipping Slowly

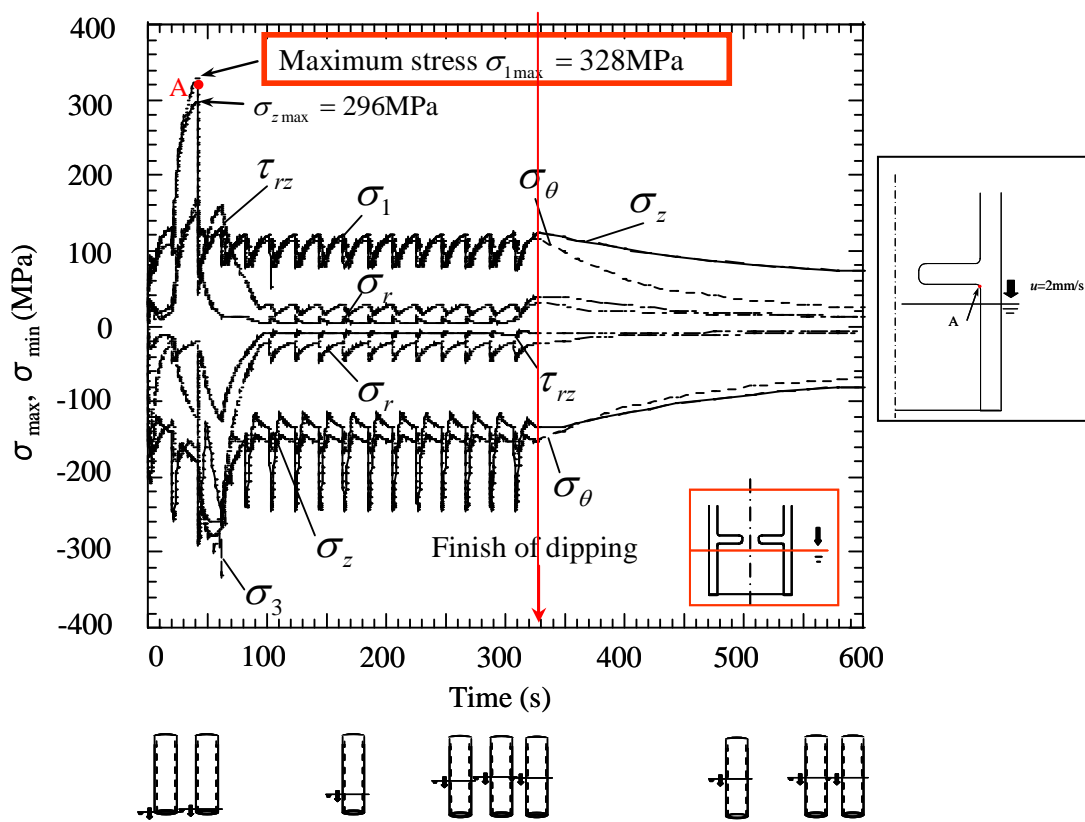


Fig. 3.4 Maximum stresses vs. time relation for stalk with protuberance ($u = 2\text{mm/s}$)

When $u = 2\text{mm/s}$, a constant value $\alpha_m = 1.523 \times 10^3 \text{W/m}^2 \cdot \text{K}$ is applied for dipping step by step along the inner and outer surfaces ($r_i = 70\text{mm}$ and $r_o = 85\text{mm}$) until reaching half tube. Since it takes 328s for dipping completely, sixteen types of partially dipping models are considered as shown in Table 3.1, and the value $\alpha_m = 1.523 \times 10^3 \text{W/m}^2 \cdot \text{K}$ is applied to the whole surface touching molten aluminum. The results are shown in Figs. 3.4-3.5. The figures indicate the maximum tensile principle stress σ_1 , maximum compressive principle stress σ_3 , maximum stresses components σ_r , σ_θ , σ_z and maximum shear stresses τ_{rz} . From Fig. 3.5 it is seen that $\sigma_{z\text{max}}$ coincides with σ_1 at $t = 20.5\text{s}$ for simple tube. Therefore, only $\sigma_{z\text{max}}$ will be discussed because it is almost equivalent to the maximum stresses σ_1 . The stress $\sigma_{z\text{max}}$

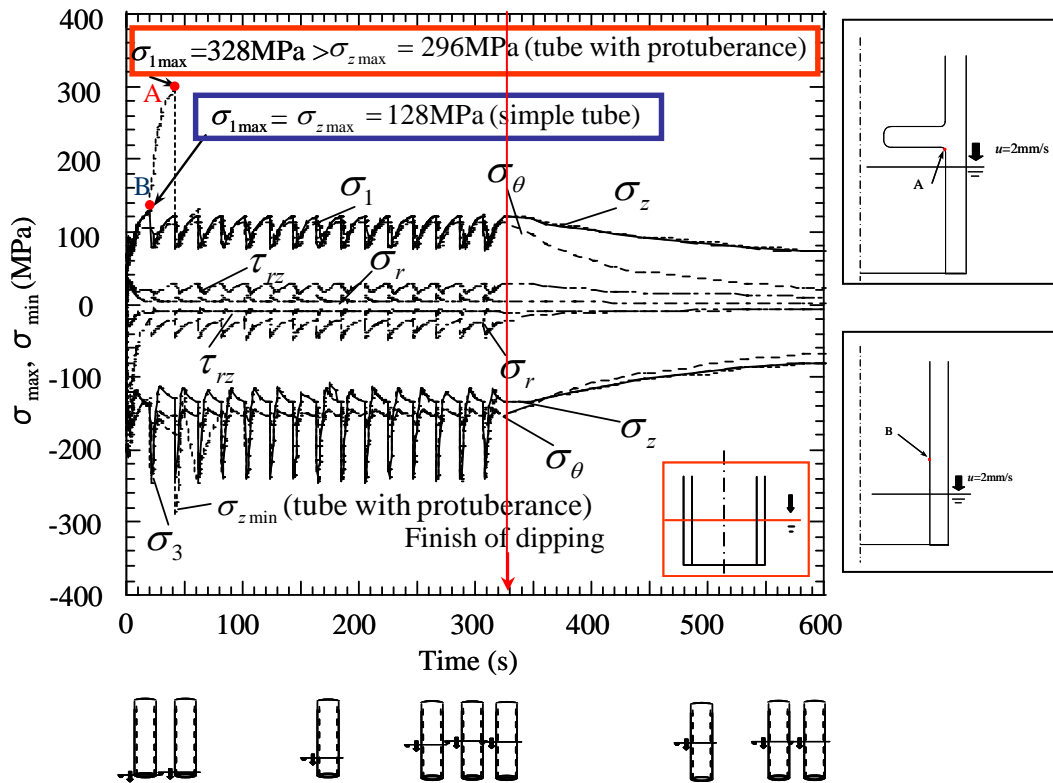


Fig. 3.5 Maximum stresses vs. time relation for simple tube and tube with protuberance ($u = 2\text{mm/s}$): similar to Fig. 2.8 (a)

($=\sigma_{1\max}$) has the peak value of 128MPa at $t = 20.5\text{s}$ for simple tube. For simple tube, the maximum stress $\sigma_{z\max} = 128\text{MPa}$ appears at $t = 20.5\text{s}$ and does not decrease while half of the tube is dipping into molten metal. Then, the stress decreases gradually after half dipping is finished. On the other hand, the maximum stress $\sigma_{1\max}$ ($\cong \sigma_{z\max}$) has the peak value $\sigma_{1\max} = 328\text{MPa}$ ($\sigma_{z\max} = 296\text{MPa}$) at $t = 41\text{s}$ for ceramics tube having protuberance as shown in Fig. 3.4.

However, for tube having protuberance, the maximum stresses $\sigma_{z\max} = 296\text{MPa}$ appears only at $t = 41\text{s}$. After $t = 41\text{s}$ the stress σ_z decreases and coincides with the results for simple tube. Since sixteen types of partially dipping models are utilized, fluctuation of stresses appears as shown in Figs. 3.4 and 3.5.

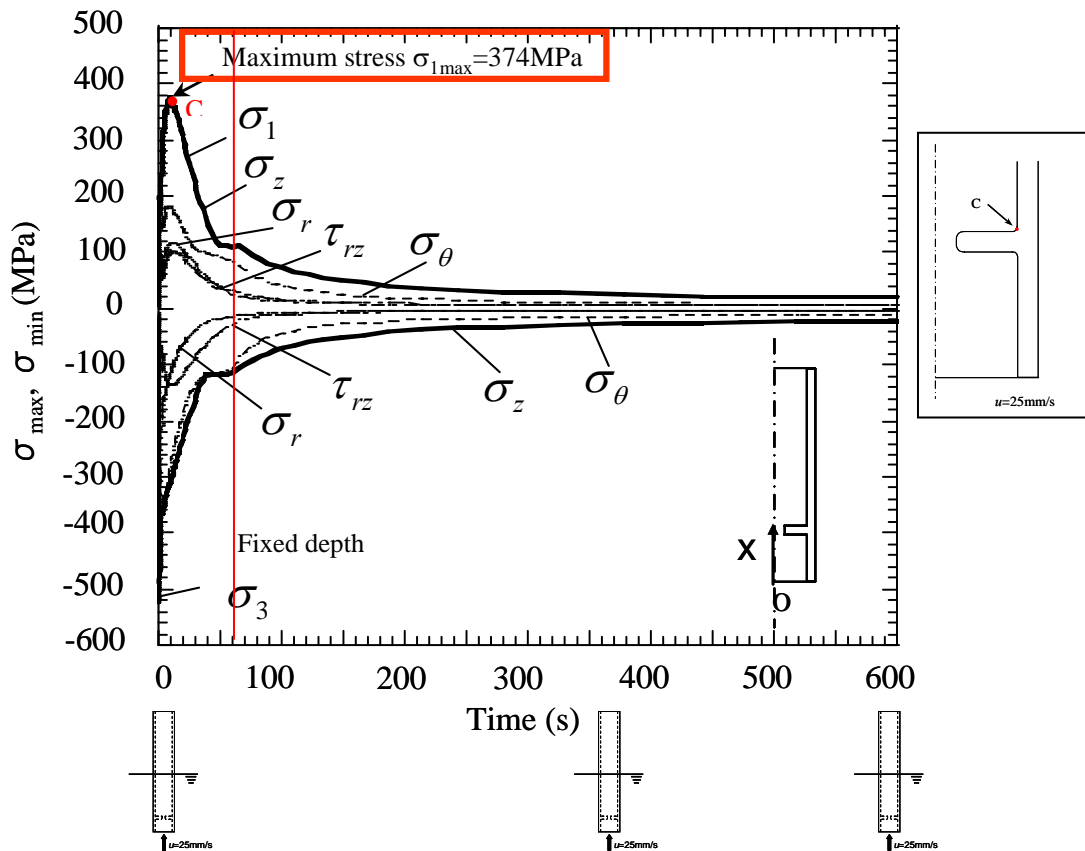


Fig. 3.6 Maximum stresses vs. time relation for stalk with protuberance ($u = 25\text{mm/s}$)

3.3.2 Results for Dipping Fast

Thermal stress is considered when the tube in Fig. 3.1 dips into molten aluminum fast at $u = 25\text{mm/s}$. In this study the finite volume method is used to calculate heat transfer coefficient for thermal stress analysis. In this case the half part of the vertical tube is assumed already in the molten aluminum and molten metal has a velocity of $u = 25\text{mm/s}$. The surface heat transfer is applied as follows (see Table 3.1):

1. When $t = 0 - 60\text{s}$, the values in Table 3.1 $\alpha = (0.831 - 19.516) \times 10^3 \text{W/m}^2 \cdot \text{K}$ is applied at the inner and outer surfaces for simple tube and $\alpha = (0.034 - 18.11) \times 10^3 \text{W/m}^2 \cdot \text{K}$ for tube having protuberance. Also the maximum

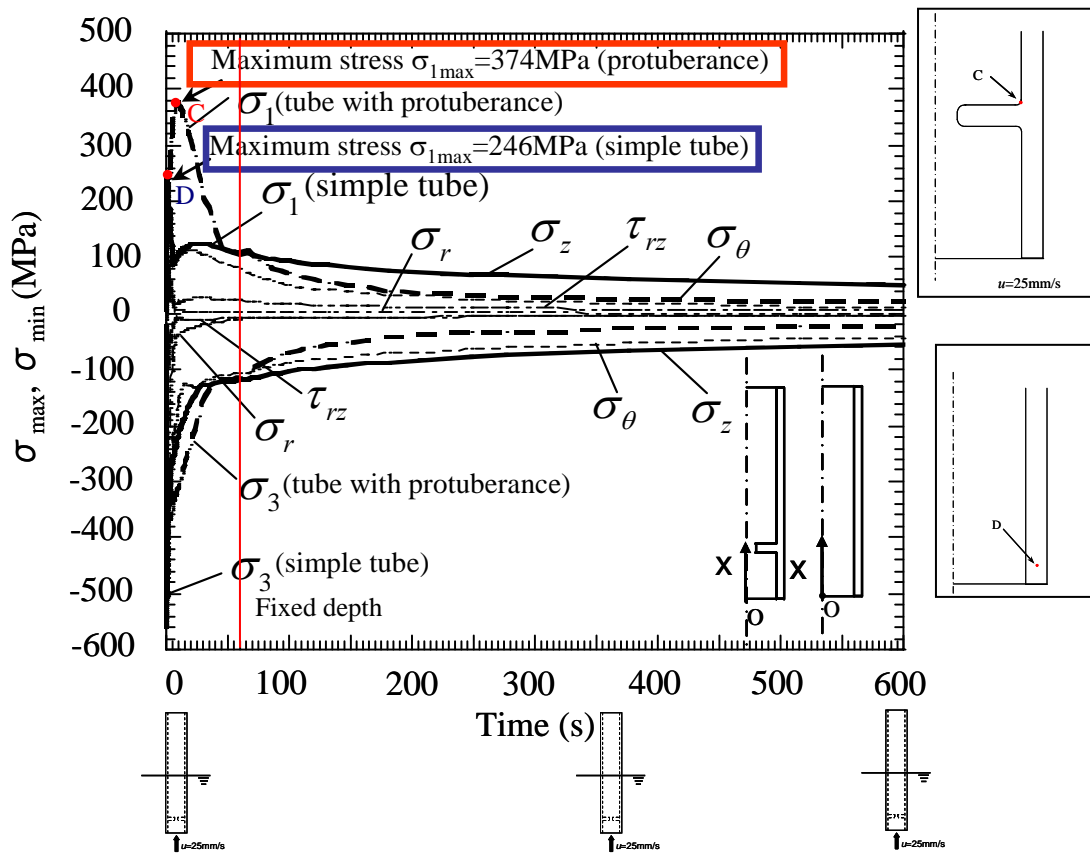


Fig. 3.7 Maximum stresses vs. time relation for simple tube and tube with protuberance ($u = 25\text{mm/s}$)

value, in Fig. 3.3 (b), $\alpha = 16.090 \times 10^3 \text{ W/m}^2 \cdot \text{K}$ is applied at the lower end surface ($z = 0\text{mm}$) for simple tube and $\alpha = 15.09 \times 10^3 \text{ W/m}^2 \cdot \text{K}$ for tube having protuberance.

- When $t > 60\text{s}$, the minimum value, in Fig. 3.3 (b) $\alpha = 0.831 \times 10^3 \text{ W/m}^2 \cdot \text{K}$ is applied for the exposed surface until reaching half tube for simple tube and $\alpha = 0.034 \times 10^3 \text{ W/m}^2 \cdot \text{K}$ for tube having protuberance.

Figures 3.6 and 3.7 show the maximum value of stresses σ_1 , σ_r , σ_θ , σ_z and τ_{rz} . As shown in Fig. 3.7, the maximum tensile stress $\sigma_1 = \sigma_\theta$ increases in a short time. After taking a peak value $\sigma_{\theta\text{max}} = 246\text{MPa}$ at $t = 1.1\text{s}$ for simple tube and

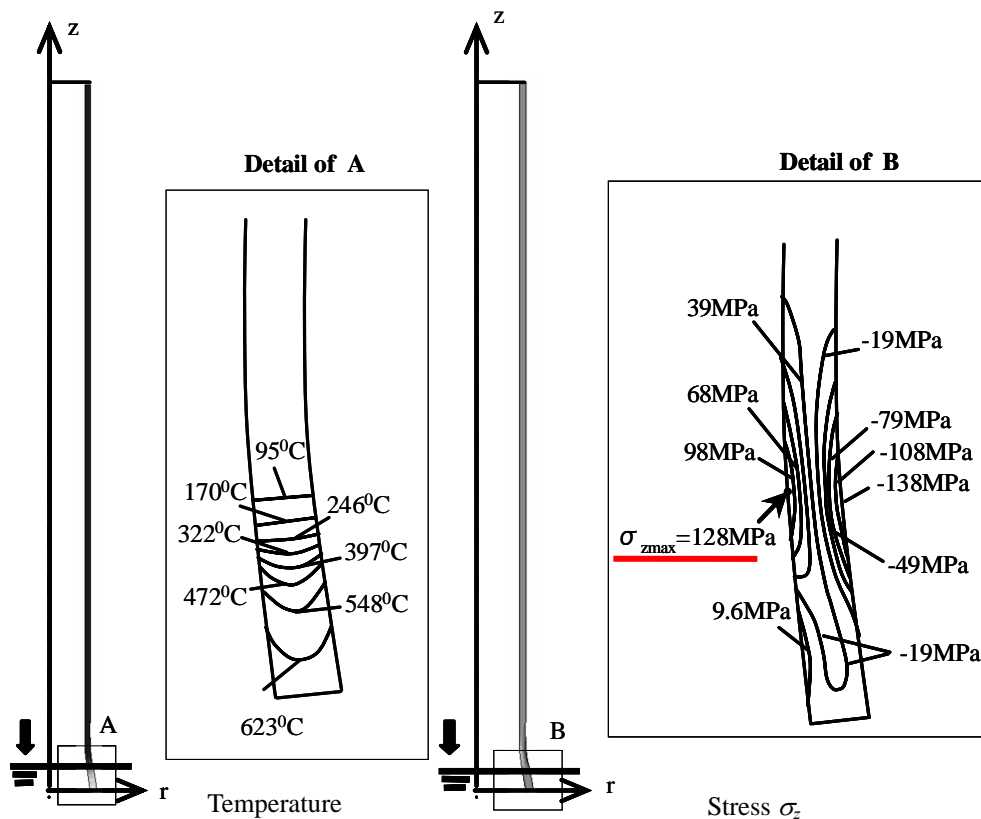


Fig. 3.8 Temperature and stress distribution for simple tube at the time of σ_{\max} ($u = 2\text{mm/s}$, $t = 20.5\text{s}$)

$\sigma_{1\max} = 374\text{MPa}$ ($\sigma_{z\max} = 363\text{MPa}$) at $t = 8.8\text{s}$ for tube having protuberance, it is decreasing. As shown clearly the maximum value of tube having protuberance 374MPa is larger than that of 246MPa for simple tube

3.3.3 Comparison between Dipping Slowly and Fast

The temperature and stress distributions of simple tube and tube having protuberance are indicated in Figs. 3.8-3.11.

(1) Dipping Slowly

Figure 3.8 shows temperature and stress distributions of σ_z at $t = 20.5\text{s}$, where the maximum stress $\sigma_{z\max} = 128\text{MPa}$ appears for the simple tube dipping slowly. For

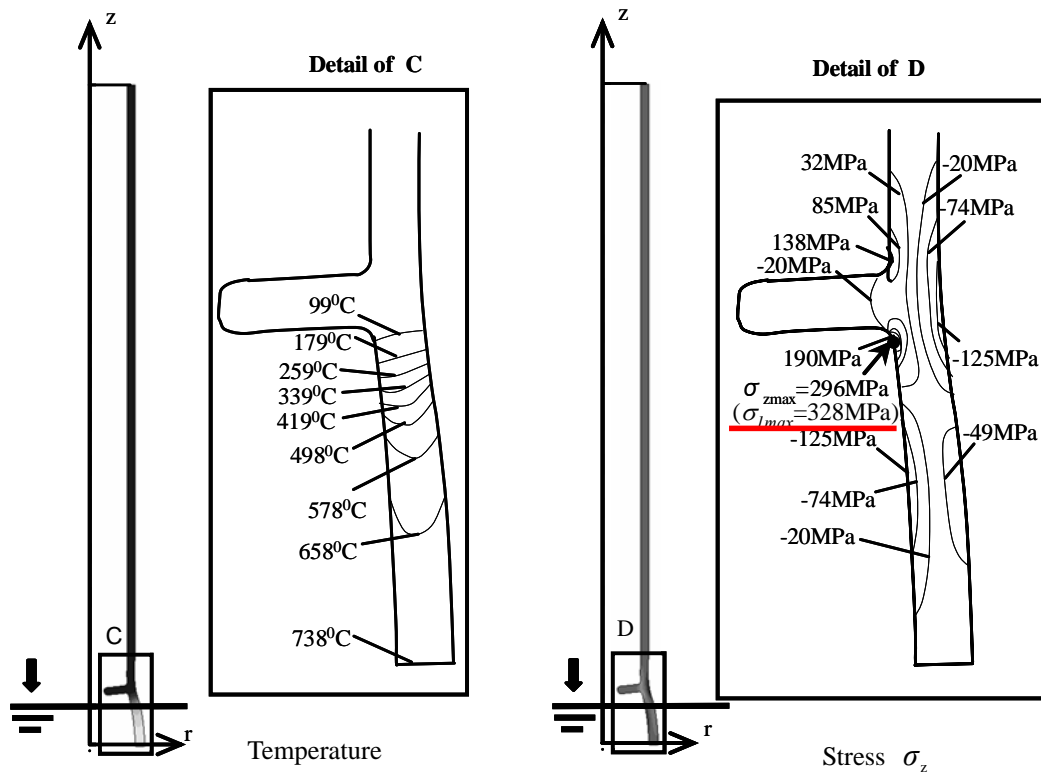


Fig. 3.9 Temperature and stress distribution for stalk with protuberance at the time of σ_{\max} ($u = 2\text{mm/s}$, $t = 41\text{s}$)

simple tube at $u = 2\text{mm/s}$, the maximum stress σ_z appears at the inner surface of the tube $r_i = 70\text{mm}$ just above the dipping level of molten aluminum as shown in Fig. 3.8. This is due to the bending moment caused by the thermal expansion of the dipped portion of the tube. Figure 3.9 shows temperature and stress distributions of σ_z at $t = 41\text{s}$, where the maximum stress $\sigma_{z\max} = 296\text{MPa}$ ($\sigma_{1\max} = 328\text{MPa}$) appears for the tube with protuberance dipping slowly. The maximum stress σ_z appears at the lower root of the protuberance $\rho = 5\text{mm}$ (see Fig. 3.9). This is due to the bending moment caused by the thermal expansion of the dipped portion of the tube and stress concentration by corner radius ρ .

(2) Dipping Fast

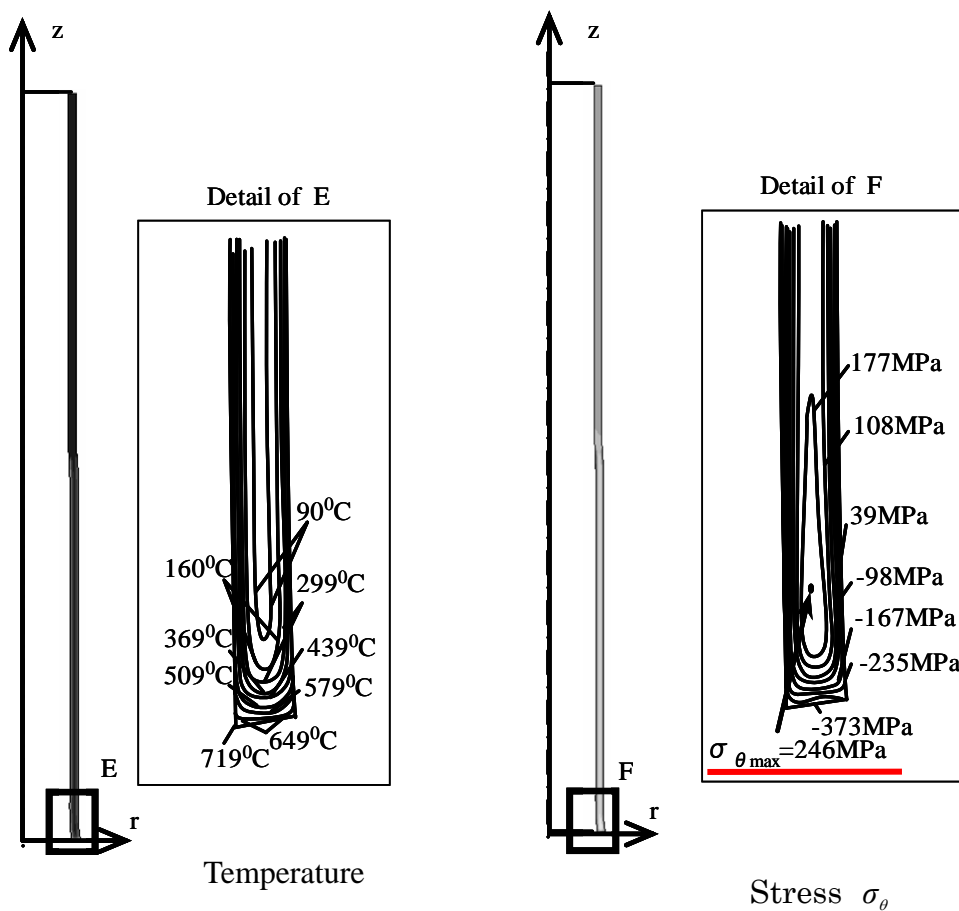


Fig. 3.10 Temperature and stress σ_θ distributions of vertical tube at the time of σ_{\max} ($u = 25\text{mm/s}$ at time $t = 1.1\text{s}$), displacement $\times 50$. : similar to Fig. 2.11

Figures 3.10 and 3.11 show temperature and stress distributions of σ for simple tube and tube with protuberance dipping fast. Figure 3.10 shows temperature and stress distributions σ_θ at $t = 1.1\text{s}$ where the maximum stress $\sigma_{\theta \max} = 246\text{MPa}$ appears for the simple tube dipping fast. For the simple tube at $u = 25\text{mm/s}$, the maximum stress $\sigma_{\theta \max}$ appears on the inside of the thickness as shown in Fig. 3.10. This is due to the large temperature difference appearing in the thickness direction.

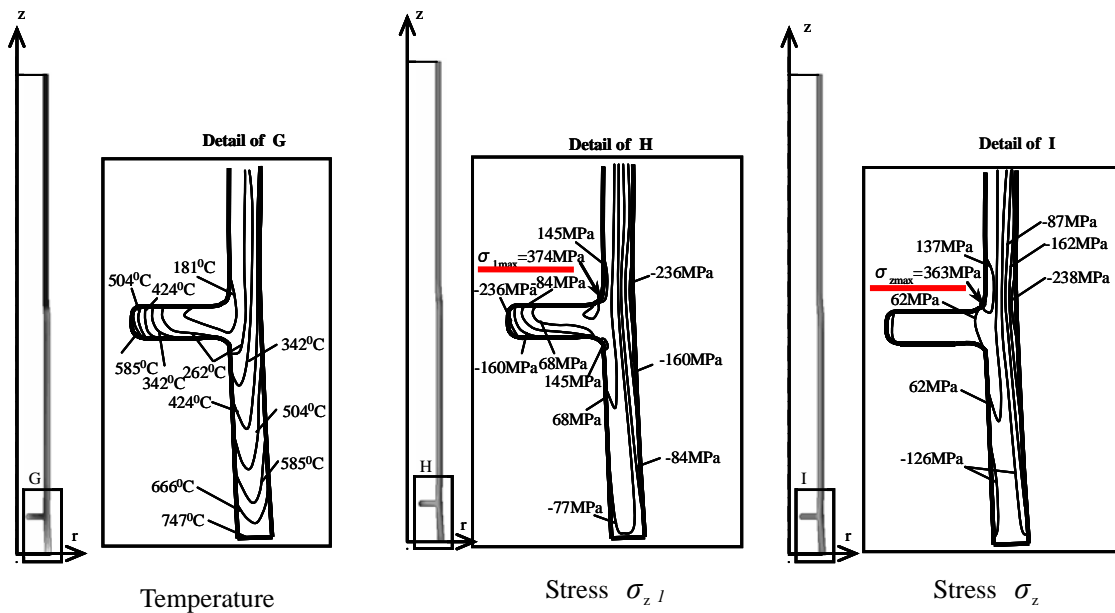
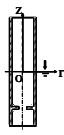
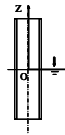
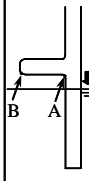
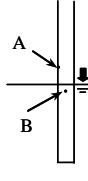
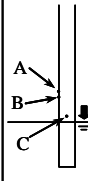
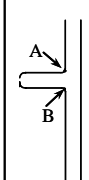
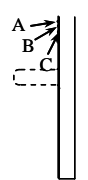



Fig. 3.11 Temperature and stress distributions of vertical tube at the time of σ_{\max} ($u = 25\text{mm/s}$ at time $t = 8.8\text{s}$), displacement $\times 50$

Figure 3.11 shows temperature and stress distributions σ_z at $t = 8.8\text{s}$ where the maximum stress $\sigma_{z\max} = 363\text{MPa}$ ($\sigma_{1\max} = 374\text{MPa}$) appears for tube with protuberance dipping fast. The maximum stress $\sigma_{z\max}$ appears at upper root of protuberance $\rho = 5\text{mm}$ as shown in Fig. 3.11. This is due to the large temperature difference appearing in the outside the thickness and lower part of tube and stress concentration by corner radius ρ .

(3) Comparison between results of simple tube and tube with protuberance

Table 3.2 Maximum stresses for stalk with protuberance compared with the results of simple tube at the same time.

	Tube having protuberance		Simple tube			
Model	Dipping 		Dipping 			
$u=2\text{mm/s}$	At $t=41\text{s}$ (maximum stress appears) $\sigma_1 = 328\text{MPa}$ (A) $\sigma_z = 296\text{MPa}$ (A) $\sigma_\theta = 162\text{MPa}$ (B) $\sigma_r = 167\text{MPa}$ (A) $\tau_{rz} = 150\text{MPa}$ (A)		At $t=41\text{s}$ $\sigma_1 = 120\text{MPa}$ (A) $\sigma_z = 120\text{MPa}$ (A) $\sigma_\theta = 110\text{MPa}$ (A) $\sigma_r = 4\text{MPa}$ (A) $\tau_{rz} = 28\text{MPa}$ (B)		At $t=20.5\text{s}$ (maximum stress appears) $\sigma_1 = 128\text{MPa}$ (A) $\sigma_z = 128\text{MPa}$ (A) $\sigma_\theta = 105\text{MPa}$ (B) $\sigma_r = 4\text{MPa}$ (A) $\tau_{rz} = 21\text{MPa}$ (C)	
$u=25\text{mm/s}$	At $t=8.8\text{s}$ (maximum stress appears) $\sigma_1 = 374\text{MPa}$ (A) $\sigma_z = 363\text{MPa}$ (A) $\sigma_\theta = 181\text{MPa}$ (A) $\sigma_r = 116\text{MPa}$ (A) $\tau_{rz} = 98\text{MPa}$ (B)		At $t=8.8\text{s}$ $\sigma_1 = 101\text{MPa}$ (A) $\sigma_z = 101\text{MPa}$ (A) $\sigma_\theta = 97\text{MPa}$ (A) $\sigma_r = 7\text{MPa}$ (C) $\tau_{rz} = 18\text{MPa}$ (B)		At $t=1.1\text{s}$ (maximum stress appears) $\sigma_1 = 246\text{MPa}$ (A) $\sigma_\theta = 246\text{MPa}$ (A) $\sigma_z = 209\text{MPa}$ (A) $\sigma_r = 89\text{MPa}$ (A) $\tau_{rz} = 98\text{MPa}$ (B)	

For simple tube, the maximum value $\sigma_{\theta\max} = 246\text{MPa}$ for dipping fast is larger than that of $\sigma_{z\max} = 128\text{MPa}$ for dipping slowly. Similarly, for tube with protuberance, the maximum stress $\sigma_{1\max} = 374\text{MPa}$ for dipping fast is larger than that of $\sigma_{1\max} = 328\text{MPa}$ for dipping slowly. Table 3.2 shows maximum stresses for tube with protuberance compared with the results of simple tube at the same time. As shown in Table 3.2, the maximum value of tube with protuberance is about 2.5 times larger than the value of simple tube for $u = 2\text{mm/s}$. On the other hand, for $u = 25\text{mm/s}$ the maximum value of tube with protuberance is about 1.5 times larger than the value of simple tube.

3.4 Conclusions

In the recent low pressure die casting machine, the tube is usually made of ceramics because of its high heat and corrosion resistances. However, attention should be paid to the thermal stresses when the tube is dipped into the molten aluminum. In this study, the finite element method in connection with thermo-fluid analysis (finite volume

method) for surface heat transfer coefficient α was applied to reduce the thermal stress when the tube is installed in the crucible. The conclusions are given as following.

1. Since the molten metal difficult to flow into the tube with protuberance, the inner α of tube with protuberance is much lower than the inner α of simple tube. Accurate α is shown in Table 3.1 and Fig. 3.3.
2. For both simple tube and tube with protuberance, dipping slowly for ceramics tube may be suitable for reducing the thermal stresses because dipping fast causes larger temperature difference in the thickness direction in the case of simple tube, and complex temperature difference in the case of tube with protuberance.

References

1. "The A to Z of Materials" Aluminum Casting Techniques-Sand Casting and Die Casting Processes. (Online), available from <<http://www.azom.com/details.asp?Articled=1392>>, (accessed 2008-4-23).
2. Bonollo, F., Urban, J., Bonatto, B., and Botter, M., Gravity and Low Pressure Die Casting of Aluminium Alloys: a Technical and Economical Benchmark, *Alluminio E Leghe*, 2005.
3. Noda, N.A., Yamada, M., Sano, Y., Sugiyama, S., and Kobayashi, S., Thermal Stress for All-ceramics Rolls used in Molten Metal to Produce Stable High Quality Galvanized Steel Sheet, *Engineering Failure Analysis*, Vol. 15, pp. 261-274, 2008.
4. Noda, N.A., Hendra, Takase, Y., Li, W., Thermal Stress Analysis for Ceramics Tube in the Low Pressure Die Casting Machine, *Journal of Solid Mechanics and Material Engineering*, Vol. 3, No.10, pp. 1090-1100, 2009.
5. Li, H. S, and Mei, C., Thermal Stress in SiC Element used in Heat Exchanger,

- Journal Cent. South Univ. Technol.*, Vol. 12, No.6, pp. 709-713, 2005.
6. Al-Zaharnah, I. T., Yilbas, B. S., and Hashmi, M. S. J., Conjugate Heat Transfer in Fully Developed Laminar Pipe Flow and Thermally Induced Stresses, *Computer Methods in Applied Mechanics and Engineering*, Vol. 190, pp. 1091-1104, 2000.
 7. Editorial committee of JSME, *Data of heat transfer*, Tokyo: JSME, p.323, 1986 (in Japanese).
 8. Korenaga, I., Sialon Ceramics Products used in Molten Aluminum, *Sokeizai*; 5:12-7, 1991 (in Japanese).
 9. Nogami, S., Large Sialon Ceramics Product for Structural Use, *Hitachi Metal Report*, Vol.15, pp.115-120, 1999, (in Japanese).
 10. Editorial committee of JSME, *Data of heat transfer*, Tokyo: JSME; p.61, 1986 (in Japanese).

Chapter 4

Maximum Stress for Shrink Fitting System used for Ceramics Conveying Rollers

4.1 Introduction

Cast iron and steel conveying rollers used in hot rolling mills (see Fig. 4.1) must be changed very frequently because hot conveyed strips induce wear on the roller surface in short period than expectation. The damage portions are usually repaired using the flame spray coating⁽¹⁾. Use of ceramics and cemented carbide has been also promoted in the spray coating⁽²⁾ because they have high temperature resistance and high abrasion resistance.

Figure 4.2 (a) shows the structure of the conventional rollers. For conventional

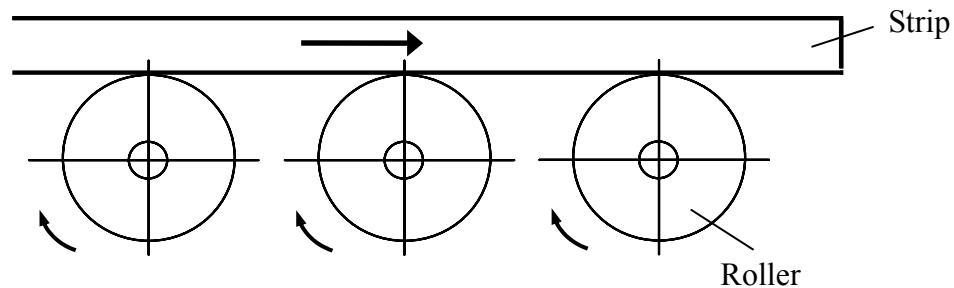


Fig. 4.1 Layout of Conveying Rollers

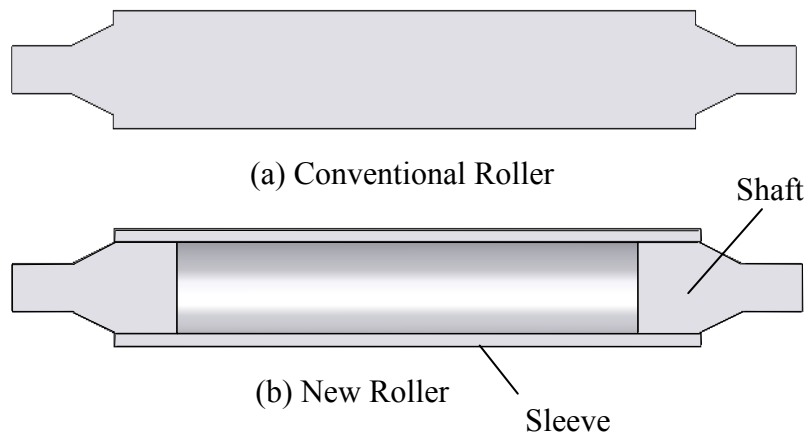


Fig. 4.2 Roller Structure

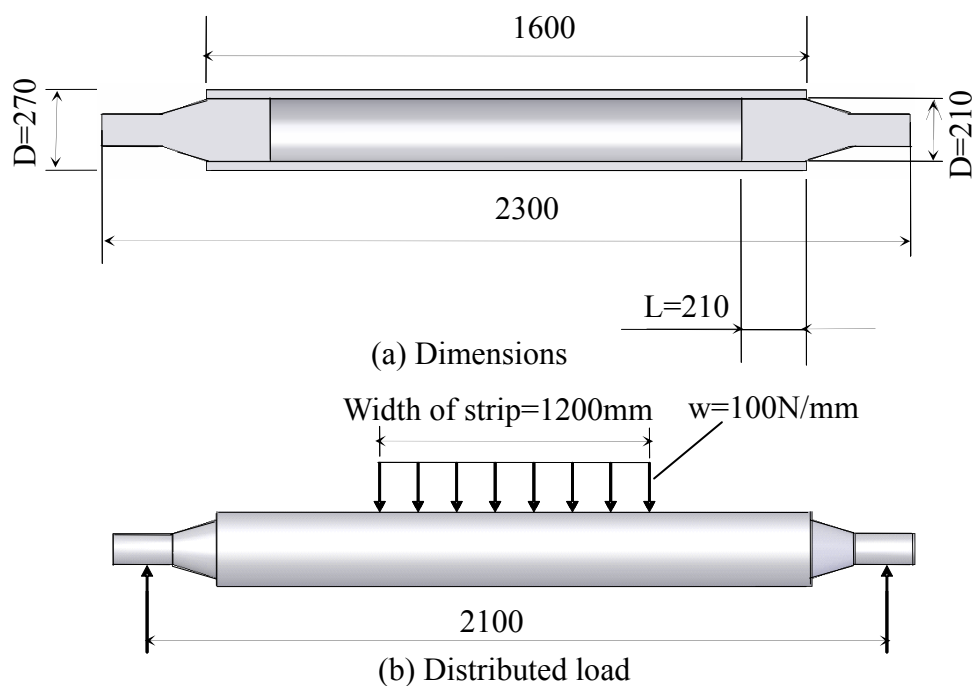


Fig. 4.3 Models considered

rollers, material consumptions are large and the exchange cost is high because we have to change whole roller. In this study, we will focus on the roller structure where a sleeve and two short shafts are connected by shrink fitting at both ends as shown in Fig. 4.2 (b).

The new roller is suitable for maintenance and reducing the cost because we can exchange the sleeve only. In addition, the running speed of the steel strip can be changed smoothly due to the light weight. Moreover, further cost reduction can be realized if ceramics are used as the sleeve because they offer high temperature resistance and high abrasion resistance. However, for the hollow rollers, attention should be paid to the maximum tensile stresses appearing at the edge of the sleeve. In particular, because fracture toughness of ceramics is extremely smaller compared with the values of steel, stress analysis for the roller becomes more and more important.

Therefore, in this study FEM analysis will be applied to the structure as shown in Fig. 4.2 (b), and suitable dimensions will be considered.

4.2 Analytical Conditions

Define the shrink fitting ratio as δ/d , where δ is the diameter difference with the diameter $d = 210\text{mm}$. Assume that the roller is subjected to distributed load $w = 100\text{N/mm}$ and simply supported at both ends (see Fig. 4.3). The friction coefficient between sleeve and shafts is assumed as 0.3.

Table 4.1 shows the material properties of steel, ceramics and also cemented carbide for reference. Stainless steel is usually used for conventional rollers but ceramics and cemented carbide rollers may provide a longer maintenance span due to their high heat resistance and high abrasion resistance.

Figure 4.4 shows the finite element mesh model of the conveying rollers. The total number of elements is 22340 and the total number of nodes is 26751. The model of 1/4 of the roller is considered due to symmetry.

4.3 Results and Discussion

4.3.1 Maximum Tensile Stress

Figure 4.5 shows stress distribution σ_{θ} when the shaft and sleeve are perfectly bonded as a unit body. The maximum tensile stress at point A is 10.1MPa as shown in Fig. 4.5. Figure 4.6 shows stress distribution σ_{θ} at the shrink fitting ratio $\delta/d = 3.0 \times 10^{-4}$. Figure 4.6 (a) shows the stress σ_{θ_s} due to shrink fitting and Fig. 4.6 (b) shows maximum stress distribution $\sigma_{\theta_{\max}} (= \sigma_{\theta_s} + \sigma_{\theta_b})$ due to load distribution

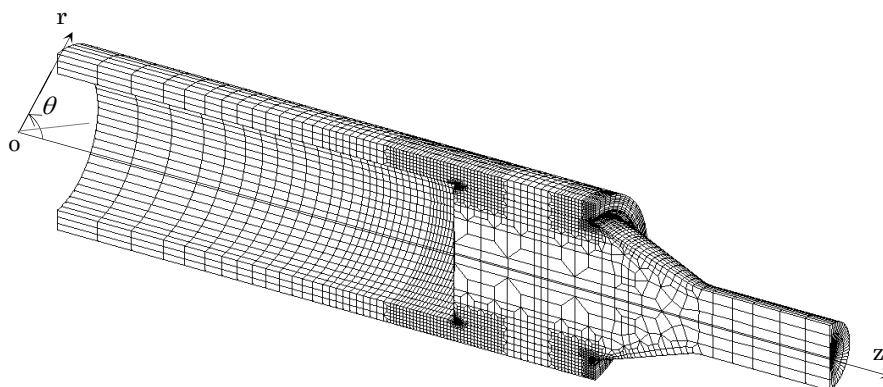


Fig. 4.4 FEM mesh

$w=100\text{N/mm}$ after shrink fitting. As shown in Fig. 4.6, the maximum tensile stress at point A is 75.2MPa while shrink fitting. It becomes 85.6MPa by applying the distribution load after shrink fitting. In other words, $\sigma_{\theta b}$ increases by 10.4MPa .

Figure 4.7 shows stress distribution σ_z at the shrink fitting ratio $\delta/d = 3.0 \times 10^{-4}$. Figure 4.7 (a) shows the stress σ_{zs} due to shrink fitting and Fig. 4.7 (b) shows maximum stress distribution $\sigma_{z\max} (= \sigma_{zs} + \sigma_{zb})$ due to load distribution $w=100\text{N/mm}$ after shrink fitting. As shown in Fig. 4.7, the maximum tensile stress at point B is 34.5MPa while shrink fitting. It becomes 54.5MPa by applying the distribution load after shrink fitting. In other words, σ_{zb} increases by 20.0MPa .

It is found that the maximum tensile stress appears at point A as σ_{θ} . In this study we will focus on reducing the maximum tensile stress σ_{θ} at A with varying

Table 4.1 Material Properties

	Young's modulus [GPa]	Poisson's ratio	Tensile strength [MPa]	Fracture toughness [MPa $\sqrt{\text{m}}$]
Ceramics	300	0.28	500	7.7
Cemented Carbide	500	0.24	1000	20
Steel HV220	210	0.3	600	100



Fig. 4.5 Stress distribution σ_θ when the sleeve and shaft are perfectly bonded as unit body

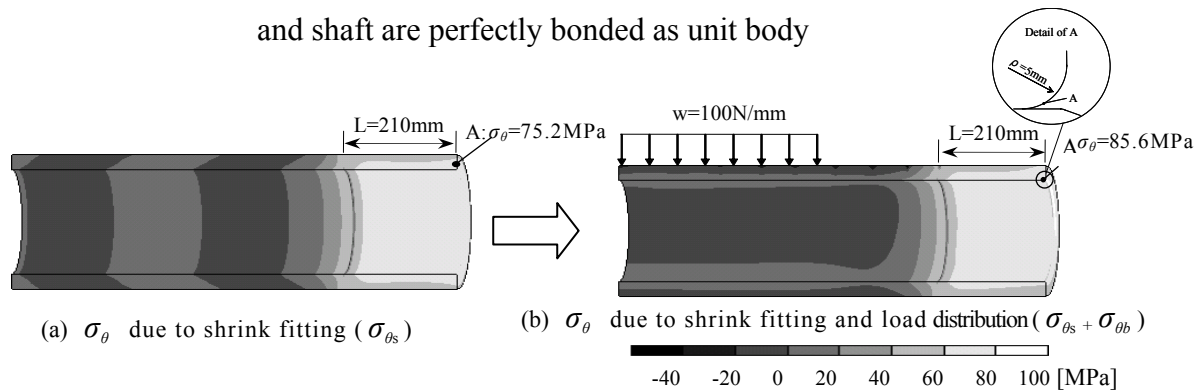


Fig. 4.6 Stress distribution σ_θ when $\delta/d = 3.0 \times 10^{-4}$

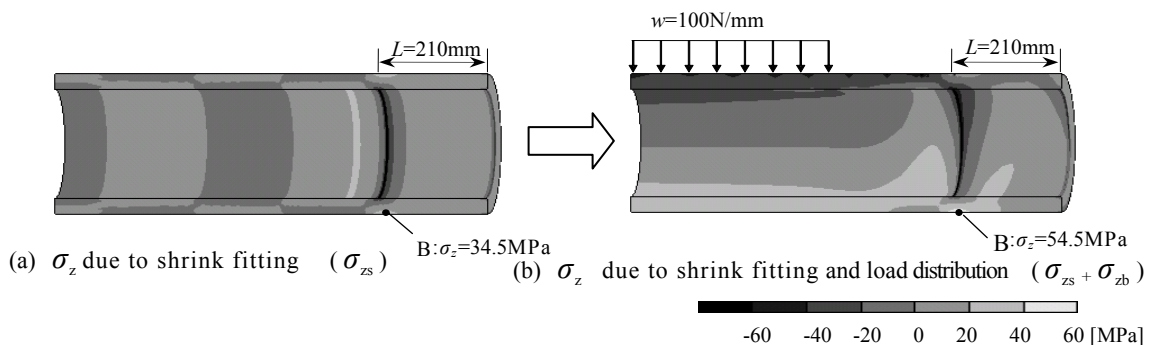


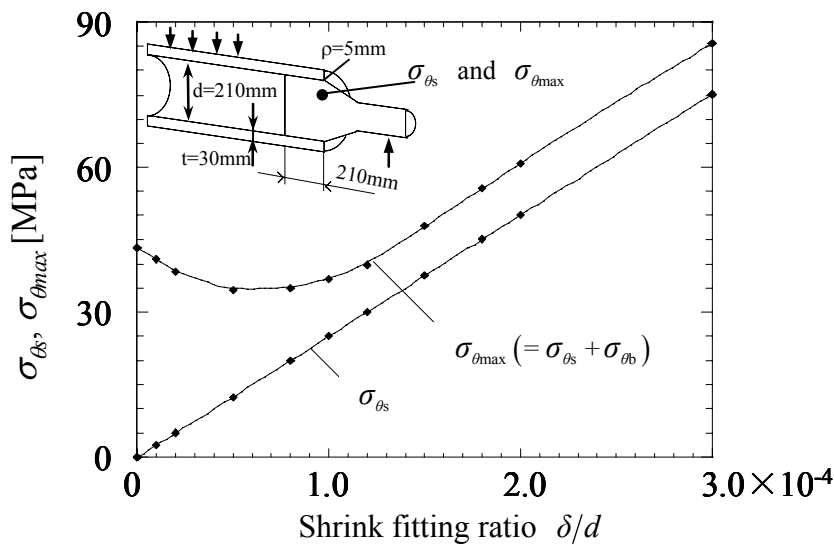
Fig. 4.7 Stress distribution σ_z when $\delta/d = 3.0 \times 10^{-4}$

geometrical conditions.

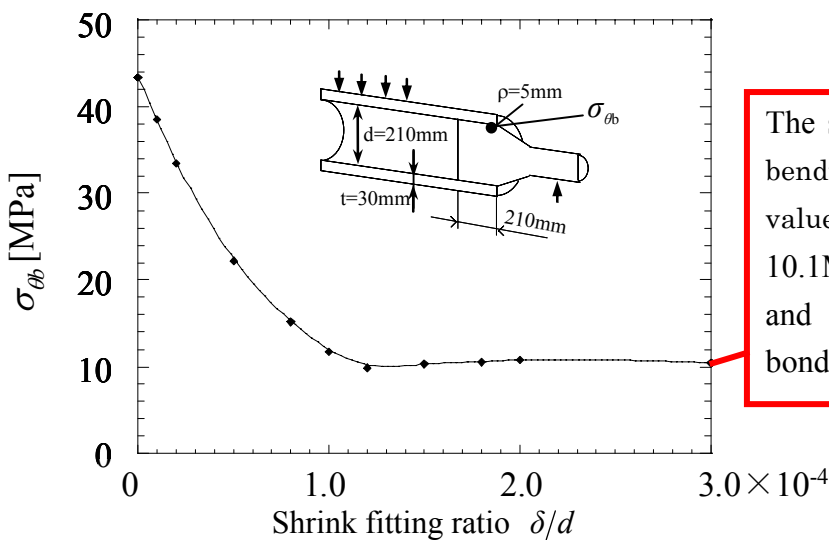
4.3.2 Effect of Shrink Fitting Ratio δ/d and Bending Moment upon the Maximum Tensile Stress $\sigma_{\theta_{max}}$

Figure 4.8 illustrates effects of shrink fitting ratio δ/d upon the stresses σ_{θ_s} , $\sigma_{\theta_{max}}$ and σ_{θ_b} . Figure 4.8 (a) shows the σ_{θ_s} and $\sigma_{\theta_{max}} (= \sigma_{\theta_s} + \sigma_{\theta_b})$ vs. δ/d relationship when the load distribution $w=100\text{N/mm}$ is applied after shrink fitting. To

clarify the effect of load distribution, Fig. 4.8 (b) shows the $\sigma_{\theta b} = \sigma_{\theta max} - \sigma_{\theta s}$ vs. δ/d relationship when the load distribution $w=100N/mm$ is applied. From Fig. 4.8 (a) it is found that $\sigma_{\theta max}$ has a minimum value at about $\delta/d = 0.5 \times 10^{-4}$. When $\delta/d \geq 1.5 \times 10^{-4}$, $\sigma_{\theta s}$ increases linearly with increasing δ/d . On the other hands, $\sigma_{\theta b}$ decreases with



(a) $\sigma_{\theta max}$ vs. δ/d and $\sigma_{\theta s}$ vs. δ/d



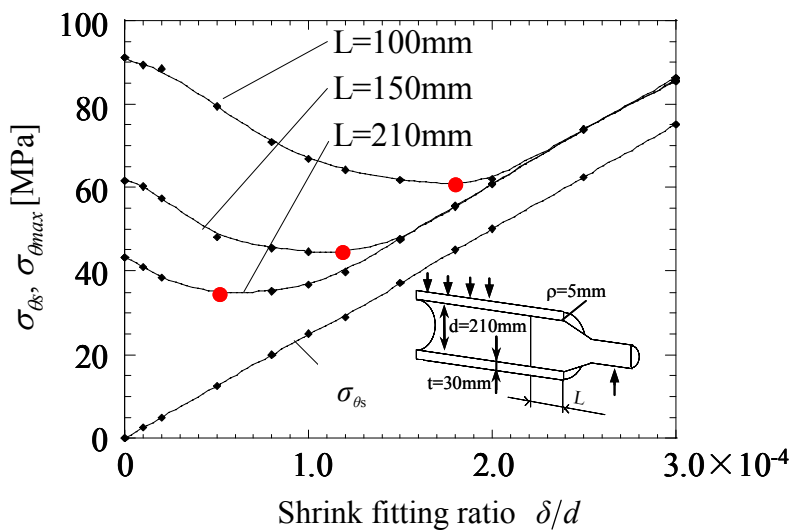
(b) $\sigma_{\theta b}$ vs. δ/d

The stress $\sigma_{\theta b} = 10.4MPa$ by bending coincides with the value maximum stress 10.1MPa when the sleeve and shaft are perfectly bonded as a unit body

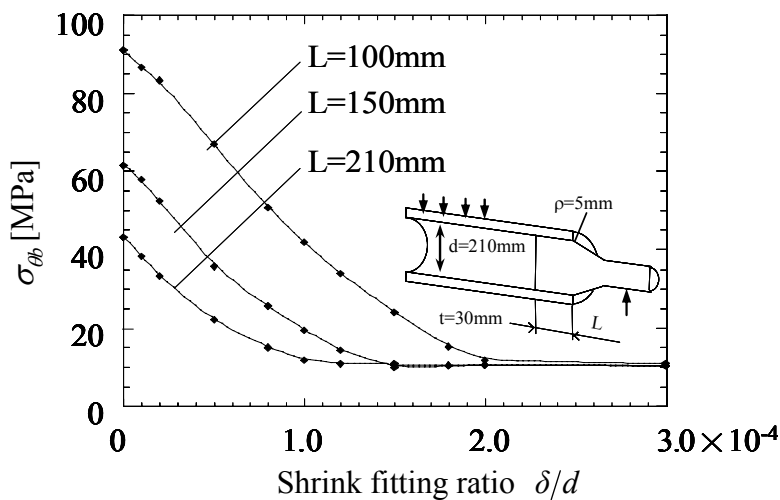
Fig. 4.8 σ_{θ} vs. δ/d when $L=210mm$

($\sigma_{\theta max} (= \sigma_{\theta s} + \sigma_{\theta b})$, $\sigma_{\theta s}$: Stress due to shrink fitting, $\sigma_{\theta b}$: Stress due to load distribution)

increasing δ/d to about $\delta/d=1.0 \times 10^{-4}$, and becomes constant when $\delta/d \geq 1.5 \times 10^{-4}$. Detail investigations reveal that the value $\sigma_{\theta b} = 10.4 \text{ MPa}$ by bending coincides with the value when the shaft and sleeve are perfectly bonded as a unit body as shown in Fig. 4.5. From Fig. 4.8 (b), it is found that the large δ/d reduces the contact stress $\sigma_{\theta b}$ by gripping the shaft tightly. It may be concluded that $\sigma_{\theta \max} (= \sigma_{\theta s} + \sigma_{\theta b})$ has a minimum



(a) $\sigma_{\theta \max}$ vs. δ/d and $\sigma_{\theta s}$ vs. δ/d



(b) $\sigma_{\theta b}$ vs. δ/d

Fig. 4.9 σ_{θ} vs. δ/d when $L=100\text{mm}$, 150mm , 210mm
 ($\sigma_{\theta \max} (= \sigma_{\theta s} + \sigma_{\theta b})$), $\sigma_{\theta s}$: Stress due to shrink fitting, $\sigma_{\theta b}$: Stress due to load distribution)

value at a certain value of δ/d . This is because with increasing δ/d the stress $\sigma_{\theta s}$ increases monotonously but $\sigma_{\theta b}$ decreases and becomes constant.

4.3.3 The Effect of Fitted Length L on $\sigma_{\theta s}$, $\sigma_{\theta \max}$ and $\sigma_{\theta b}$

Figure 4.9 (a) shows $\sigma_{\theta s}$ and $\sigma_{\theta \max} (= \sigma_{\theta s} + \sigma_{\theta b})$ vs. δ/d relation when the load distribution $w=100\text{N/mm}$ is applied after shrink fitting for different fitted length L . Here, we assume the fitted length $L=100\text{mm}$, 150mm , 210mm . Small values of L are desirable for the maintenance because exchanging the sleeve is easier for smaller L . Figure 4.9 (b) shows $\sigma_{\theta b}$ vs. δ/d relation when the load distribution $w=100\text{N/mm}$ is applied. When shrink fitting ratio $\delta/d \geq 2.0 \times 10^{-4}$, $\sigma_{\theta b}$ becomes constant and independent of δ/d . When $\delta/d \geq 2.0 \times 10^{-4}$, the shafts and sleeve can be treated as a unit body bonded perfectly.

From Fig. 4.9 (a), it is found that $\sigma_{\theta \max}$ has a minimum value 60.5MPa at $\delta/d = 1.8 \times 10^{-4}$ when $L=100\text{mm}$. Similarly, it is found that the shrink fitting ratio for minimizing $\sigma_{\theta \max}$ is $\delta/d = 1.2 \times 10^{-4}$ when $L=150\text{mm}$, and also $\delta/d = 0.5 \times 10^{-4}$ when $L=210\text{mm}$. When shrink fitting ratio $\delta/d \geq 2.0 \times 10^{-4}$, $\sigma_{\theta b}$ becomes constant 10.4MPa independent of δ/d .

4.3.4 The Effect of Materials Difference on $\sigma_{\theta s}$, $\sigma_{\theta \max}$ and $\sigma_{\theta b}$

Figure 4.10 shows $\sigma_{\theta s}$, $\sigma_{\theta \max}$ and $\sigma_{\theta b}$ vs. δ/d relation for different materials of sleeve. As shown in Fig. 4.10 (b), the maximum tensile stress of cemented carbide is larger than those of ceramics and steel at the same value of δ/d . This is because the Young's modulus of cemented carbide $E = 500\text{MPa}$ is larger than the ones of ceramics $E = 300\text{MPa}$, and steel $E = 210\text{MPa}$ (see Table 4.1).

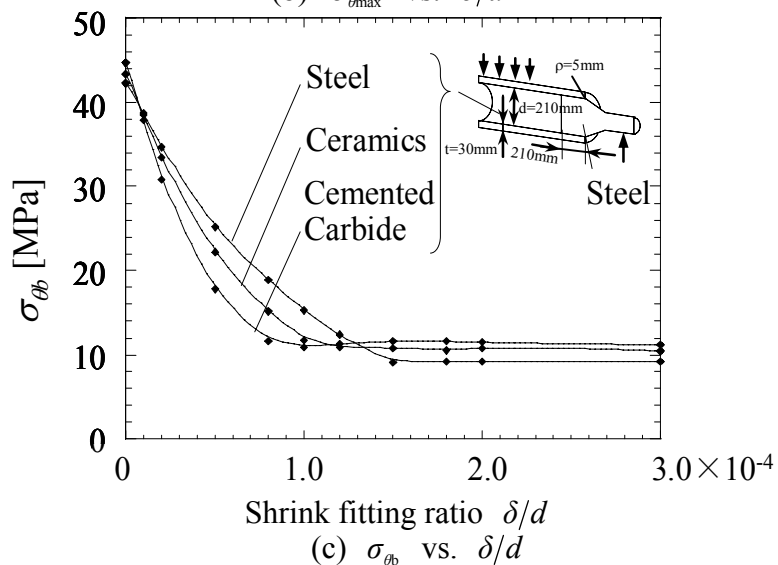
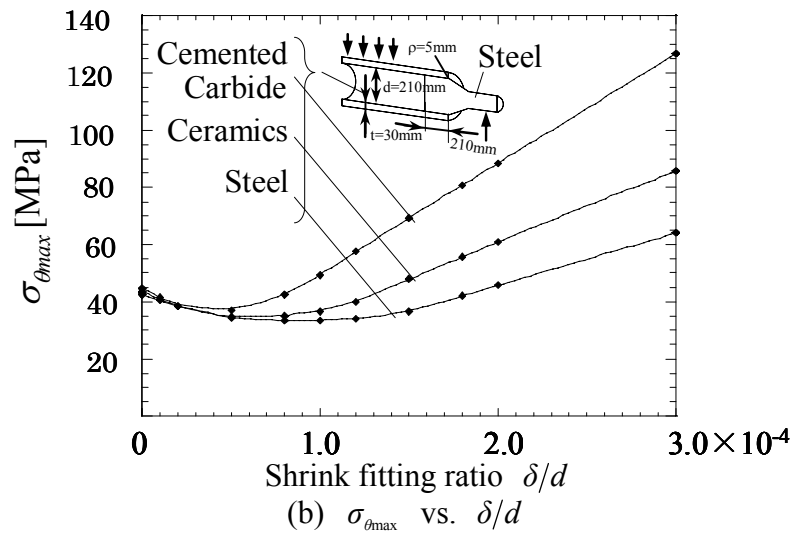
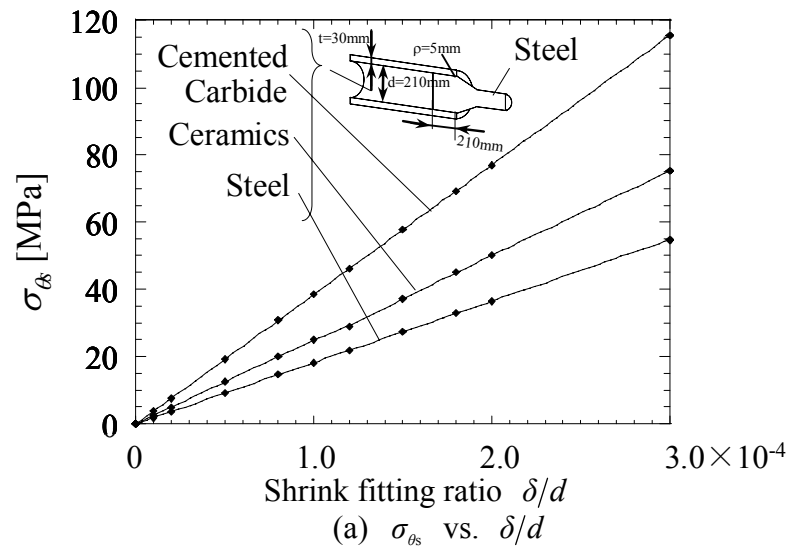


Fig. 4.10 σ_{θ} vs. δ/d when Steel, Ceramics, Cemented Carbide are used as the sleeve ($\sigma_{\theta_{max}} (= \sigma_{\theta_s} + \sigma_{\theta_b})$, σ_{θ_s} : Stress due to shrink fitting, σ_{θ_b} : Stress due to load distribution)

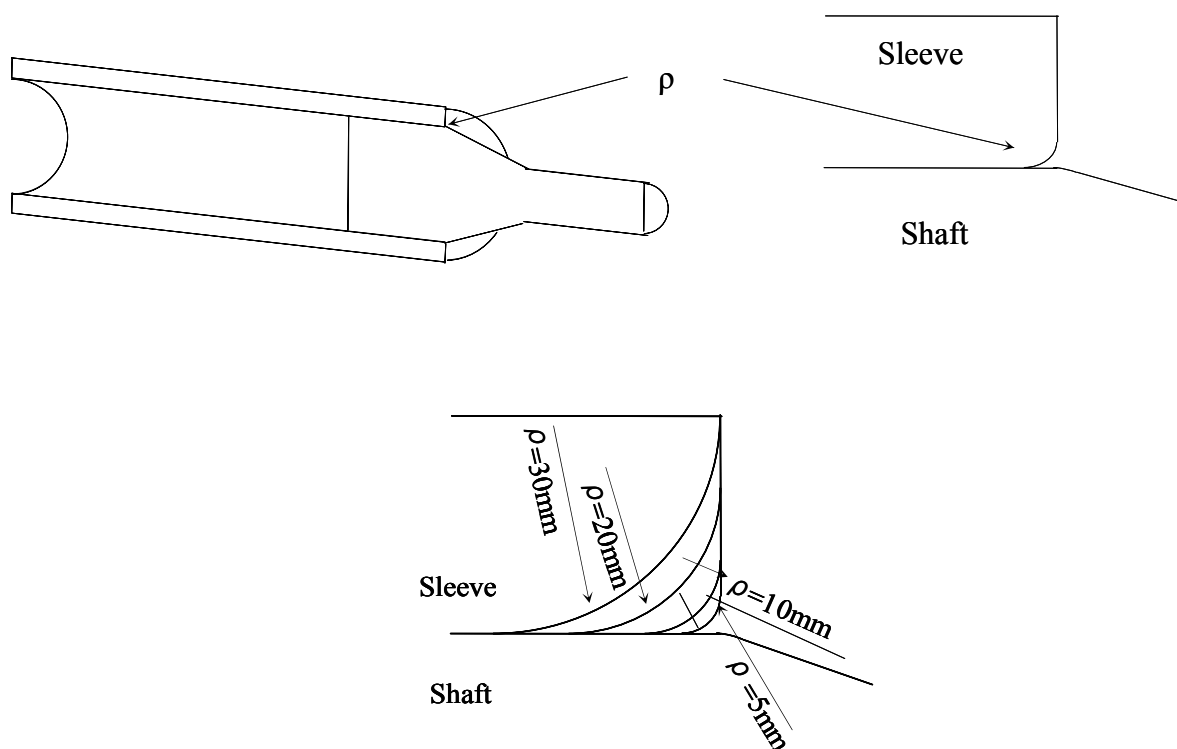


Fig. 4.11 Curvature radius on sleeve end corner of inner side

From Fig. 4.10 (c), $\sigma_{\theta b}$ becomes constant when δ/d is large. The constant values are $\sigma_{\theta b}=9.2\text{MPa}$ for steel, $\sigma_{\theta b}=10.4\text{MPa}$ for ceramics and $\sigma_{\theta b}=11.4\text{MPa}$ for cemented carbide. These results coincide with the case when the shafts and sleeve are perfectly bonded as shown in Fig. 4.5. It is seen that $\sigma_{\theta b}$ becomes constant at a smaller value of δ/d if the Young's modulus becomes larger. This is because larger Young's modulus reduces the maximum contact stress by tightening the shafts stronger. In other words the results of larger Young's modulus are corresponding to larger shrink fitting ratio δ/d .

4.3.5 The Effect Radius Curvature ρ on $\sigma_{\theta s}$, $\sigma_{\theta \max}$ and $\sigma_{\theta b}$

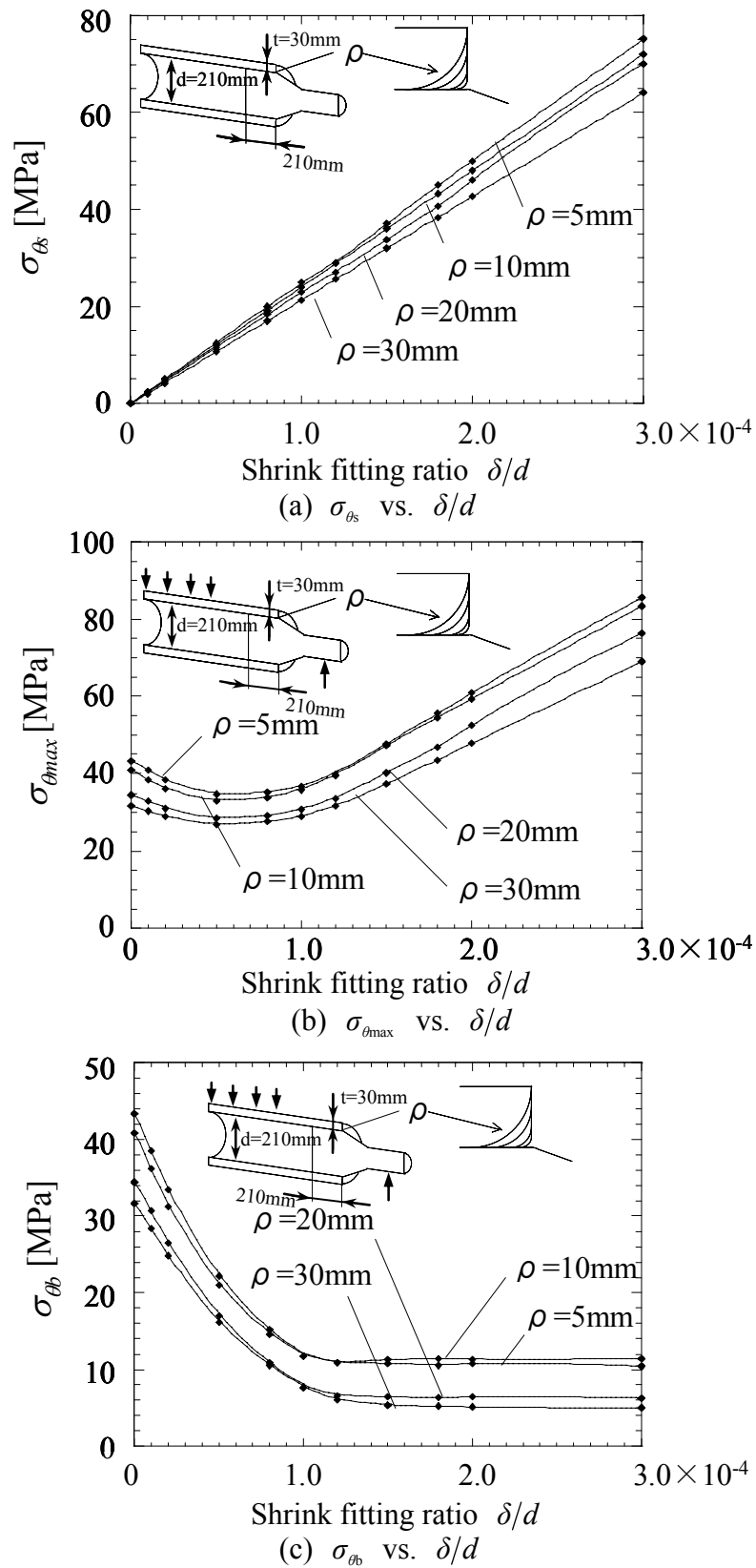


Fig. 4.12 σ_{θ} vs. δ/d when $\rho=5, 10, 20, 30\text{mm}$
 ($\sigma_{\theta_{max}} (= \sigma_{\theta_s} + \sigma_{\theta_b})$, σ_{θ_s} : Stress due to shrink fitting, σ_{θ_b} : Stress due to load distribution)

In the previous discussion, the radius curvature ρ at the edge of sleeve is

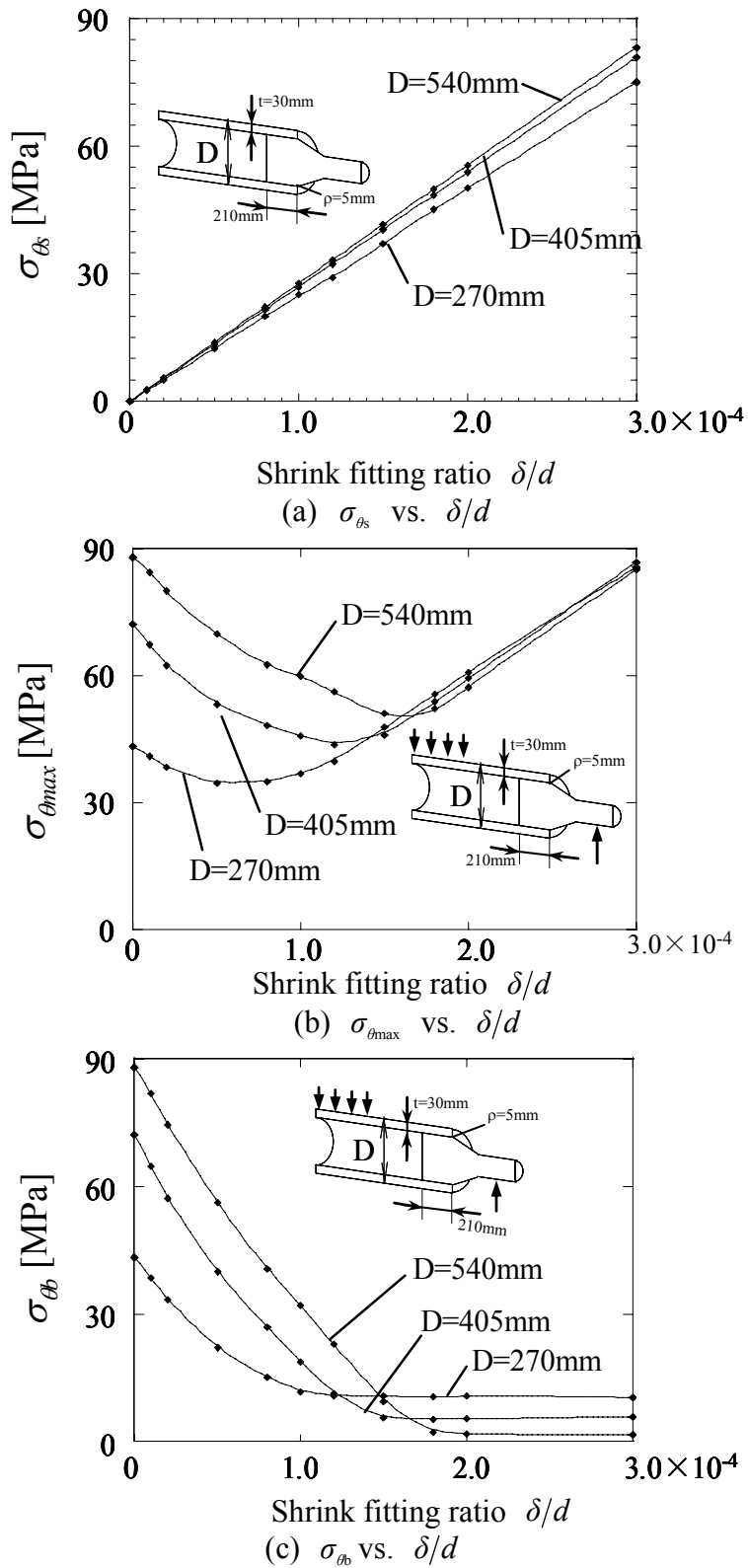


Fig. 4.13 σ_{θ} vs. δ/d when $D=270, 405, 540\text{mm}$

($\sigma_{\theta_{\max}} (= \sigma_{\theta_s} + \sigma_{\theta_b})$, σ_{θ_s} : Stress due to shrink fitting, σ_{θ_b} : Stress due to load distribution)

always assumed as $\rho=5\text{mm}$. However, the values of σ_{θ_s} , $\sigma_{\theta_{\max}}$ and σ_{θ_b} may be

changed depending on the radius curvature ρ because $\sigma_{\theta_{\max}}$ appears at point A in the circular arc part at the edge of sleeve. As shown in Fig. 4.11, therefore, the effect of radius curvature is analyzed with varying $\rho = 5\text{mm}$, 10mm , 20mm , and 30mm . The relationships between the shrink fitting ratio δ/d and σ_{θ_s} , $\sigma_{\theta_{\max}}$ and σ_{θ_b} are shown in Fig. 4.12. From Fig. 4.12 (a) and Fig. 4.12 (b) it is found that the maximum stresses σ_{θ_s} and $\sigma_{\theta_{\max}}$ increase with decreasing the radius ρ . For the large values of δ/d , the stress σ_{θ_b} becomes constant at the same value of δ/d independently of ρ . At the fixed value of $\delta/d = 3.0 \times 10^{-4}$, for example $\sigma_{\theta_{\max}} = 85.6\text{MPa}$ when $\rho = 5\text{mm}$ but $\sigma_{\theta_{\max}} = 69.1\text{MPa}$ when $\rho = 30\text{mm}$. From Fig. 4.12(c), it is seen that σ_{θ_b} becomes larger when δ/d is smaller. However, when $\delta/d \geq 1.5 \times 10^{-4}$ σ_{θ_b} for $\rho = 10\text{mm}$ is larger than σ_{θ_b} for $\rho = 5\text{mm}$.

4.3.6 The Effect of Diameter D on σ_{θ_s} , $\sigma_{\theta_{\max}}$ and σ_{θ_b}

Figure 4.13 shows the relationships between shrink fitting ratio δ/d on σ_{θ_s} , $\sigma_{\theta_{\max}}$ and σ_{θ_b} with varying the outside diameter of sleeve as $D = 270\text{mm}$, 405mm and 540mm . Here, we assume a ceramics sleeve has a fitted length $L = 210\text{mm}$, radius of curvature $\rho = 5\text{mm}$, and thickness of the sleeve $(D-d)/2 = 30\text{mm}$. Also, we calculate magnitudes of load distribution w so as to produce the same value of nominal bending stress σ_{zn} from Eq. (4.1). Then, we have $w = 100\text{N/mm}$ for $D = 270\text{mm}$, $w = 243\text{N/mm}$ for $D = 405\text{mm}$, $w = 450\text{N/mm}$ for $D = 540\text{mm}$. The nominal bending stress is expressed by

$$\sigma_{zn} = \frac{32M}{\pi(D^3 - d^3)} \quad (4.1)$$

where

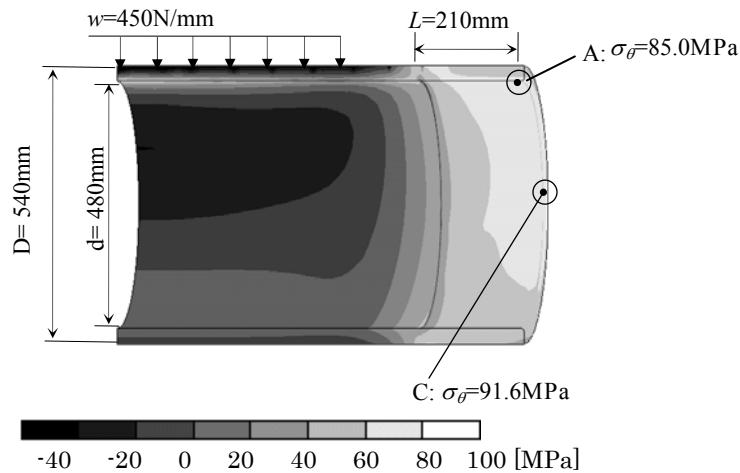


Fig. 4.14 σ_{θ} due to shrink fitting and load distribution when $\delta/d = 3.0 \times 10^{-4}$

D : outside diameter of sleeve (mm)

d : inner diameter of sleeve (mm)

M : bending moment (Nmm)

Figure 4.13 (b) shows that $\sigma_{\theta_{\max}}$ increases with increasing the outer diameter of the sleeve when δ/d is small. With increasing the diameter D , a minimum value of $\sigma_{\theta_{\max}}$ is appearing at a larger value of δ/d . Figure 4.13 (b) is closely related to Fig. 4.9 (a), where the fitted length L is changed under a constant D . In other words, increasing D under a fixed L in Fig. 4.13 (b) is found to be almost equivalent to decreasing L under a fixed D in Fig. 4.9 (a).

From Fig.4.13 (c), it is seen that for large values of δ/d , σ_{θ_b} becomes constant independently of δ/d . The constant values are $\sigma_{\theta_b} = 10.5\text{MPa}$ for $D = 270\text{mm}$, $\sigma_{\theta_b} = 5.5\text{MPa}$ for $D = 405\text{mm}$, and $\sigma_{\theta_b} = 1.9\text{MPa}$ for $D = 540\text{mm}$. Further investigations reveal that those constant values coincide with the values when the shaft and sleeve are perfectly bonded as a unit body. With increasing the outer diameter D , σ_{θ_b} becomes constant under larger values of δ/d .

Figure 4.14 shows a stress distribution σ_{θ} due to the load distribution

$w=450\text{N/mm}$ after shrink fitting when $D=540\text{mm}$ with $\delta/d=3.0\times 10^{-4}$. Attention should be paid to the large diameter D because the maximum stress 91.6MPa appears at point C instead of A ($\sigma_{\theta}=85.0\text{MPa}$) in Fig. 4.6 differently from other cases when $\delta/d \geq 1.0\times 10^{-4}$.

4.4 Conclusions

Hot conveyed strips induce wear on the steel roller surface in short periods than expectation. To reduce maintenance cost for exchanging the rollers, in this study, a new structure is considered where a ceramics sleeve connected with short steel shafts at both ends. Stress analysis was performed with the application of the finite element method; then several geometrical conditions were investigated, such as fitted length L , radius curvature ρ at end of the sleeve, outer diameter D of the sleeve. The conclusions can be made in the following way.

1. The maximum tensile is appearing at the end of the sleeve as $\sigma_{\theta_{\max}}$. The stress $\sigma_{\theta_{\max}}$ may be expressed by $\sigma_{\theta_{\max}} = \sigma_{\theta_s} + \sigma_{\theta_b}$ where σ_{θ_s} is a shrink fitting stress and σ_{θ_b} is a stress due to load distribution. For example, the maximum value $\sigma_{\theta_{\max}} = 85.6\text{MPa}$ appears under the load $w=100\text{N/mm}$ after shrink fitting. Here, $\sigma_{\theta_s} = 75.2\text{MPa}$, $\sigma_{\theta_b} = \sigma_{\theta_{\max}} - \sigma_{\theta_s} = 10.4\text{MPa}$ when the fitted length $L=210\text{mm}$, shrink fitting ratio $\delta/d = 3.0\times 10^{-4}$, radius curvature $\rho = 5\text{mm}$, and outer diameter $D=270\text{mm}$ (see Fig. 4.6).
2. For small values of δ/d , the maximum stress $\sigma_{\theta_{\max}}$ becomes larger because large contact forces may appear between the sleeve and shafts, especially for small L . Suitably larger values of δ/d may reduce $\sigma_{\theta_{\max}}$ effectively. In other words, $\sigma_{\theta_{\max}}$ takes a minimum value at a certain value of δ/d .
3. For large values of δ/d , σ_{θ_b} becomes constant independently from δ/d .

The constant value coincides with the results when the shafts and sleeve are perfectly bonded. In other words, if δ/d is large enough, the shafts and sleeve can be treated as a unit body.

4. The effect of material difference of the sleeve was considered. Under small values of δ/d , a larger Young's modulus of the sleeve may reduce σ_{θ} because the sleeve clamps the shafts more tightly and reduces the magnitude of contact forces. On the other hand, large values of δ/d with larger Young's modulus of sleeve may increase the value of σ_{θ} .
5. With increasing the radius ρ at the end of sleeve, the maximum stress $\sigma_{\theta\max}$ decreases. The stress σ_{θ} becomes constant for large values of δ/d independent of ρ .
6. Care should be taken for large diameters D because the maximum stress σ_{θ} may appear at a different position. Increasing diameter D under a fixed fitted length L is almost equivalent to decreasing L under a fixed D .

References

1. Miki, E., High Corrosion Resistance and Cost Reduction by Spraying Methods, *Plant Engineer*, Vol.21, No.1 1989 (in Japanese).
2. Iwata, T. and Mori, H., Material Choice for Hot Run Table Roller, *Plant Engineer*, Vol.15, No.6 1983 (in Japanese).
3. Harada, S., Noda, N., Uehara, O. and Nagano, M., Tensile Strength of Hot Isostatic Pressed Silicon Nitride and Effect of Specimen Dimension, *Transactions of the Japan Society of Mechanical Engineering*, Vol.57, No.539 1991.
4. Kobayashi, H., and Kawakubo, T., Fatigue –Difference between ceramics and metal, *Journal of the Japan Institute of Metals*, Vol.27, No.10 1988.

Chapter 5

Strength Analysis for Shrink Fitting System Used for Ceramics Rolls in the Continuous Pickling Line

5.1 Introduction

Pickling is the process of chemically removing oxides and scale from the surface of a metal by the action of water solutions of inorganic acids. Considerable variation in type of pickling solution, operation and equipment is found in the industry. Among the types of pickling equipment may be mentioned the batch picklers, modified batch, non-or semi-continuous and continuous picklers⁽¹⁾. Figure 5.1 shows the schematic diagram of pickling line. As shown in Fig. 5.1 the continuous acid wash makes the coil surface clean by going through hydrochloric acid tank and removing surface scale formed in the previous process. Similar lines for Fig. 5.1 may be found in coil painting equipment, which continuously paints the cold rolling lamina coil, galvanizing steel board coil, and aluminum coil, etc. A lot of large rolls are used for those equipments. At present cast iron, carbon steel, and alloy steel are used as roll materials in the coil painting and also continuous acid wash equipments, which induce wear on the roll surface in a short period than expected. Therefore, the production lines have to be stopped to exchange the rolls requiring a lot of time for maintenance. Then, the damage portions have to be repaired by using the flame spray coating⁽²⁾.

Figure 2 shows the structure of the rolls. In this study, we will focus on the roll structure where a sleeve and two short shafts are initially connected by shrink fitting at both ends, and shaft and spacer rings are finally connected by welding as shown in Fig. 5.2. The use of hard facing roll spraid by ceramics and cemented carbide is recently

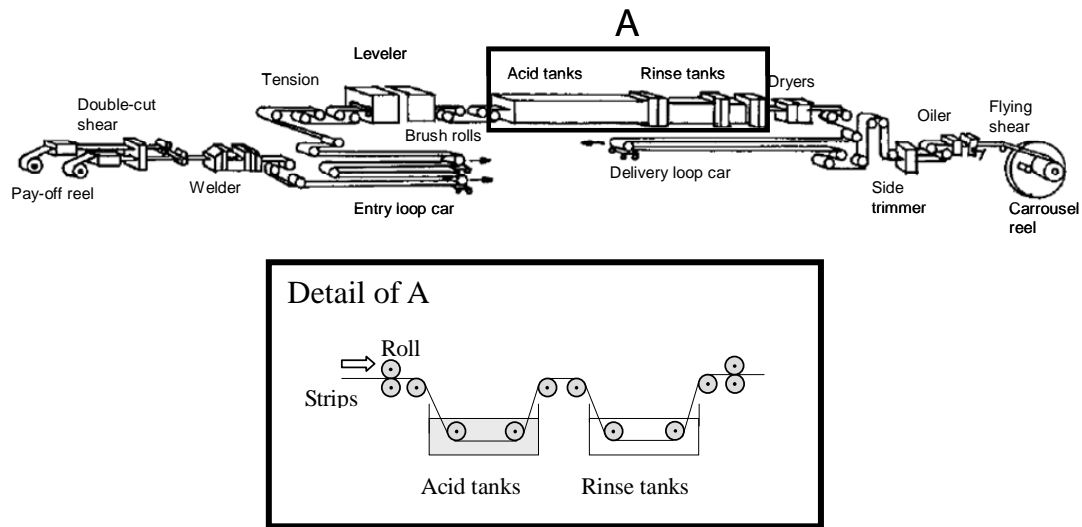


Fig. 5.1 Schematic diagram of new pickling line

promoted⁽³⁾ because they provide high temperature resistance, high abrasion resistance and anti-oxidation. Here, we consider ceramics sleeve and ceramics spacer rings connected by shrink fitting, which are suitable for reducing the cost for maintenance.

However, to design the hollow rolls as shown in Fig. 5.2, attention should be paid to the maximum tensile stresses and stress amplitude appearing at the edge of the sleeve. In particular, since fracture toughness is extremely smaller and fatigue strengths of ceramics are small, stress analysis for the roll becomes more and more important compared with the cases for steel rolls. Therefore, in this study FEM analysis will be applied to the structure as shown in Fig. 5.3, and suitable dimensions will be discussed.

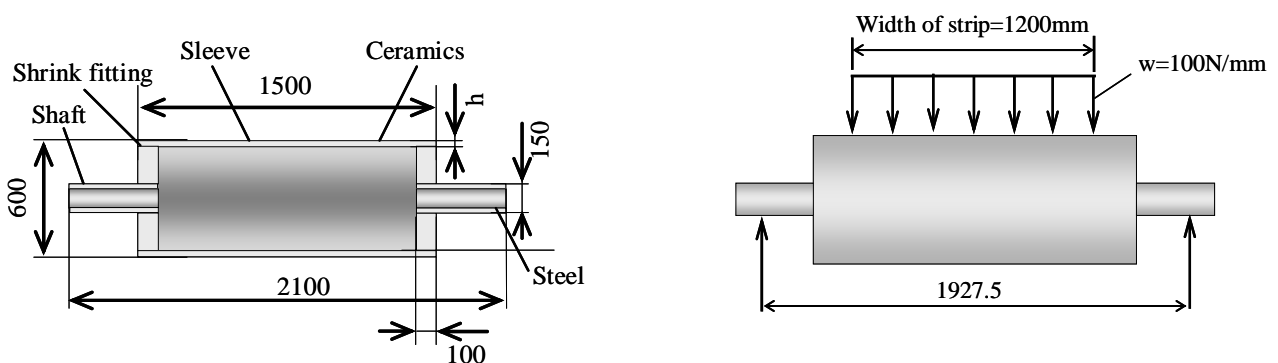


Fig. 5.2 New ceramics roll system (mm)

Table 5.1 Material Properties

	Young's modulus [GPa]	Poisson's ratio	Tensile strength [MPa]	Fracture toughness [$\text{MPa}\sqrt{\text{m}}$]	Fatigue strength [MPa]
Ceramics (Si_3N_4)	300	0.28	500	7	200
Steel (HV=220)	210	0.3	600	100	300
Cemented Carbide	500	0.24	1000	20	400

5.2. Analytical Conditions

Define the shrink fitting ratio as δ/d , where δ is the diameter difference with the diameter d . Assume that the roll is subjected to distributed load $w=100\text{N/mm}$ and simply supported at both ends (see Fig. 5.2). The friction coefficient between sleeve and shafts is assumed as 0.3.

Table 5.1 shows the material properties of ceramics, steel, and cemented carbide. Stainless steel is usually used for rolls but ceramics and cemented carbide rolls may provide a longer maintenance span due to their high corrosion resistance and high abrasion resistance.

Figure 5.3 shows the finite element mesh model of the rolls. The total number of elements is 37020 and the total number of nodes is 26751. The model of 1/4 of the roll

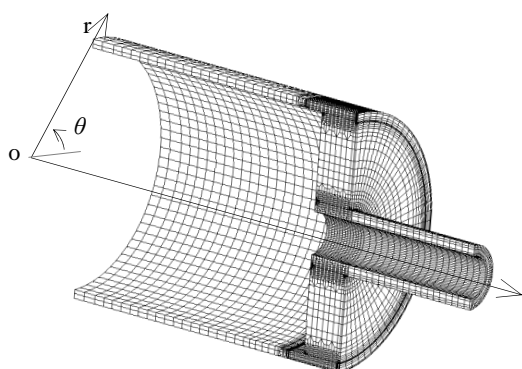


Fig. 5.3 FEM mesh

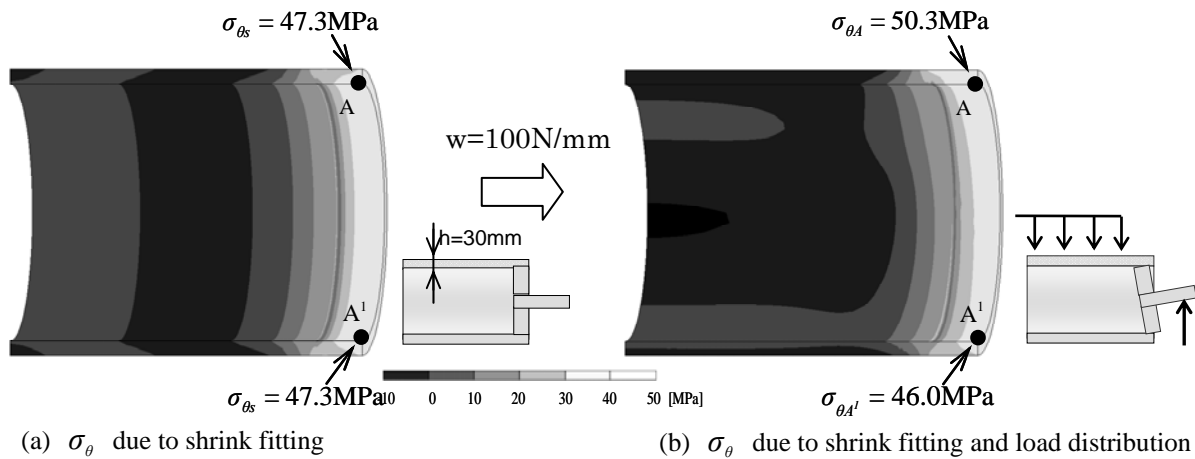


Fig. 5.4 Stress distribution σ_{θ} when $\delta/d = 1.5 \times 10^{-4}$

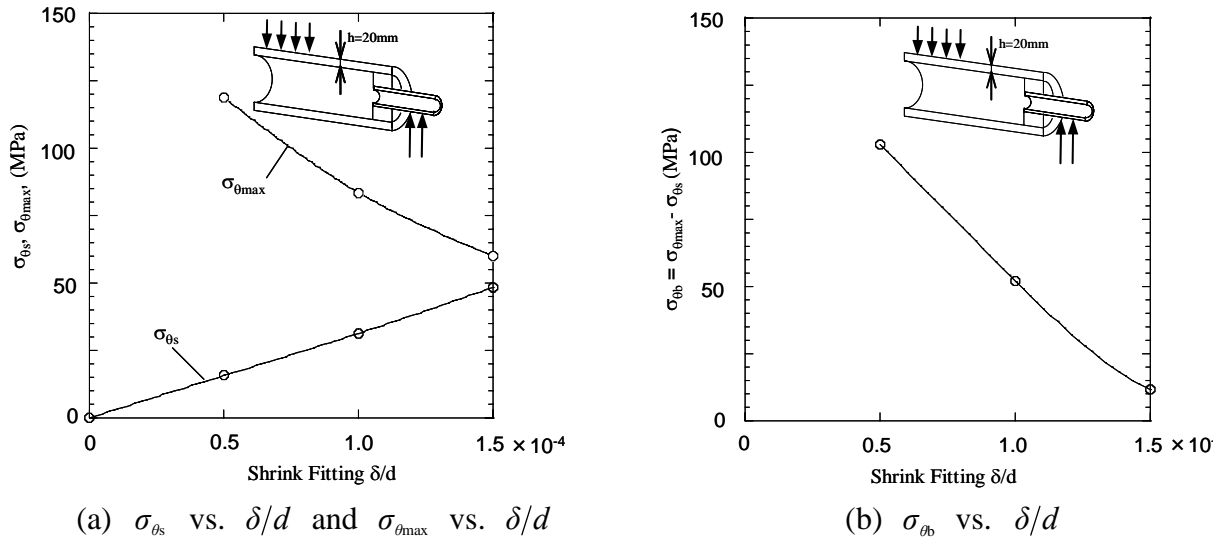
is considered due to symmetry.

5.3. Maximum Tensile Stress Analysis

5.3.1 Maximum Tensile Stress

We will consider the range $\delta/d \leq 1.5 \times 10^{-4}$ because large values δ/d are not suitable for ceramics. Figure 5.4 shows stress distribution σ_{θ} at the shrink fitting ratio $\delta/d = 1.5 \times 10^{-4}$ and the sleeve thickness $h = 30 \text{ mm}$. Figure 5.4 (a) shows the stress σ_{θ_s} due to shrink fitting and Fig. 5.4 (b) shows maximum stress distribution $\sigma_{\theta_{\max}} (= \sigma_{\theta_s} + \sigma_{\theta_b})$ due to load distribution $w = 100 \text{ N/mm}$ after shrink fitting. As shown in Fig. 5.4 (a), the maximum tensile stress at point A and A^1 are $\sigma_{\theta_s} = 47.3 \text{ MPa}$ while shrink fitting. It becomes $\sigma_{\theta_{\max}} = 50.3 \text{ MPa}$ by applying the distribution load after shrink fitting at point A and $\sigma_{\theta_{\max}} = 46.0 \text{ MPa}$ at point A^1 as shown in Fig. 5.4 (b). In other words, σ_{θ_b} increases by $\sigma_{\theta_b} = 2.9 \text{ MPa}$ at point A.

It is found that the maximum tensile stress appears at point A as σ_{θ} . In this chapter we will focus on reducing the maximum tensile stress σ_{θ} at A with varying geometrical conditions.

(a) σ_{θ_s} vs. δ/d and $\sigma_{\theta_{\max}}$ vs. δ/d (b) σ_{θ_b} vs. δ/d Fig. 5.5 σ_{θ} vs. δ/d when $h=20\text{mm}$

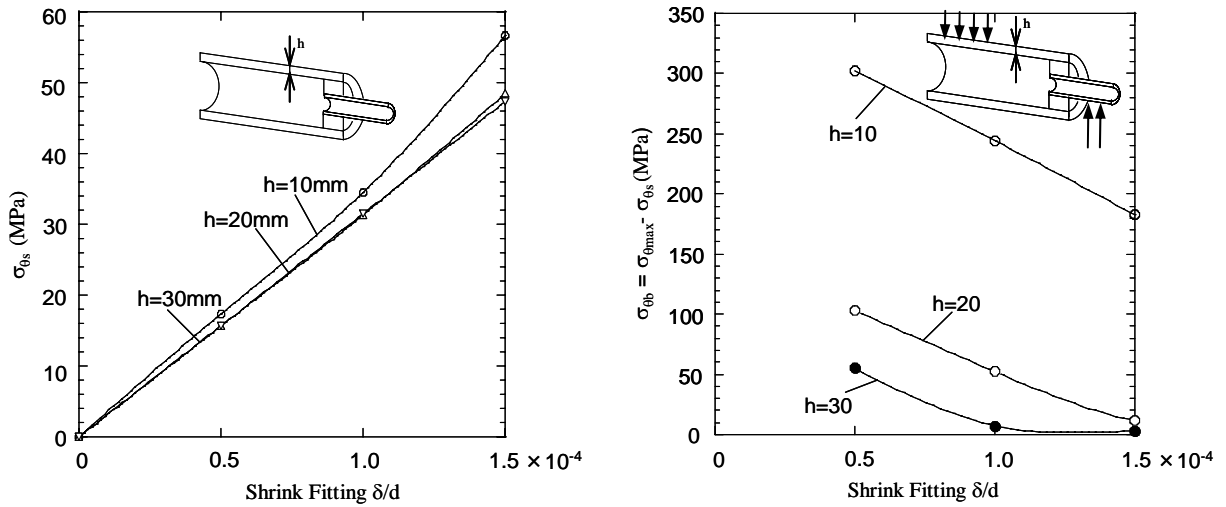
($\sigma_{\theta_{\max}} (= \sigma_{\theta_s} + \sigma_{\theta_b})$, σ_{θ_s} : Stress due to shrink fitting, σ_{θ_b} : Stress due to load distribution)

5.3.2 Effect of Shrink Fitting Ratio δ/d and Bending Moment upon the Maximum Tensile Stress $\sigma_{\theta_{\max}}$

Figure 5.5 illustrates effects of shrink fitting ratio δ/d upon the stresses σ_{θ_s} , $\sigma_{\theta_{\max}}$ and σ_{θ_b} . Figure 5.5 (a) shows the stress σ_{θ_s} vs. δ/d and $\sigma_{\theta_{\max}} (= \sigma_{\theta_s} + \sigma_{\theta_b})$ vs. δ/d relationships when the load distribution $w=100\text{N/mm}$ is applied after shrink fitting when $h=20\text{mm}$. From Fig. 5.5 (a), it is found that σ_{θ_s} increases with increasing δ/d and $\sigma_{\theta_{\max}}$ has a minimum value at $\delta/d=1.5 \times 10^{-4}$. On the other hand, σ_{θ_b} decreases with increasing δ/d as shown in Fig. 5.5 (b). From Fig. 5.5 (b), it is found that the large δ/d reduces the contact stress σ_{θ_b} by gripping the shaft tightly. It may be concluded that $\sigma_{\theta_{\max}} (= \sigma_{\theta_s} + \sigma_{\theta_b})$ may decrease with increasing δ/d .

5.3.3 The Effect of Thickness h on σ_{θ_s} and σ_{θ_b}

Figure 5.6 shows σ_{θ_s} vs. δ/d and $\sigma_{\theta_b} = \sigma_{\theta_{\max}} - \sigma_{\theta_s}$ vs. δ/d relations when the load distribution $w=100\text{N/mm}$ is applied after shrink fitting for different thickness h .

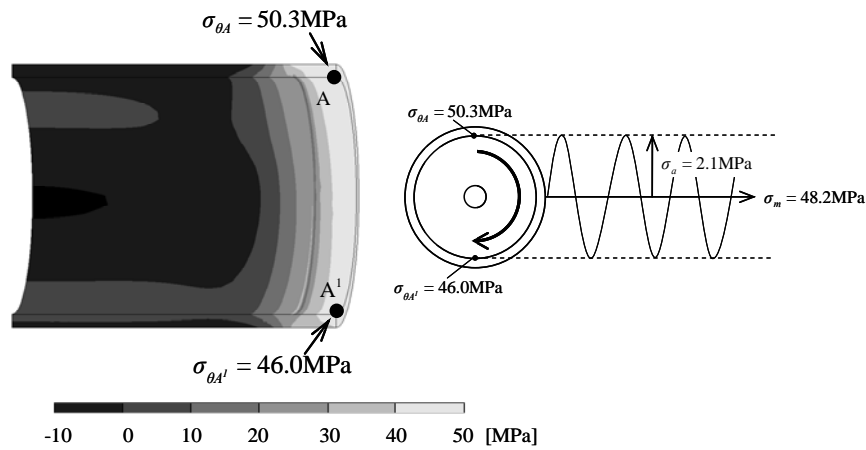
(a) σ_{θ_s} vs. δ/d (b) σ_{θ_s} vs. δ/d Fig. 5.6 σ_{θ} vs. δ/d when $h=10, 20,$ and 30mm

(σ_{θ_s} : Stress due to shrink fitting, σ_{θ_b} : Stress due to load distribution)

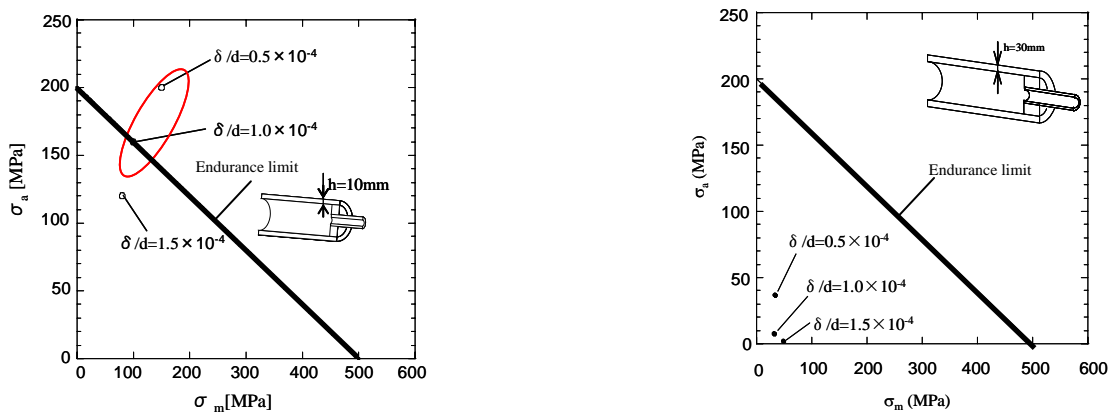
Here, we assume three different thicknesses, $h=10\text{mm}$, $h=20\text{mm}$, and $h=30\text{mm}$. From Fig. 5.6 (a), it is seen that σ_{θ_s} increases with increasing δ/d . It should be noted that σ_{θ_s} decreases with increasing the sleeve thickness h . Similarly, σ_{θ_b} decreases with increasing sleeve thickness h in Fig. 5.6 (b). When the δ/d is larger, the spacer rings and sleeve can be treated as a unit body bonded perfectly in sleeve thickness 30mm.

5.4. Fatigue Strengths Analysis of Ceramics Rolls

Maximum stresses are found to be lower than the tensile stress 500MPa as shown in the previous chapter. However, fatigue strengths should be also considered for ceramics. The values of fatigue limit such as $\sigma_a = 200\text{MPa}$ and $\sigma_m = 500\text{MPa}$ are obtained at room temperature as shown in Fig. 5.7 (b). However, the previous study show that the mechanical properties of ceramics are not changed up to 1000°C ⁽⁴⁾. Figure 5.7 (a) indicates the mean stress $\sigma_m = (\sigma_{\theta_{tA}} + \sigma_{\theta_{tA'}})/2$ and stress amplitude



(a) σ_{θ} due to shrink fitting and load distribution for ceramics roll $h=30\text{mm}$



(b) States of stress and endurance limit of ceramics rolls $h=10\text{mm}$ and 30mm

Fig. 5.7 Mean stress and stress amplitude for ceramics rolls

$\sigma_a = (\sigma_{\theta A} - \sigma_{\theta A'}) / 2$ at shrink fitting ratio $\delta/d = 1.5 \times 10^{-4}$ when thickness $h=30\text{mm}$. Due to the rotation of rolls, the largest value of σ_{θ} varies from 50.3MPa to 46.0MPa as shown in Fig. 5.7 (a). Then, the corresponding value of mean stress $\sigma_m = 48.2\text{MPa}$ with the value of stress amplitude $\sigma_a = 2.1\text{MPa}$. With increasing the shrink fitting ratio δ/d , the mean stress increases but the stress amplitude decreases in the case of $h=30\text{mm}$. As shown in Fig. 5.7 (b), it is found that the values of stress amplitude σ_a and mean stress σ_m are below the fatigue strengths of ceramics material. In the case of thickness $h=10\text{mm}$, the mean stress and stress amplitude increase when the shrink fitting ratio δ/d is less than 1.0×10^{-4} as shown in Fig. 5.7 (b). Under this condition, the values of fatigue exceed value the fatigue limit. This is not suitable for designing the rolls.

5.5. Conclusions

Cast iron and steel rolls used in the continuous pickling line must be changed frequently because the continuous acid wash equipment process induces wear on the roll surface in a short period. Therefore the production lines have to be stopped to exchange the rolls with requiring a lot of time for maintenance. To reduce maintenance cost for exchanging the rolls, in this study, a new structure was considered where a ceramics sleeve connected with ceramics spacer rings and steel shafts at both ends by shrink fitting. Strengths analysis was performed with the application of the finite element method with varying several geometrical conditions. The conclusions can be made in the following way.

1. The maximum tensile stress is appearing at the end of the sleeve as $\sigma_{\theta_{\max}}$. The stress $\sigma_{\theta_{\max}}$ may be expressed as $\sigma_{\theta_{\max}} (= \sigma_{\theta_s} + \sigma_{\theta_b})$ where σ_{θ_s} is a shrink fitting stress and σ_{θ_b} is a stress due to load distribution. For example, the maximum tensile stress at point A and A¹ are $\sigma_{\theta_s} = 47.3\text{MPa}$ while shrink fitting when the thickness $h=30\text{mm}$, shrink fitting ratio $\delta/d = 1.5 \times 10^{-4}$. It becomes $\sigma_{\theta_{\max}} = 50.3\text{MPa}$ by applying the distribution load after shrink fitting at point A and $\sigma_{\theta_{\max}} = 46.0\text{MPa}$ at point A¹. In other words, σ_{θ_b} increases by $\sigma_{\theta_b} = 2.9\text{MPa}$ at point A.
2. For small values of δ/d , the maximum stress $\sigma_{\theta_{\max}}$ becomes larger because large contact stresses may appear between the sleeve and shafts, especially for small thickness h . The maximum values of $\delta/d = 1.5 \times 10^{-4}$ may reduce $\sigma_{\theta_{\max}}$ effectively. In other words, $\sigma_{\theta_{\max}}$ takes a minimum value at $\delta/d = 1.5 \times 10^{-4}$.
3. The effect of thickness of the sleeve was considered. It is seen that σ_{θ_s} increases with increasing δ/d . It should be noted that σ_{θ_b} decreases with

increasing the sleeve thickness h . Similarly, σ_{θ} decreases with increasing sleeve thickness h in Fig. 5.6 (b).

4. Fatigue strength was also considered for ceramics rolls. When $\delta/d = 1.5 \times 10^{-4}$ with thickness $h=30\text{mm}$, it is found that the values of stress amplitude σ_a and mean stress σ_m are definitely below the fatigue strengths of ceramics material.

References

1. US Patent 5412966, *Push-pull pickle line*, Available from <www.freepatentsonline.com>
2. Miki, E., "High Corrosion Resistance and Cost Reduction by Spraying Methods", *Plant Engineer*, Vol. 21, No.1, pp.8-12, 1989 (in Japanese).
3. Iwata, T. and Mori, H., "Material Choice for Hot Run Table Roller", *Plant Engineer*, Vol.15, No.6, pp.55-59, 1983 (in Japanese).
4. Miyahara, N., Mutoh, Y., Oikawa, T., and Yabuta, K., Strength and Fracture Toughness of SiAlON at Elevated Temperatures, *Journal of Japan Society of Mechanical Engineering (Seri A)*, Vol. 59, No. 567, pp. 2546-2552, 1993.
5. Harada, S., Noda, N., Uehara, O. and Nagano, M., "Tensile Strength of Hot Isostatic Pressed Silicon Nitride and Effect of Specimen Dimension", *Transactions of the Japan Society of Mechanical Engineering*, Vol. 57, No. 539, pp.173-178, 1991.
6. Tsuyunaru, M., Noda, N. A., Hendra and Takase, Y., "Maximum Stress for Shrink Fitting System used for Ceramics Conveying Rollers", *Transactions of the Japan Society of Mechanical Engineering*, Vol.74, No.743, pp.919-925, 2008 (in Japanese).

Chapter 6

Summary

6.1 Conclusion of This study

Structural engineering ceramics are widely used in all kinds of engineering fields for their advantages of wear resistance, corrosion resistance, abrasion resistance and high heat resistance. The ceramics have been used for turbo-charger, gas turbine, auto heat engine, rolls, die cast sleeve, stalk and conveying roller. However, it is not easy to utilize large ceramics material in many kinds of engineering fields more efficiently because of their high cost of machining and low toughness compared with metallic material. In this study, the maximum tensile stresses and stress amplitude of ceramics structure will be mainly considered by the application of the finite element method. Then, how to reduce the maximum stress will be investigated with varying dipping speeds for ceramics tube, and with varying the dimensions of the structure for conveying rollers.

(1) In chapter 1, introduction about ceramics applications in this study was explained briefly. Ceramics are compound between metallic and nonmetallic elements. Oxides, nitrides, borides, carbides and silica at all metals and non metallic elemental solids are ceramics. Glasses, traditional ceramics, engineering ceramics, cements and concretes, rocks and minerals, ceramics composites and new engineering ceramics are types of ceramics. The characteristics of ceramics are high stiffness, high wear and heat resistances, good thermal and electric isolative characteristic, non-magnetic, chemically stable, refractory and brittle. Nowadays, ceramics engineering encompasses much more than silicates and divided into traditional and advanced ceramics. Five classes of

advanced ceramics for structure are alumina, zirconia, silicon nitride, sialon and silicon carbide. Advanced ceramics have found in electrical insulator, automotive engines, tribological components and cylinder head plates, pistons and turbocharger rotors, machine tools, cold rolling mill rolls and low pressure die casting machine. In this study, ceramics (silicon nitride and Sialon) are considered for material tube and rollers because it has high heat resistance, high corrosion resistance and high abrasion resistance. However, attention should be paid to the thermal stress when the ceramics tube is dipped into the molten metal. It is important to reduce the risk of fracture that may happen due to the thermal stresses. Also for conveying rollers, attention should be paid to the maximum tensile stresses (appearing at the edge of the sleeve) for brittle fracture and maximum repeated stress amplitude for fatigue fracture. In particular, because fracture toughness of ceramics is extremely smaller compared with the values of steel, more exact stress analysis for the roller becomes more and more important.

(2) In chapter 2, effect of heat transfer coefficient α on the thermal stress and thermal stress analysis for simple ceramics tube model vertical and horizontal dipping into molten metal have been conducted. In this analysis, finite volume method and finite element method are used for heat transfer coefficient and thermal stress calculated.

- 1) Since the value of heat transfer coefficient α is not well known in molten metal, we have confirmed the effect of α on the thermal stress of ceramics. Three values of α are assumed, first α_{Zu} by Zukauskas formula, second infinite large value of α_i and third α_{FVM} by applying finite volume method. The results show the maximum stress due to the infinite value of α_i is much larger than that due to Zukauskas formula and finite volume method. It is found that just assuming a very large α

does not provide correct thermal stresses. Maximum stress of α using Zukauskas formula and finite volume method is nearly the same but the time for reaching maximum stress is different. It may be concluded that the finite volume method is desirable for calculating thermal stress of ceramics correctly.

- 2) The heat transfer coefficient α calculated by finite volume method is therefore applied to finite element method to calculate the thermal stresses when the simple tube is dipped into the crucible by varying dipping speeds ($u = 2\text{mm/s}$ and $u = 25\text{mm/s}$), and directions (vertical and horizontal).
 - a) For vertical tube, the maximum value $\sigma_{\theta_{\max}} = 246\text{MPa}$ for dipping fast is larger than that of $\sigma_{z_{\max}} = 128\text{MPa}$ for dipping slowly as shown in Figs. 2. 10 and 2. 11. Therefore, dipping slowly may be suitable for reducing the thermal stresses. On that condition, dipping fast ($u = 25\text{mm/s}$) causes larger temperature difference in the thickness direction of tube.
 - b) On the other hand, for horizontal tube as shown in Figs. 2. 14 (a) and 2. 14 (b), the maximum value $\sigma_{\theta_{\max}} = 258\text{MPa}$ for dipping slowly is larger than that of $\sigma_{\theta_{\max}} = 196\text{MPa}$ for dipping fast. In conclusion dipping fast may be suitable for reducing the thermal stresses.
 - c) Those different conclusions may be explained in terms of deformations of the tube. For vertical tube, the deformation is always axi-symmetric. However, for horizontal tube, dipping slowly causes large asymmetric deformation, which results in the largest $\sigma_{\theta_{\max}}$ at the inner surface of the end of the tube. This is due to large temperature difference

appearing between the dipped and upper parts. On the other hand, for dipping fast of horizontal tube, the deformation is almost axi-symmetric.

(3) In chapter 3, heat transfer coefficient α and thermal stress for simple ceramics tube and the tube having protuberance dipping vertical into molten aluminum have been conducted. The finite volume method is applied to calculate surface heat transfer coefficient α .

- 1) The results show the values of α for inner of vertical tube with protuberance are much smaller than those of the simple tube. The molten metal cannot go into the tube with protuberance smoothly and most of the molten metal has to detour the tube. The results in the outer α of tube with protuberance are also lower than the outer α of the simple tube in the zone $x < 200\text{mm}$. And when $x > 230\text{mm}$, the outer α of ceramics tube with protuberance becomes coincides with the outer α of simple tube.
- 2) For thermal stress, maximum stress for vertical tube with protuberance is larger by 2.5 times, than the value of simple tube in the case of dipping slowly.
- 3) For dipping fast the maximum stress with protuberance is 1.5 times larger than the simple tube.
- 4) In each case with protuberance maximum stress at the corner of the protuberance but for simple tube, maximum stress appears at the inner surface and inside of thickness of tubes. It can be concluded that dipping slowly may reduce the thermal stresses because dipping fast causes larger

temperature difference in the thickness direction of the tube with or without protuberance.

(4) In chapter 4, maximum stress for shrink fitting system used for ceramics conveying rollers has been conducted. In this study, new roller structure is considered where a ceramics sleeve is connected with steel shaft at both ends by shrink fitting. Finite element method analysis is applied to the new structure, and the shrink fitting stress σ_{θ_s} , maximum tensile stress $\sigma_{\theta_{max}}$ and bending stress σ_{θ_b} have been investigated with varying the dimensions and material of the structure. The stress $\sigma_{\theta_{max}}$ may be expressed by $\sigma_{\theta_{max}} = \sigma_{\theta_s} + \sigma_{\theta_b}$ where σ_{θ_s} is a shrink fitting stress and σ_{θ_b} is a stress due to load distribution. The results show maximum tensile is appearing at the end of the sleeve as $\sigma_{\theta_{max}}$.

- 1) The maximum value $\sigma_{\theta_{max}} = 85.6\text{MPa}$ appears under the load $w = 100\text{N/mm}$ after shrink fitting. The stress $\sigma_{\theta_s} = 75.2\text{MPa}$ and $\sigma_{\theta_b} = \sigma_{\theta_{max}} - \sigma_{\theta_s} = 10.4\text{MPa}$ when the fitted length $L = 210\text{mm}$, shrink fitting ratio $\delta/d = 3.0 \times 10^{-4}$, radius curvature $\rho = 5\text{mm}$, and outer diameter $D = 270\text{mm}$.
- 2) For small value of shrink fitting ratio δ/d , the maximum stress $\sigma_{\theta_{max}}$ becomes larger. The stress σ_{θ_s} increases linearly with increasing δ/d . On the other hand, σ_{θ_b} decreases with increasing δ/d and becomes constant.
- 3) The stresses σ_{θ_s} and $\sigma_{\theta_{max}}$ increases with decreasing length fitted L and radius curvature ρ . The stress $\sigma_{\theta_{max}}$ has a minimum value at $\delta/d = 0.5 \times 10^{-4}$ for $L = 210\text{mm}$, $\delta/d = 1.2 \times 10^{-4}$ for $L = 150\text{mm}$ and $\delta/d = 1.8 \times 10^{-4}$ for $L = 100\text{mm}$. The stress σ_{θ_b} increases with decreasing

L and ρ , and becomes constant at larger δ/d . For larger length fitted L and radius curvature ρ of the sleeve may reduce $\sigma_{\theta_{\max}}$.

- 4) For different materials and diameter of sleeve, the stresses σ_{θ_s} and $\sigma_{\theta_{\max}}$ increases with increasing Young's modulus and diameter. The stress σ_{θ_b} decreases with increasing δ/d and becomes constant.

(5) In chapter 5, static and fatigue strengths for shrink fitting system used for ceramics rolls in the continuous pickling line has been conducted. In this chapter, new roller structure is discussed where a ceramics sleeve is connected with ceramics spacer rings and steel shaft at both ends by shrink fitting. Finite element method analysis is applied to the new structure, and the maximum tensile stress and stress amplitude have been investigated with varying the dimensions of the structure.

- 1) In this study, we considered the range of shrink fitting ratio $\delta/d \leq 1.5 \times 10^{-4}$. Here, we assume three different thicknesses of sleeve, $h=10\text{mm}$, $h=20\text{mm}$ and $h=30\text{mm}$. The results show the stress $\sigma_{\theta_s} = 47.3\text{MPa}$ while shrink fitting when the thickness $h=30\text{mm}$, shrink fitting ratio $\delta/d = 1.5 \times 10^{-4}$. It becomes $\sigma_{\theta_{\max}} = 50.3\text{MPa}$ by applying the distribution load after shrink fitting. In other words, σ_{θ_b} increases by $\sigma_{\theta_b} = 2.9\text{MPa}$. The stress σ_{θ_s} and $\sigma_{\theta_{\max}}$ increases with decreasing sleeve thickness h . The stress $\sigma_{\theta_{\max}}$ has a minimum value at $\delta/d = 1.5 \times 10^{-4}$.
- 2) When the δ/d is larger, the spacer rings and sleeve become as a unit body bonded perfectly. With increasing the shrink fitting ratio δ/d , the mean stress increases but the stress amplitude decreases.
- 3) The values of stress amplitude and mean stress are below the fatigue strength of ceramics material for thickness 20mm and 30mm under any

values shrink fitting ratio δ/d . However, under the condition when the thickness is smaller ($h=10\text{mm}$), δ/d is less than 1.0×10^{-4} the values of fatigue exceed value the fatigue limit. This is not suitable for designing of rolls.

6.2 Future Issue

There are some issues that should be investigated in future regarding the development of this study, which can be summarized as follows:

In order to grasp a comprehensive understanding of thermal stress and shrink fitting stress on a large ceramics structure, more numerical and experimental investigations are required.

It will be also necessary to do more study on the effect of heat transfer coefficient on the thermal stress for a large ceramics structure by using finite volume method.

Moreover, it is important to explore more on the actual production of new ceramics structure and compare the results of simulation (e.g., FEM) with actual operation.

Appendix A

Finite volume method

The finite volume method is a method for representing and evaluating partial differential equations in the form of algebraic equations [LeVeque, 2002; Toro, 1999], especially for those of the advection-diffusion-reaction type. Finite volume methods have been used in many cases such as pressure and enthalpy for the velocity component and staggered grid for radiation hydrodynamics. Finite volume methods has some advantages such as their numerical robustness through the obtention of maximum principle, their applicability on very general unstructured meshes and the intrinsic local conservation properties of the resulting discretized system.

Finite volume refers to the small volume surrounding each node point on a mesh. The method is used in many computational fluid dynamics (CFD) packages. CFD is the science of predicting fluid flow, heat transfer, mass transfer, chemical reactions, and related phenomena by solving the mathematical equations which govern these processes using a numerical process.

The strategy of CFD is to replace the continuous problem domain with a discrete domain using a grid. In the continuous domain, each flow variable is defined at

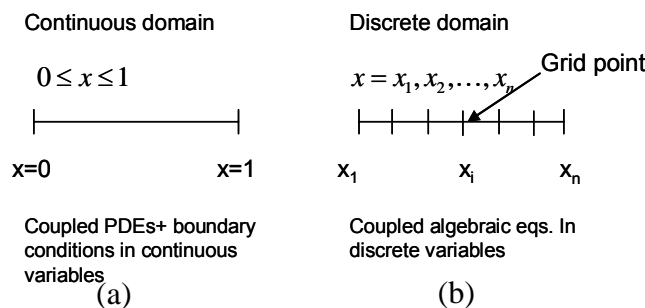


Fig. A. 1 Continuous domain and discrete

every point in the domain. For instance, the pressure p in the continuous

one-dimensional shown in Fig. A. 1 (a) would be given as

$$p = p(x), 0 < x < 1$$

In the discrete domain, each flow variable is defined only at the grid points. The pressure would be defined only at the N grid points as shown in Fig. A. 1 (b)

$$p_i = p(x_i), i = 1, 2, \dots, N$$

The governing partial differential equations and boundary conditions are defined in terms of the continuous variables p , \vec{V} etc. One can approximate these in the discrete domain in terms of the discrete variable p_i , \vec{V}_i . The discrete system is large set of coupled, algebraic equations in the discrete variables.

Applying the fundamental laws of mechanics to a fluid gives the governing equations for a fluid. The conservation mass equation is:

$$\frac{\partial \rho}{\partial t} + \nabla \cdot (\rho \vec{V}) = 0 \quad (1)$$

And the conservation of momentum equation is:

$$\frac{\partial \rho}{\partial t} + \rho (\vec{V} \cdot \nabla) \vec{V} = -\nabla p + \rho \vec{g} + \nabla \cdot \tau_{ij} \quad (2)$$

These equations along with the conservation of energy equation form a set of coupled, non linier partial differential equations.

In the finite volume method, such a quadrilateral is commonly referred to as a cell and a grid point as a node. In two-dimensional, one could also have triangular cells. In three-dimensional, cells are usually hexahedrals, tetrahedrals, or prisms. In the finite volume approach, the integral form of the conservation equations are applied to the control volume defined by a cell to get the discrete equation for the cell. The integral form of the continuity equation for steady, incompressible flow is:

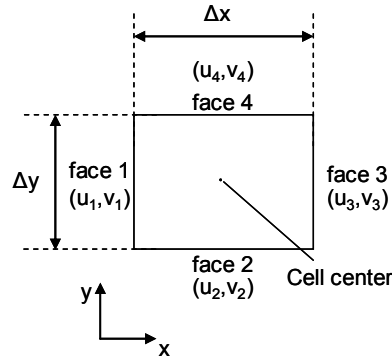


Fig. A. 2 Rectangular cell

$$\int_S \vec{V} \cdot \hat{n} ds = 0 \quad (3)$$

Where S is over the surface of the control volume.

n is the outward normal at the surface.

Physically, this equation means that the net volume flow into the control volume is zero.

Consider the rectangular cell as shown in Fig. A.2. The velocity at face 1 is taken to be $\vec{V}_i = u_i \hat{i} + v_i \hat{j}$. Applying the mass conservation equation (3) to control volume defined by the cell gives:

$$-u_1 \Delta y - v_2 \Delta x + u_3 \Delta y + v_4 \Delta x = 0 \quad (4)$$

This is the discrete form of the continuity equation for the cell. It is equivalent to summing up the net mass flow into the control volume and setting it to zero. The face value u_1, v_2 , etc. are obtained by suitably interpolating the cell centre values at adjacent cells.

Fluent, like other commercial CFD code, offers a variety of boundary condition options such as velocity inlet, pressure inlet, pressure outlet, etc. it is very important that to specify the boundary condition in order to have a well defined problem.

Reference

1. Eymard, R. Gallouët, T. R. Herbin, R.(2000) *The finite volume method* Handbook of Numerical Analysis, Vol. VII, 2000, p. 713-1020. Editors: P.G. Ciarlet and J.L. Lions.
2. LeVeque, Randall (2002), *Finite Volume Methods for Hyperbolic Problems*, Cambridge University Press.
3. Toro, E. F. (1999), *Riemann Solvers and Numerical Methods for Fluid Dynamics*, Springer-Verlag.
4. Bhaskaran, R., and Collins, L., Introduction to CFD Basics, Fluent 6.0.

Appendix B

The heat transfer coefficients of α

The heat transfer coefficient is the primary quantity characterizing the convection heat transfer process. In any given flow situation, it can vary with position on the surface and with time. It depends strongly on the velocity and thermal boundary conditions, as well as the geometry of the body.

Zukauskas⁽¹⁾ proposed a convenient formula to estimate heat transfer coefficient for 2D circle as shown in Fig. B. 1. The heat transfer coefficients depend on the velocity as shown in Eq. B.1. Zukauskas⁽¹⁾ proposed the following equation to estimate Nusselt number for a two-dimensional cylinder in the fluid with the velocity u .

$$Nu_m \equiv \frac{\alpha_m \cdot D}{\lambda} = C_1 \cdot Re^n \cdot Pr^{0.37} \cdot \left(\frac{Pr}{Pr_w} \right)^{0.25} \quad (\text{B. 1})$$

$$Re = \frac{u \cdot D}{\nu}, \quad Pr = \frac{C_p \cdot \eta}{\lambda} \quad (\text{B. 2})$$

where, α_m is the average surface heat transfer coefficient, λ is thermal conductivity, D is the diameter of the cylinder, C_1 and n are constants determined by Reynolds number Re . Also, Pr is Prandtl number, and subscript w denotes the property for temperature of cylinder wall. The velocity u can be calculated by the diameter of the tube divided by the time when the tube dips into the molten aluminum,

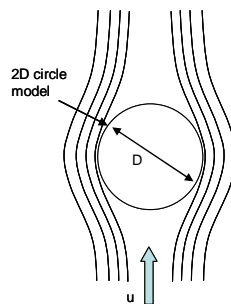


Fig. B. 1 Two-dimensional circle model

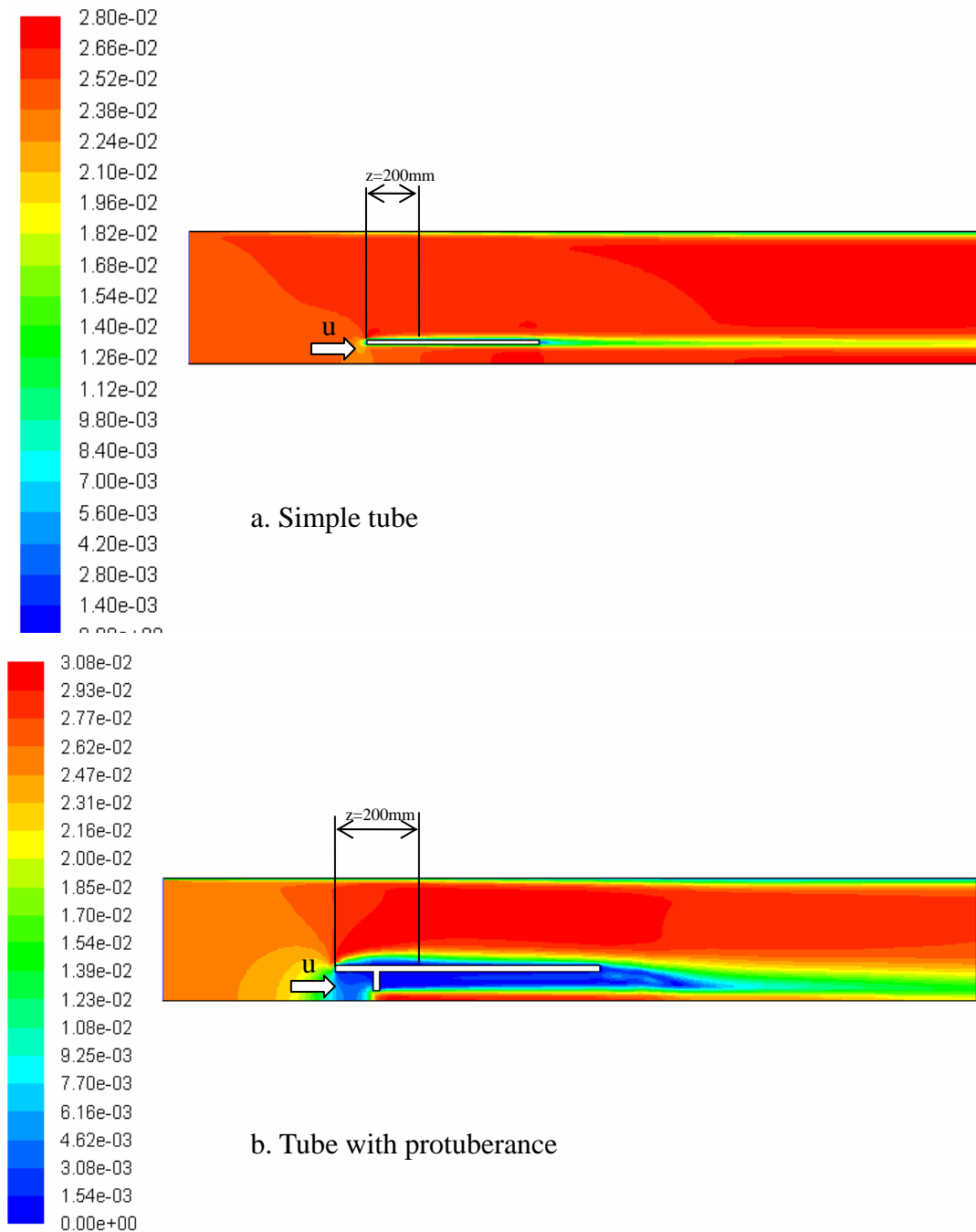


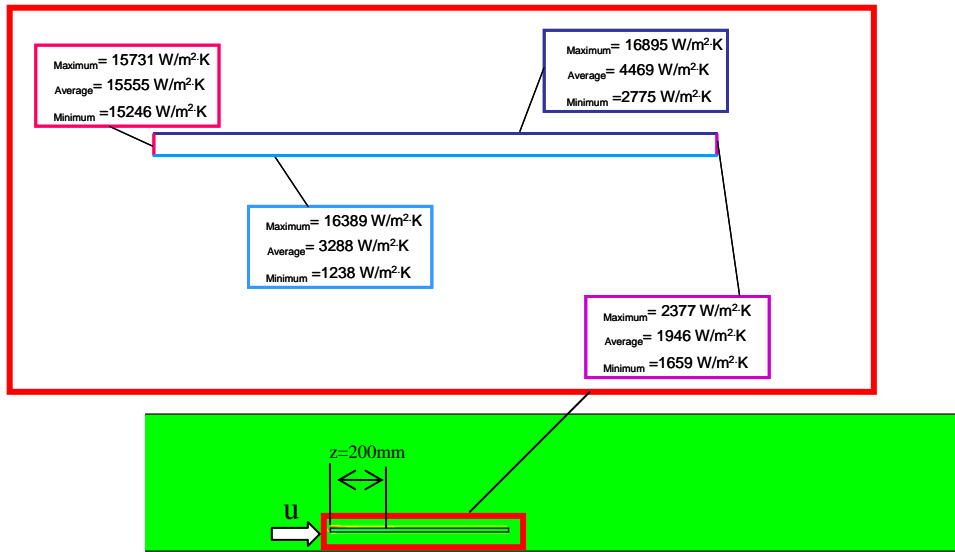
Fig. B.2 Comparison velocity simple tube and tube with protuberance

which is usually $u = 2 - 25\text{mm/s}$.

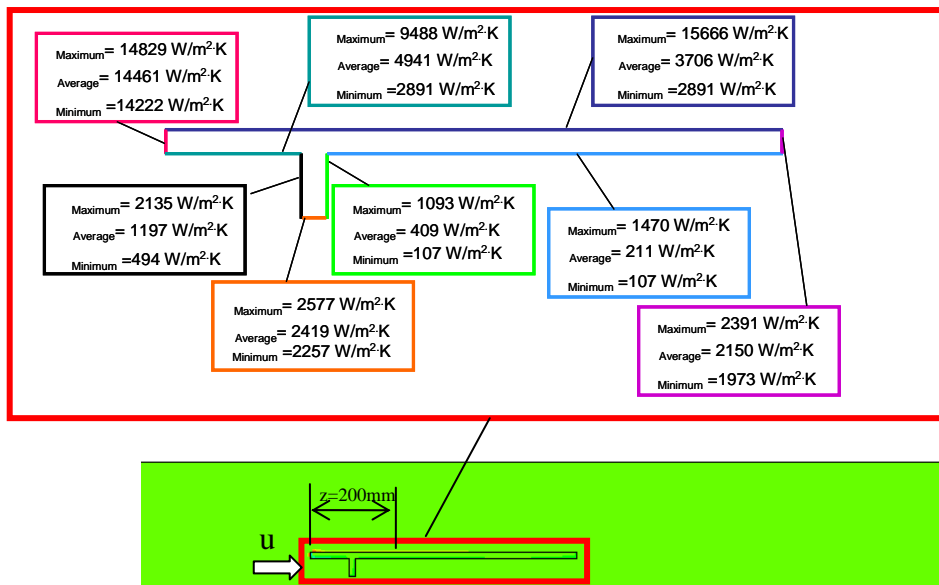
In the vertical tube, axi-symmetric models are analyzed by using the finite volume method to calculate α when the tube is dipped into the molten metal. For

Appendix B

axi-symmetry model, the values of the surface heat transfer coefficient α inner and outer of tube are different as shown in Fig. B. 3. Figure B. 3 shows comparison the surface heat transfer coefficient α of simple tube and tube with protuberance. As shown in Fig. B. 3 the values of α for inner of tube with protuberance are much smaller than those of the simple tube. The molten metal cannot go into the ceramics tube with protuberance smoothly and most of the molten metal has to detour the tube. Therefore, the outer α of ceramics tube with protuberance is also lower than the outer α of the simple tube when $z < 200\text{mm}$. And when $z > 230\text{mm}$, the outer α of ceramics tube with protuberance becomes coincides with the outer α of simple tube.



a. Simple tube



b. Tube with protuberance

Fig. B. 3 Comparison heat transfer coefficient of α distributions for simple tube and tube with protuberance

References

1. Zukauskas, A., Heat Transfer from Tubes in Cross Flow, In: Hartnett JP, Irvine Jr TF,

Appendix B

editors, *Advances in Heat Transfer*, Vol.8, New York: Academic Press, p. 131, 1972.

2. ME 320: Heat Transfer Laboratory, Lumped-Mass/Convection Heat Transfer Investigation, University of Illinois.
3. Bhaskaran, R., and Collins, L., *Introduction to CFD Basics*, Fluent 6.0.